DISSERTATION

Analysis of nephrotoxic changes induced by calcineurin inhibitors in a rat model

Analyse nephrotoxischer Nebenwirkungen von Calcineurininhibitoren im Rattenmodell

zur Erlangung des akademischen Grades
Doctor rerum medicinalium (Dr. rer. medic.)

vorgelegt der Medizinischen Fakultät

Charité – Universitätsmedizin Berlin

von

Hasan Demirci

aus Trabzon/Turkey

Erstbetreuung: Prof. Dr. Sebastian Bachmann

Datum der Promotion: 29 November 2024

Preface

Part of this study published at preprint server.

Demirci H., Popovic S., Dittmayer C., Yilmaz D. E., El-Shimy I. A., Mülleder, M., Hinze C. Persson B. P., Mutig K., Bachmann, S. (2023). Immunosuppression with Cyclosporine versus Tacrolimus shows distinctive nephrotoxicity profiles within renal compartments. bioRxiv, 2023-05. doi: https://doi.org/10.1101/2023.04.05.535688.

Table of Contents

List of tables

List of figures

List of abbreviations

3D-SIM	Three-dimensional structured illumination microscopy
6-MP	6-mercaptopurine
ACEI	Angiotensin converting enzyme inhibitor
ADMA	Asymmetric dimethylarginine
AKT	AKT Serine/Threonine kinase
AMPK	Adenosine-monophosphate activated protein kinase
ARB	Angiotensin receptor blocker
ATF6	Activating transcription factor 6
ATL	Ascending thin limb of Henle´s loop
AVR	Ascending vasa recta
BBM	Brush border membrane
BiP	Binding immunoglobulin protein
BUN	Blood urea nitrogen
Ca^{+2}	Calcium
CD144	VE-cadherin
CD2AP	CD2-associated protein
CD31	Platelet endothelial cell adhesion molecule 1
CHOP	CCAAT/enhancer-binding protein homologous protein
CKD	Chronic kidney disease
CN	Calcineurin
CnA	Calcinerin A, catalytic subunit
CnB	Calcinerin B, regulatory unit
CNI	Calcineurin inhibitor
CNT	Connecting tubule
CrCl	Creatinine clearance
CsA	Cyclosporine A
CTAL	Cortex thick ascending limb of Henle´s loop
DCT	Distal convoluted tubule
DDAH-2	Dimethylarginine dimethylaminohydrolases-2
DEG	Differentially expressed gene

DEP	Differentially expressed protein
DEPP	Differentially expressed phosphoprotein
DLT	Descending thin limb of Henle´s loop
DVR	Descending vasa recta
ECM	Extracellular matrix
EGM	Extraglomerular mesangium
eIF2α	Eukaryotic translation initiation factor 2
eNOS	Endothelial nitric oxide synthase
ER	Endoplasmic reticulum
ERAD	ER-associated protein degradation
ESRD	End-stage renal disease
ET-1	Endothelin-1
FAT-1	FAT atypical cadherin 1
FDR	False discovery rate
FeNa	Fractional excretion of sodium
FKBP12	FK-binding protein 12
FLT-1	Vascular endothelial growth factor receptor 1
FOXO	Forkhead transcription factors
FSD	Filtration slit density
GAG	Glycosaminoglycan
GBM	Glomerular basement membrane
GFB	Glomerular filtration barrier
GFR	Glomerular filtration rate
GO	Gene ontology
H_2O_2	Hydrogen peroxide
HPLC	High-performance liquid chromatography
IC	Intercalated cells
ICAM2	Intercellular adhesion molecule 2
IHC	Immunohistochemistry
IF/TA	Tubulo-interstitial fibrosis, tubular atrophy
IL2	Interleukin-2
IMCD	Inner medullary collecting duct
IRE1α	Inositol-requiring enzyme 1 α
JUNK	JUN N-terminal kinase

KEGG	Kyoto encyclopedia of genes and genomes
KIM1	Kidney injury molecule 1
LAMP1	Lysosomal-associated membrane protein 1
LM	Light microscopy
MCOLN1	Mucolipin 1
MD	Macula densa
MEF2	Myocyte-specific enhancer factor 2
mRNA	Messenger ribonucleic acid
MS	Mass spectrometry
mTAL	Medullary thick ascending limb of Henle´s loop
mTORC1	Mammalian target of rapamycin complex 1
Na^+	Soduim
NFAT	Nuclear factor of activated T cells
NKCC2	Na-K-2Cl cotransporter
NO	Nitrit oxide
PC	Principal cells
PCT	Proximal convoluted tubule
PECs	Parietal epithelial cells
PEMP	Podocyte exact morphology measurement procedure
PERK	Protein kinase RNA-like ER kinase
PGF	Placental growth factor
PODO	Podocyte
PST	Proximal straight tubule
PT	Proximal tubule
RAAS	Renin angiotensin aldesterone system
RIDD	RE1-dependent decay
RNA-seq	RNA sequencing
ROS	Reactive oxygen species
SDF-1	Stromal cell–derived factor 1
SEM	Scanning electron microscopy
SER	Serine
Tac	Tacrolimus
TAL	Thick ascending limb of Henle´s loop
TEM	Transmission electron microscopy

TFE3	Transcription factor binding to IGHM enhancer 3
TFEB	Transcription factor EB
TGF-β	Transforming growth factor beta
TMA	Thrombotic microangiopathy
TMT	Tandem mass tag
TRAF	TNF receptor-associated factor
TUNEL	Terminal deoxynucleotidyl transferase dUTP nick end labeling
ULK1	Atg1/unc-51 like autophagy activating kinase 1
UPR	Unfolded protein response
VEGF	Vascular endothelial growth factor
VEGFR2	Vascular endothelial growth factor receptor 2
WT1	Wilm´s tumor protein 1
XBP1	X-box binding protein 1

Abstract

Background: Calcineurin inhibitors (CNI) such as cyclosporine A (CsA) and tacrolimus (Tac, FK506) are commonly used as immunosuppressive drugs in patients with solid organ transplantation or autoimmune affections. With merits undisputed at short-term, their chronic use leads to nephrotoxicity in a significant proportion of renal or non-renal transplant recipients, resulting in compromised kidney function. Although attempts have been made to substitute CNIs with other immunosuppressants, the alternatives to CNIs are generally considered less effective. CsA has been considered more toxic than Tac, but the current preference for Tac over CsA needs further validation. Understanding the cellular mechanisms of their particular nephrotoxicity profiles should enable more personalized treatment protocols to minimize adverse effects. We therefore aimed to investigate whether CsA and Tac exhibit distinct renal damage patterns. Systemic and kidney parameters were studied in rats exposed to chronic CNI delivery.

Methods: Wild-type male Wistar rats (group size n=6 to 12) were treated with vehicle, CsA (30 mg/kg/day) or Tac (2 mg/kg/day) via subcutaneously implanted osmotic minipumps for 28 days. Histopathology and advanced microscopy techniques such as large-scale electron microscopy and 3D-structured illumination microscopy were used tissue analyses. Standard biochemistry, RNA sequencing as well as proteomic and phosphoproteomic analyses were conducted to identify molecular changes.

Results: Distinct damage patterns were observed in the CNI treatment groups compared to vehicle. Alterations were located in vasculature and nephron. Cells of the glomerular filtration barrier revealed displayed more damage by Tac than by CsA, with changes located in pore endothelium and podocytes. The VEGF/VEGFR2 pathways

as well as podocyte-specific gene expression were substantially and differentially altered. Contrastingly, the renal tubule was more severely affected by CsA than by Tac with prominent lysosomal dysfunction, impaired proteostasis, oxidative stress and enhanced apoptosis chiefly observed in the early proximal nephron.

Conclusion: We found that pathological changes in renal microenvironments were specific to each treatment. If our findings can be translated to the clinical context, the choice of CNI should consider individual risk factors related to renal vasculature and tubular epithelia. As a step in this direction, we present identified products and pathways from multiomics analyses with potential pathognomonic relevance.

Zusammenfassung

Hintergrund: Calcineurin-Inhibitoren (CNI) wie Cyclosporin A (CsA) und Tacrolimus (Tac, FK506) werden häufig als Immunsuppressiva bei Patienten mit Organtransplantation oder Autoimmunerkrankungen eingesetzt. Obwohl ihre Vorzüge kurzfristig unbestritten sind, führt ihre chronische Anwendung bei einem erheblichen Teil der Empfänger von Nieren- oder Nicht-Nierentransplantaten zu Nephrotoxizität, die zu signifikanter Beeinträchtigung der Nierenfunktion führen kann. Obwohl Versuche unternommen werden, CNI durch andere Immunsuppressiva zu ersetzen, gelten die Alternativen zu CNI im Allgemeinen als weniger wirksam. CsA gilt als toxischer als Tac, die derzeitige Bevorzugung von Tac gegenüber CsA bedarf jedoch weiterer Bestätigung. Das Verständnis der zellulären Mechanismen ihrer jeweiligen Nephrotoxizitätsprofile sollte personalisierte Behandlungsprotokolle fördern, um Nebenwirkungen zu minimieren. Unser Ziel war es daher zu untersuchen, ob CsA und Tac unterschiedliche Nierenschädigungsmuster aufweisen. Systemische und Nierenparameter wurden bei Ratten untersucht, die einer chronischen CNI-Verabreichung ausgesetzt waren.

Methoden: Männliche Wildtyp-Wistaratten (Gruppengröße n=6 bis 12) wurden über subkutan implantierte osmotische Minipumpen 28 Tage lang mit Vehikel, CsA (30 mg/kg/Tag) oder Tac (2 mg/kg/Tag) behandelt. Für Gewebeanalysen wurden Histopathologie und moderne Mikroskopietechniken wie *Large scale* Elektronenmikroskopie und *3D-structured illumination* Mikroskopie verwendet. Zur Identifizierung molekularer Veränderungen wurden grundlegende Biochemie, RNA-Sequenzierung sowie proteomische und phosphoproteomische Analysen durchgeführt.

Ergebnisse: In den CNI-Behandlungsgruppen wurden im Vergleich zur Vehikelgabe deutliche Schadensmuster beobachtet. Beide Medikamente verursachten erhebliche, aber unterschiedliche Schäden im Gefäßsystem und im Nephron. Komponenten der glomerulären Filtrationsbarriere wurden durch Tac stärker beeinträchtigt als durch CsA, was zu erheblichen Beeinträchtigungen des Porenendothels und der Podozyten, vereint mit geschwächter VEGF/VEGFR2-Signalübertragung und verminderter podozytenspezifischen Genexpression, führte. Im Gegensatz dazu wurde der Nierentubulus durch CsA stärker beeinträchtigt als durch Tac, wobei ausgeprägte lysosomale Dysfunktion, beeinträchtigte Proteostase, oxidativer Stress und verstärkte Apoptose hauptsächlich im frühen proximalen Nephron beobachtet wurden.

Schlussfolgerung: Wir fanden heraus, dass pathologische Veränderungen im Nierenparenchym für jede Behandlung spezifisch waren. Mit Bezug auf den klinischen Kontext sollten unsere Ergebnisse dazu verhelfen, bei der Wahl geeigneter Immunsuppressiva individuelle Risikofaktoren im Zusammenhang mit Nierengefäßen und tubulären Epithelien zu berücksichtigen. Als Schritt in diese Richtung stellen wir identifizierte Produkte und Signalwege aus den Multiomics-Analysen mit potenzieller pathognomonischer Relevanz vor.

1. Introduction

1.1 Kidney anatomy

The kidney is a bean-shaped organ located behind the abdominal cavity in the retroperitoneal space. It is surrounded by a fibrous capsule. The renal parenchyma is divided into the cortex and the medulla. Blood supply to the kidney comes from the renal artery and vein via the hilus. Arteries branch into interlobar, arcuate and interlobular arteries which give rise to afferent arterioles supplying individual glomeruli in superficial, midcortical and juxtamedullary position. Their efferent arterioles provide the supply for the peritubular interstitium via the glomerular efferent arterioles. Juxtamedullary efferent arterioles form the vasa recta constituting blood supply to the renal medulla (Treuting et al. 2018).
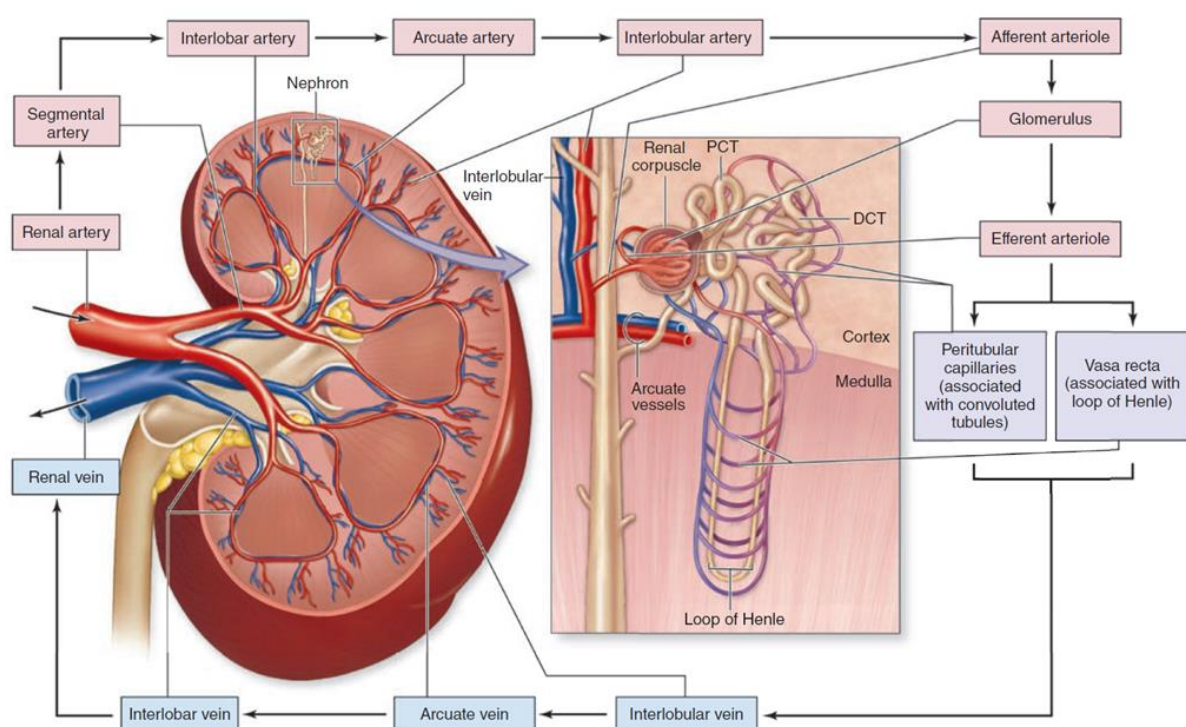
Figure 1. Gross anatomy of kidney and the structure of the nephron. On the left, a coronal view of the kidney displays the primary blood vessels, each labeled with its respective name. On the right, an enlarged diagram provides a detailed representation of the renal tubules and microvascular elements, extending from the interlobular vessels into both the cortex and

medulla. DCT, distal convoluted tubule; PCT, proximal convoluted tubule. Adopted from (Mescher 2021).

In the human kidney, approximately one million glomeruli per kidney are developed as the initial parts of the nephron (Eckardt et al. 2013). These are connected with the distinct tubular segments. During development capillaries sprout into an epithelial vesicle from the nephrogenic mesenchyme to form an S-shaped body (Patel and Dressler 2013). Capillaries then differentiate to the glomerular capillary tuft which is covered by the visceral epithelium and supplied by the afferent arteriole. At the vascular pole of the glomerulus, the visceral epithelim continues into the parietal epithelium of Bowman's capsule to create a capsular space (Quaggin and Kreidberg 2008). This space opens into the developing proximal tubule at the urinary pole. The terminally differentiated nephron comprises the proximal convoluted tubule (PCT), the proximal straight tubule (PST), the descending thin limb, the distal straight tubule (thick ascending limb, TAL), the macula densa, the distal convoluted tubule (DCT), and the connecting tubule which continues into the collecting duct system. Depending on the position of the glomerulus in the cortical parenchyma, an ascending thin limb may be formed. PST, thin limbs, and distal straight tubules form the loop of Henle (Marieb et al. 2020). The collecting duct system forms the papillary collecting ducts which open into the renal pelvis. The renal interstitium is the narrow space between the renal tubules and the peritubular capillaries. In the healthy organism it contains little connective tissue with few fibroblasts and immune cells. The position of the glomeruli and segmentation of the renal tubule along with their vascular supply results in the formation of the renal parenchymal zones, i.e., cortex, outer stripe and inner stripe of outer medulla, and inner medulla with innermost renal papilla (Figure 1) (Skorecki et al. 2016).

1.1.1 Renal vasculature

The kidney receives intensive blood supply reaching 20% of the cardiac output (Tamayo-Gutierrez and Ibrahim 2022). Blood comes from the renal artery which branches into segmental, interlobar, and arcuate arteries. The arcuate arteries take their course at the cortico-medullary border and give rise to the interlobular arteries of the cortex. From these, the afferent arterioles, which may be branched, supply the glomeruli. Before entering the glomerular tuft, their terminal media portion contains the enzyme renin, whose release is controlled by sympathetic nerve fibres (Mohamed and Sequeira-Lopez 2019). From there, the arteriole branches into the glomerular capillaries which are covered by the glomerular basement membrane and the podocyte epithelium. Capillaries are lined by the pore endothelium. The glomerular tuft then gives rise to the efferent arteriole which supplies the cortical peritubular interstitium with a second capillary bed lined by fenestrated endothelium. Cortical interlobular veins then collect the blood and drain into arcuate veins. Lymphatic vessels accompany cortical arteries and arterioles. While cortical arteries reveal regular wall structure, veins have capillary walls lacking a tunica media and are lined by fenestrated endothelium. Medullary blood supply comes from efferent arterioles of the juxtamedullary nephrons which may extend as far to the tip of the medulla as descending vasa recta. These vessels maintain their arteriolar structure until branching to the fenestrated endothelia of medullary interstitial capillaries which drain into the ascending vasa recta (Figure 2). In the inner stripe of the outer medulla, descending and ascending vasa recta are organized as the vascular bundles which exchange solutes and water with the medullary tubules (Pallone et al. 2012).
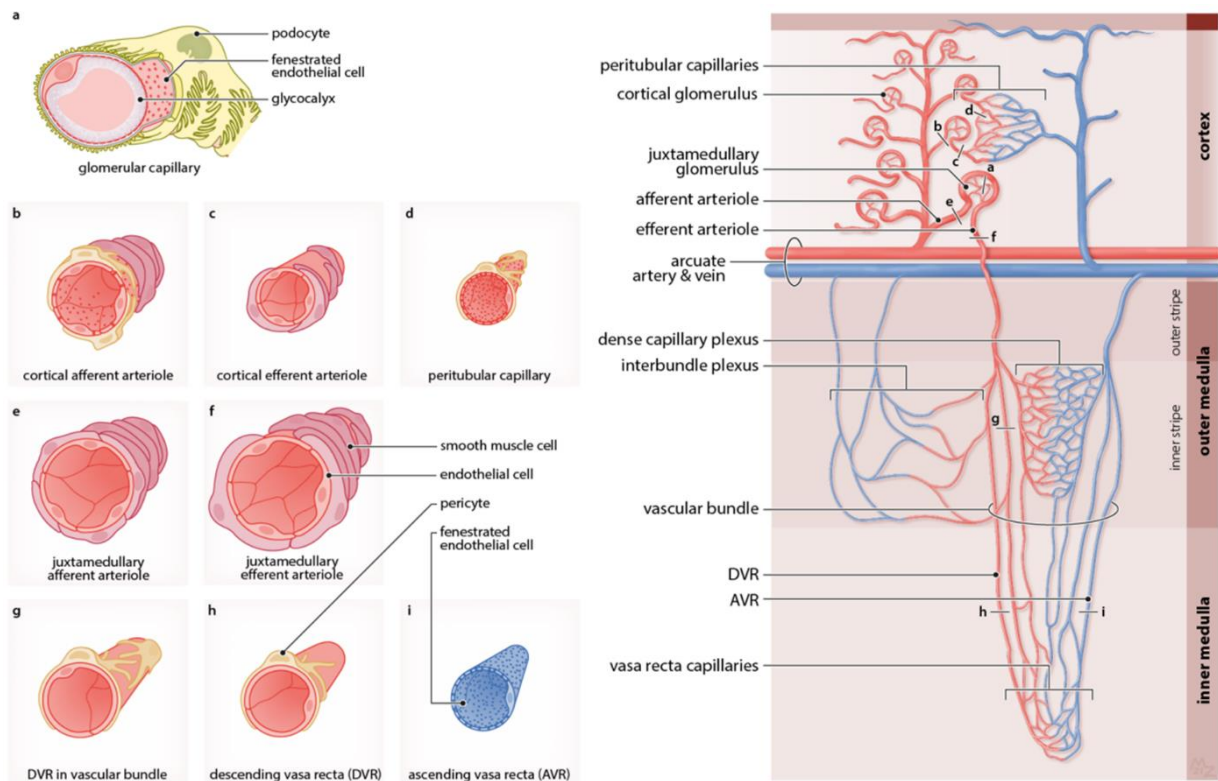
Figure 2. Renal microvascular network. (A) The glomerular capillaries have a fenestrated endothelium and are surrounded by podocytes. (B) The highly muscularized cortical afferent arteriole is surrounded by pericytes. (C) Cortical efferent arteriole is less muscularized. (D) Pericyte-surrounded peritubular capillaries. (E) Juxtamedullary afferent arterioles. (F) Juxtamedullary efferent arterioles. (G) Descending vasa rectum (DVR) in vascular bundle is surrounded by pericyte. (H) Descending vasa recta of inner zone. (I) Fenestrated ascending vasa recta (AVR). Adopted from (Apelt et al. 2021).

1.1.2 Glomerulus

The glomerulus (renal corpuscle) enables the formation of the primary urine as an ultrafiltrate of the blood. Blood is supplied by the afferent arteriole, whose muscle cell layer continues into the glomerular tuft as the mesangial cells which provide suspension to the capillary loops. These are lined by a unique pore endothelium which reveal fenestrae with diaphragms likely serving high throughput volume transfer. The glomerular basement membrane (GBM) ensheathes all capillaries incompletely, that is, on a given capillary the GBM continues towards the neighboring capillary at the level of the respective mesangial stalk (Scott and Quaggin 2015). At the vascular pole, the GBM leaves the capillaries to continue into Bowman's capsule, where it underlies the parietal epithelium as the capsular membrane. Within the glomerular tuft, the GBM

4

is covered by the layer of the visceral epithelium consisting of the podocytes. The podocytes give rise to the foot processes which are connected by the slit diaphragm in immediate vicinity to the GBM (Pavenstädt et al. 2003; Cortinovis et al. 2022). Pore endothelium, GBM and slit diaphragm of the podocytes constitute the glomerular filtration barrier (GFB) which controls the passage of ions and small molecules but helps to retain larger plasma proteins in the blood stream (Figure 3) (Fridén et al. 2011; Schlöndorff et al. 2017).

The glomerular endothelial cells of the capillary tuft are fenestrated but lack of diaphragms ("pore endothelium") to allow for high-volume of fluid filtration (Dumas et al. 2021). Fenestrae span roughly 20% of the cell surface area to enable the movement of the primary filtrate across the GFB (Satchell et al. 2006a). The glomerular endothelial cells also produce polyanionic glycosaminoglycans, glycoproteins, proteoglycans, and glycolipids which is called a glycocalyx or endothelial surface layer that covers the cell surfaces and imparts a negative charge (Jeansson and Haraldsson 2006). The glycocalyx has a role in the regulation of immune cell transit, shear stress reactivity, permeability, coagulation, and signaling in endothelial cells (Salmon and Satchell 2012). The glomerular endothelial cells express their distinctive markers, including von Willebrand factor (vWF), intercellular adhesion molecule 2 (ICAM2), platelet endothelial cell adhesion molecule 1 (PECAM1, CD31), vascular endothelial growth factor receptor 2 (VEGFR2), and VE-cadherin (Satchell et al. 2006b).
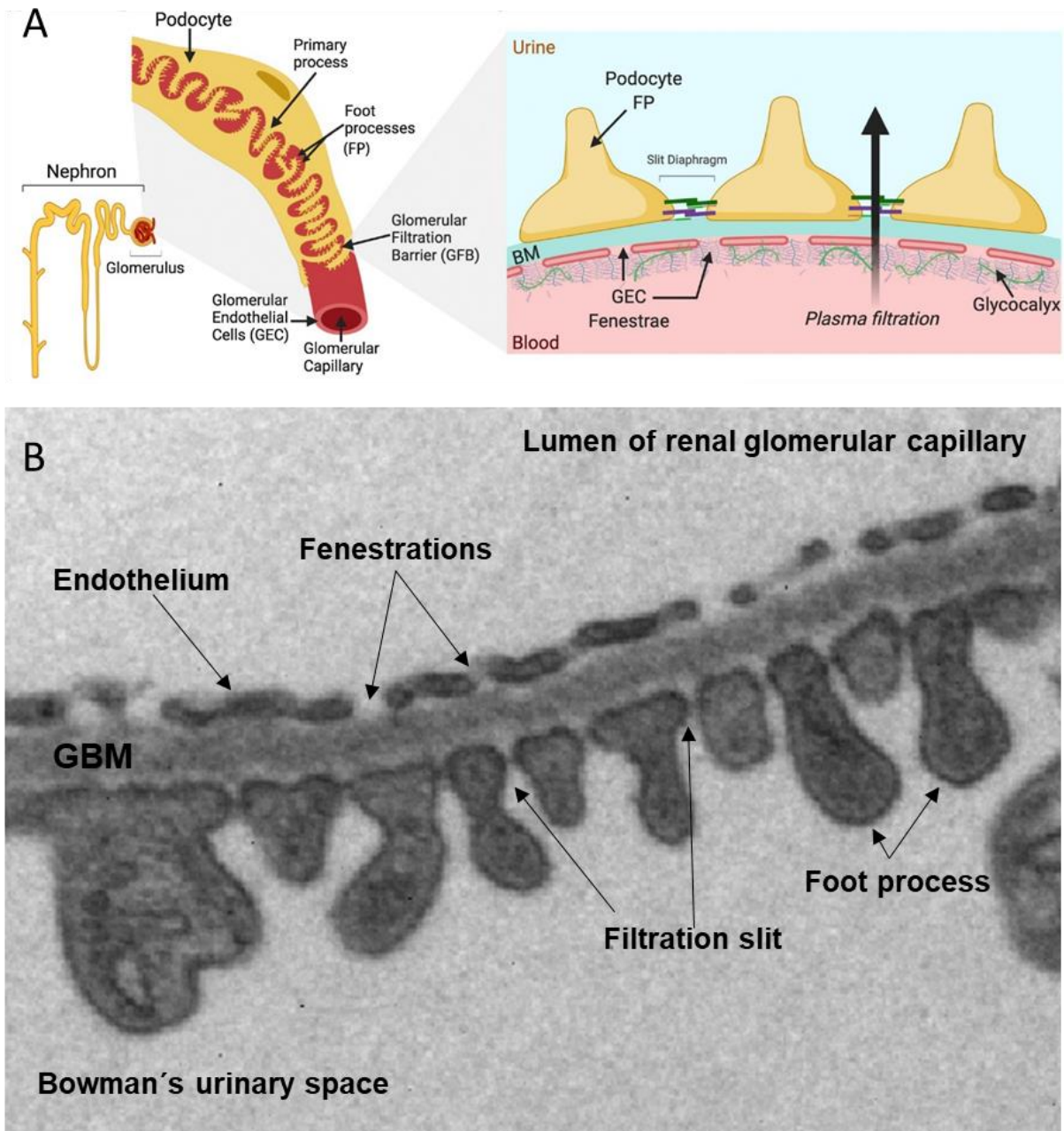
Figure 3. Podocyte and glomerular filtration barrier structure. (A) Schematic drawing of a single glomerulus and nephron, a glomerular capillary vessel, and the glomerular filtration barrier (GFB). (B) Electron micrograph shows glomerular basement membrane (GBM) lined by fenestrated glomerular endothelium; filtration slit and foot process belong to the podocytes. Adapted from (Ebefors et al. 2021).

1.1.2.1 Podocytes (Visceral epithelial cells)

The podocytes attach to the GBM via laminin and type IV collagen of the foot processes

(Garg 2018). The slit diaphragm is composed of an extracellular protein complex.

Proteins such as ZO-1, nephrin, NEPH1, podocin, CD2AP, FAT1, and P-cadherin form

this modified cell junction (Figure 4) (Huber et al. 2001; Ichimura et al. 2003; Benzing 2004).
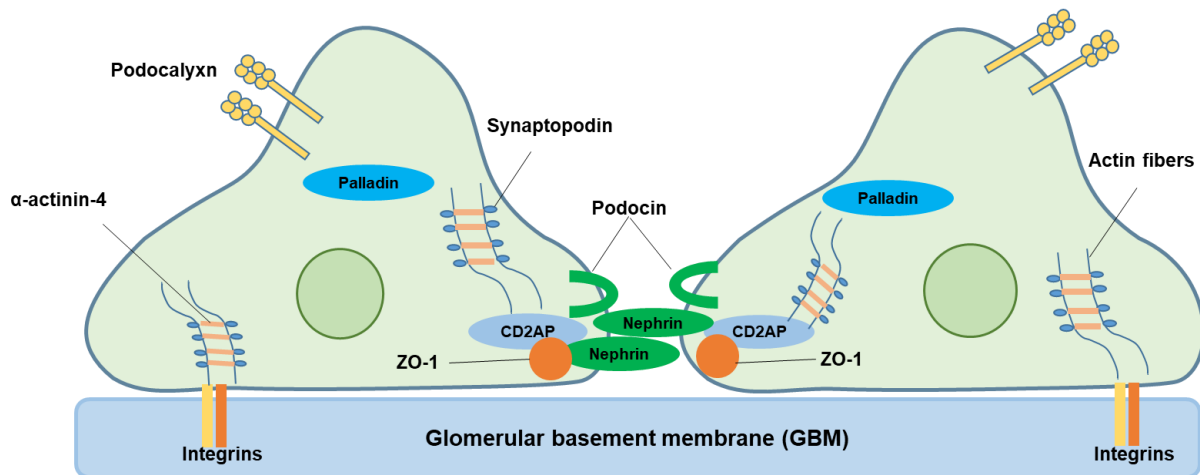
Figure 4. Overview and localization of important slit diaphragm proteins (Own design).

Podocytes supply structural support to the glomerular capillaries by adapting the foot process actin cytoskeleton in order to counteract the hydrodynamic pressures that are caused by vascular flow. In addition, podocytes need to acquire an elasticity that enables the capillary to expand and contract with each beat of the heart (Suleiman et al. 2017; Blaine and Dylewski 2020). These distinctive features are most likely mediated by its cytoskeletal structure. While the cell body and the major processes contain a significant amount of microtubules and intermediate filaments, foot processes are thought to develop this important actin network (Drenckhahn and Franke 1988). Mutations in proteins involved in the maintenance of the podocyte actin cytoskeleton are a common cause for genetic forms of glomerular disease (Lim et al. 2016). Podocyte damage may result in a change of podocyte architecture in which foot processes are diminished in number or are no longer distinguishable; this is known as foot process effacement which depends on the rearrangement of the podocyte cytoskeleton. There are two stages to the foot process effacement process. First, the foot processes retract, leaving behind short, amorphous cell protrusions lacking slit

diaphragms. Second, the GBM is no longer covered by the regular foot processes, as the podocytes overall structure transforms into a disc-like cell (Kriz et al. 2013). The number of podocytes continuously diminishes if the podocyte monolayer is damaged by disease (Vallon and Komers 2011). Podocyte loss is the primary driver of chronic kidney disease (CKD). The main cause of podocyte loss appears to be the detachment of podocytes from the GBM. There are two main causes for podocyte detachment, increased mechanical forces and altered adhesion forces of podocytes to the GBM. Hypertension, hyperfiltration, and/or hypertrophy of the glomerulus can cause increased mechanical stress (Kriz and Lemley 2015).

1.1.2.2 Podocyte and endothelial cell communication in glomerulus

Crosstalk between glomerular cell types is necessary for the establishment and maintenance of the glomerular barrier (Bartlett et al. 2016). Vascular endothelial growth factor (VEGF), endothelial nitric oxide synthase (eNOS), stromal cell–derived factor 1, angiopoietins, semaphorins, and endothelin-1 are factors discovered through loss- and gain-of-function studies as mediating podocyte-endothelial interaction (Reidy et al. 2009; Bartlett et al. 2016; Sol et al. 2020).

VEGF is a crucial regulator of microvascular permeability. In mammals, five members of the VEGF family (VEGF-A, -B, -C, and –D) as well as placental growth factor (PGF) have been identified (Uciechowska-Kaczmarzyk et al. 2018). VEGF-A is produced by the podocytes, whereas the glomerular endothelial cells express VEGF-R1 (Flt-1) and -R2 (Flk-1/KDR) tyrosine kinase receptors that mediate VEGF-A signalling. VEGF-R2 is the only receptor directly involved in both normal and abnormal vascular permeability (Roberts and Palade 1995; Eremina et al. 2003; Koch and Claesson-Welsh 2012). According to their location and gene expression profile, podocytes are necessary for providing glomerular endothelial cell migratory signals for the generation of their fenestrated phenotype to form the renal filtration barrier (Eremina et al. 2006; Satchell

and Braet 2009). Transgenic manipulation of VEGF expression in podocytes indicates that the glomerular endothelial cell phenotypes are extraordinarily sensitive to VEGF. Loss of both VEGF-A alleles from the podocyte reduces endothelial cell migration in developing glomeruli significantly. As a result, the glomerular filtration barrier does not form, and newborn mice develop renal insufficiency and die. Loss of only one of the two VEGF-A alleles results in early fenestration formation, whereas overexpression causes glomerulomegaly, glomerular basement membrane thickening, mesangial expansion, altered permeability and proteinuria (Veron et al. 2011). Thus, maintaining physiological levels of VEGF in the glomeruli is required.

eNOS is one of the three NOS isoforms and is involved in the generation of nitric oxide (NO) in the vascular endothelium. NO generated by eNOS in endothelial cells is a crucial mediator of renal blood flow, glomerular filtration rate, and fluid homeostasis as a potent endogenous vasodilator (Dong and Xu 2022). VEGF-A promotes the VEGFR-2/Akt axis in glomerular endothelial cells to regulate eNOS phosphorylation. eNOS action is triggered by the phosphorylation of serine (Ser1177) by the protein kinase Akt (Fulton et al. 1999; Kim et al. 2011a). eNOS-deficient mice have impaired renal function, glomerular and tubulointerstitial damage and may reveal loss of glomerular and peritubular capillaries. Reduction in NO release by endothelial dysfunction is therefore thought to represent a significant risk factor for the progression of renal disease (Nakayama et al. 2009). Asymmetric dimethylarginine (ADMA) is an endogenous inhibitor of NO synthase. ADMA inhibits nitric oxide synthases, which may explain impaired vasorelaxation, higher inflammation, and decreased angiogenesis in human and in animal models during CKD (Vallance et al. 1992; Sibal et al. 2010). ADMA is metabolised by dimethylarginine dimethylaminohydrolases (DDAH); DDAH-2 is primarily expressed in tissues harboring endothelial NOS. It has been

demonstrated that DDAH overexpression encourages endothelial healing following vascular damage (Leiper et al. 1999; Dobrian 2012).

1.1.3 Renal tubules

The renal tubule of mammals has been subdivided into 14 segments (Figure 5). Sixteen different cell types have been described, each displaying a unique set of functions mostly related to transport and metabolism (Chen et al. 2019a). After its formation in the renal corpuscle the primary urine enters the proximal tubule. The proximal tubule is divided into the convoluted part comprising an early S1 and a late S2 segment located in the cortical labyrinth. The S2 segment is then followed by the proximal straight tubule or S3 segment which is mostly located in the medullary rays of the cortex and in the outer stripe. All proximal segments reveal substantial membrane amplification featuring luminal brush border microvilli and basolateral interdigitation. Both structural landmarks are adaptations to the high transport activity of the proximal tubule achieving 65 to 70% reabsorption of the filtrate. An apical vesicular apparatus is particularly well developed in the proximal convolutions, revealing endocytotic vesicles, endosomes, lysosomes, a recycling apparatus, and cisternae of the smooth endoplasmic reticulum. These are serving functions related with fluid-phase endocytosis, receptor-mediated endocytosis involving megalin/cubulin and clathrin, enzymatic degradation of proteins, recycling of endocytotic vesicles, and exocytosis of membrane bound cell content. Lysosomes harboring non-digestibles may occur as autofluorescent residual bodies to be exocytosed (Alpern et al. 2008). Basolaterally located peroxisomes containing catalase provide a number of functions including the control of oxidative stress, metabolism of glutathione, and lipids biotransformation (Ansermet et al. 2022). High density of mitochondria adjacent to the basolateral membrane foldings mirror the high need for energy to support primary active basolateral transport. The PST has a less-developed vesicular compartment

and combines reabsorptive and secretory functions. While in rat its brush border membrane is more developed than in the convolutions, in humans it is comparatively less developed. Basolateral interdigitations are reduced and the cells display a polygonal pattern.

At the junction between outer and inner stripe of the outer medulla the proximal tubule continues into the descending thin limb which reaches the thick ascending limb directly at the border between outer and inner medulla in short loops, forming a hairpin bend. Alternatively, an ascending thin limb is interposed between descending thin limb and thick ascending limb with the hairpin bend located at different levels of the inner medulla. Thin limbs serve the renal concentrating mechanism with selective solute and water permeabilities and have minor metabolic equipment (Kriz and Kaissling 2008).

The thick ascending limb starts at the border between inner and outer medulla. It is divided into a medullary and a cortical portion. The cortical TAL forms the macula densa at its glomerulus and continues with a short post-maula segment into the distal convoluted tubule. TAL cells show few microvilli and a meandering luminal cell boorder. Basolateral cells are interdigitated with each other in proximity to numerous large, palisade-like mitochondria. An apical vesicular compartment contains Tamm Horsfall proteon for luminal exocytosis. Apical Na-K-2Cl (NKCC2) cotransporter provides transepithelial Na^+ and Cl^- transport, whereas water cannot pass which results on dilution of the tubular urine to below 100 mOsm/kg H_2O in the cortical portion. The macula desa consists of approximately 20 polygonal cells functioning to sense the chloride load in the filtrate and control the tubuloglomerular feedback (Ares et al. 2011).

The distal convoluted tubule is short, has a similar structure as the TAL, also not water permeable, and expresses apical NaCl cotransporter (NCC) at the luminal cell pole. Its function is the fine tuning of natriuresis, calcium and magnesium excretion; it also contributes importantly to plasma potassium homeostasis (Subramanya and Ellison

2014). The ensuing connecting tubule (CNT) displays a hybrid phenotype between distal nephron and collecting duct, and is located near the interlobular vasculature. It may transport sodium via the epithelial Na^+ channel (ENaC) in the CNT principal cells. A second cell type, the intercalated cell, is involved in acid-base regulation. All CNT cells are cuboid to polygonal. The following collecting duct (CD) has a similar architecture as the CNT with characteristic occurrence of intercalated cells depending on the parenchymal zones (Pearce et al. 2015; Rao et al. 2019).

Both CNT and CD respond to vasopressin (antidiuretic hormone, ADH) by membrane insertion of aquaporin water channels in the principal cells. Transepithelial diffusion along the interstitial osmotic gradient then moves water out of the lumen to the interstitium. Aldosterone-sensitive sodium reabsorption via ENaC is coupled to luminal secretion of potassium via the K^+ channel, ROMK of principal cells (Kortenoeven et al. 2015).

1. Glomerulus: podocyte (PODO), parietal epithelial cell, mesangial cell, glomerular endothelial cell

2. Proximal convoluted tubule (PCT cell)

3. Proximal straight tubule (PST cell)

4. Descending thin limb of Henle's loop (DTL1, DTL2, and DTL3 cells)

5. Ascending thin limb of Henle's loop (ATL cell)

6. Thick ascending limb (TAL) of Henle's loop: medullary (MTAL cell) and cortical (CTAL)

7. Macula densa (MD) cell (very low abundance in whole kidney)

8. Distal convoluted tubule (DCT) cell (divided into DCT1 and DCT2 cells in some species)

9. Connecting tubule (CNT) cell, type B intercalated cell (B-IC), non-A, non-B intercalated cells

10. Cortical collecting duct: Principal cell (PC), type B intercalated cell (B-IC), type A intercalated cell (A-IC)

11. Outer medullary collecting duct: Principal cell (PC), type A intercalated cell (A-IC)

12. Inner medullary collecting duct: IMCD cell

Figure 5. Renal tubule cells. The diagram shows how both a short-looped nephron and a long-looped nephron are connected to the system of collecting ducts. The numbers show to different parts of the kidney's tubules, and to the right of the scheme is a list of the types of cells that each segment has. Regions are separated by dashed lines. Adapted from (Chen et al. 2019a).

1.1.4 Renal interstitium

The renal interstitium is the narrow space between nephron and vasculature. It contains small bundles of collagen 1 fibres, interstitial fibroblasts, dendritic cells and few macrophages. The cortical interstitium characteristically contains the 5' ectonuceotidase-positive fibroblasts which may release erythropoietin upon an adequate stimulus. The inner medullary interstitium is characterized by the lipid-laden interstitial cells involved in prostaglandin synthesis (Kaissling and Le Hir 2008).

1.2 Renal transplantation

Today, transplantation of one kidney is still the optimal therapy for patients with end-stage renal disease (Suthanthiran and Strom 1994; Tonelli et al. 2011). The first successful renal transplantation was performed by Joseph E. Murray and colleagues

in 1954 in Boston, USA. Donor and recipient were identical twins (Merrill 1956). Allograft rejection causing graft loss acutey was common as the primary challenge during the following two decades. Alloreactive T cells may cause acute and chronic rejection, and the current clinical objective is to prevent them from overreacting against the allograft (Adler and Turka 2002). Therefore, efficient suppression of the alloimmune response by the use of immunosuppressive treatments has become a successful medication in transplantation. Tretament has developed over the years, starting with total body irridation followed by the application of 6-mercaptopurine, corticosteroids or azathioprine, but by high rejection rates, related to their toxicity, prevailed (Taylor et al. 2005). A major advancement came from the discovery of the calcineurin inhibitors, cyclosporine A and, later, tacrolimus in the 1980s (Kapturczak et al. 2004).

1.2.1 Calcineurin inhibitors

Since their introduction into clinical practice, the use of calcineurin inhibitors (CNIs) in the prevention of organ graft rejection after transplantation has significantly improved graft and patient survival (Ume et al. 2021).

Cyclosporine A (CsA) was first isolated in 1970 from *Tolypocladium inflatum* (Borel et al. 1976). CsA is a neutral lipophilic cyclic endacapeptide (Kapturczak et al. 2004). Tacrolimus (FK506, Tac) is a macrolide compound isolated from *Streptomyces tsukubaensis* in 1984 (Christians et al. 1992; Kino and Goto 1993).

When antigen is delivered to the T-cell receptor by an antigen presenting cell during immune response, intracellular Ca^{2+} rises to activate calcineurin, a serine/threonine protein phosphatase. Transcription factor nuclear factor of activated T cells (NFAT), which is hyperphosphorylated at multiple serine/threonine residues in cytosol, is a target of calcineurin to be translocated to the nucleus upon dephrosphorylation (Figure 6). Interleukin-2 (IL-2), essential cytokine for T cell activation, then becomes released. (Medyouf and Ghysdael 2008; Otsuka et al. 2021).

CsA and Tac are the most specific and well-established inhibitors of calcineurin. Despite their completely different chemical structures, the biological effects and modes of action of CsA and Tac are strikingly similar. CNIs target calcineurin indirectly. Due to their hydrophobic nature, they can diffuse across the plasma membrane to interact with their intracellular immunophilin receptor proteins such as cyclophilin (Cyp) and FK-binding protein 12 (FKBP12). These immunophilins are categorized based on their capacity to selectively bind specific immunosuppressive drugs modulating their actions. CsA binds to Cyp, Tac to FKBP12 with high affinities (Figure 6). CNI-immunophilin complexes then bind to calcineurin to inhibit its phosphatase activity. (Martinez-Martinez and Redondo 2004; Azzi et al. 2013; Ume et al. 2021; Otsuka et al. 2021).
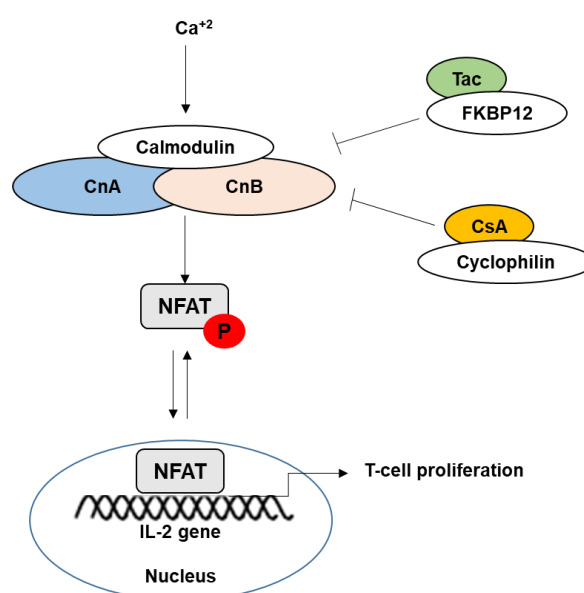
Figure 6. The mechanism of calcineurin inhibitors. Calcineurin inhibitors (CNIs) blunt the immune response by inactivating calcineurin phosphatase activity. CsA and Tac bind to cytosolic cyclophilin and FKBP12, respectively. The resulting CNI-immunophilin complexes bind to the active site of calcineurin and inhibit its phosphatase activity. Following inhibition, transcription factors like nuclear factor of activated T cells (NFAT) cannot be activated via dephosphorylation. This inhibits immunological activation by preventing NFAT translocation into the nucleus to enhance IL-2 production (Own design).

1.2.2 Calcineruin structure and function

Calcineurin is a heterodimeric protein composed of the catalytic subunit, calcineurin A (CnA, 60 kDa), and the Ca^{2+}-binding component, calcineurin B (CnB, 19 kDa) (Creamer 2020). Calcineurin is conserved in mammals and is particularly abundant in human brain (Martinez-Martinez and Redondo 2004). The kidney also contains calcineurin abundantly (Rusnak and Mertz 2000). It plays crucial roles in several signaling cascades, regulating transcription factors, dynamic structural proteins and ion channels (Jorgensen et al. 2003; Creamer 2020).

Calcineurin dephosphorylates and regulates the activity of transcription factors such as NFAT, forkhead (FOXO), myocyte-specific enhancer factor 2 (MEF2), and transcription factor EB (TFEB) (Creamer 2020). TFEB regulates autophagic flow by promoting lysosome biogenesis, autophagosome formation and fusion with lysosomes in the context of cell substrate clearance. It is also functionally involved in lysosomal exocytosis (Zhang et al. 2020). In the glomerulus, synaptopodin, an actin stabilizer in podocytes, is subject to dephosphorylation by calcineurin as well which induces cathepsin-L mediated degradation (Vassiliadis et al. 2011).

1.2.3 CNI neprotoxicity

The considerable side-effects associated with CNI treatment menace long-term kidney graft survival and may cause significant increases in morbidity. Even though CsA and Tac have a similar mechanism of action, their toxicity profiles may differ (Azzi et al. 2013). CsA regimen is known to cause hyperuricemia, gingival hyperplasia, hirsutism, and higher hyperlipidemia than Tac whereas Tac has been associated with the development of post-transplant diabetes, hyperkalemia as well as the occurrence of neurological problems (Farouk and Rein 2020). CNI nephrotoxicity may be divided into characteristic acute phase damages which may be reversible, and chronic, irreversible

nephropathy which may affect all tissue compartments of the kidney including arterioles, glomeruli and tubulo-interstitium (Liptak and Ivanyi 2006).

Acute CNI nephrotoxicity is characterized by hemodynamically mediated renal dysfunctions, which are usually reversible with consequent dosage reduction or exchange of CNI with an alternative immunosuppressant regimen (Chapman 2011). The most common symptoms of acute nephrotoxicity include acute afferent arteriolopathy (endothelial swelling; necrosis and early-stage hyalinosis), reduced glomerular filtration rate, tubulopathy (isometric vacuolization in proximal tubule), and less commonly, thrombotic microangiopathy (Morozumi et al. 2004; Naesens et al. 2009b; Bentata 2020).

Chronic CNI nephrotoxicity is characterized by irreversible damages to renal architecture and function. Commonly, arteriolar hyalinosis, glomerular affections such as thickening of Bowman´s capsule and focal segmental to global glomerulosclerosis, and interstitial fibrosis/tubular atrophy (IF/TA) occur (Young et al. 1995; Cattaneo et al. 2004; Williams and Haragsim 2006). Hyaline arteriolopathy is commonly regarded as a hallmark of both, CsA and Tac nephrotoxicities. The lesions affect small arteries and arterioles which reveal media necrosis and nodular hyaline deposits eventually narrowing the lumen (Mihatsch et al. 1998; Liptak and Ivanyi 2006). Local inactivation of calcineurin-NFAT signaling pathways is thought to be causally involved (Graef et al. 2001). Associated vasoconstriction causing local hypoxia or ischemia is further thought to drive glomerulosclerosis and IF/TA. Inadequate activation of renin-angiotensin system (RAS) leading to renin overexpression and enhanced angiotensin II release have been implicated in glomerular dysfunction, inflammation and fibrosis. Angiotensin converting enzyme inhibition or angiotensin receptor blockers have therefore been considered to reduce CNI nephrotoxicity (Hošková et al. 2017). CNI-induced RAS activation via renin overexpression and enhanced angiotensin II release have indeed

been implicated in glomerular dysfunction, inflammation and fibrosis (Calò et al. 2017; Mortensen et al. 2017; Chou et al. 2018). Dysbalance between vasoconstrictive and vasodilatory mediators other than angiotensin, i.e., endothelin and NO, may further be involved (Kurtz et al. 1988; Lamas 2005; Azzi et al. 2013). Interstitial hypoxia has been assumed to exacerbate parenchymal damage via reactive oxygen species (ROS) causing oxidative stress with consequent cellular apoptosis (Naesens et al. 2009a; Pallet et al. 2011; Honda et al. 2019). The production of ROS from mitochondria is known to destroy mitochondrial and general cellular structure, driving cells into apoptosis (Jeon et al. 2005; Yuan et al. 2020). Overexpression of transforming growth factor-β (TGF-ß), promoting interstitial fibrosis, has been reported in this context as well (Akool et al. 2008; Ume et al. 2021).

A link between CNI and defective protein biosynthesis has further been established in patient biopsies and cell models with a focus on endoplasmic reticulum (ER) stress and the unfolded protein response (UPR) (Yilmaz et al. 2022a). Impaired protein folding leads to accumulation of misfolded proteins in the ER and activates a compensatory intracellular signaling pathway, UPR. UPR consists of three main branches with PKR-like ER kinase (PERK), inositol-requiring enzyme 1 α (IRE1α), and activating transcription factor 6 (ATF6) sensing the respective pathways. These are bound to binding immunoglobulin protein (BiP or GRP78) which is inactive under normal, non-stressed condition. When misfolded proteins accumulate in the ER, BiP is recruited to attach to unfolded proteins, thereby activating the sensors. ER-associated degradation is enhanced following splicing of transcription factor called X-Box binding protein 1 (XBP1). Translation decreases due to the phosphorylation of eukaryotic translation initiation factor 2 subunit-α (eIF2α), reducing the ER workload. However, if ER stress becomes overwhelming or prolonged, UPR can activate apoptotic pathways

through the proapoptotic transcription factor C/EBP homologous protein (CHOP) and

caspases (Figure 7) (105).
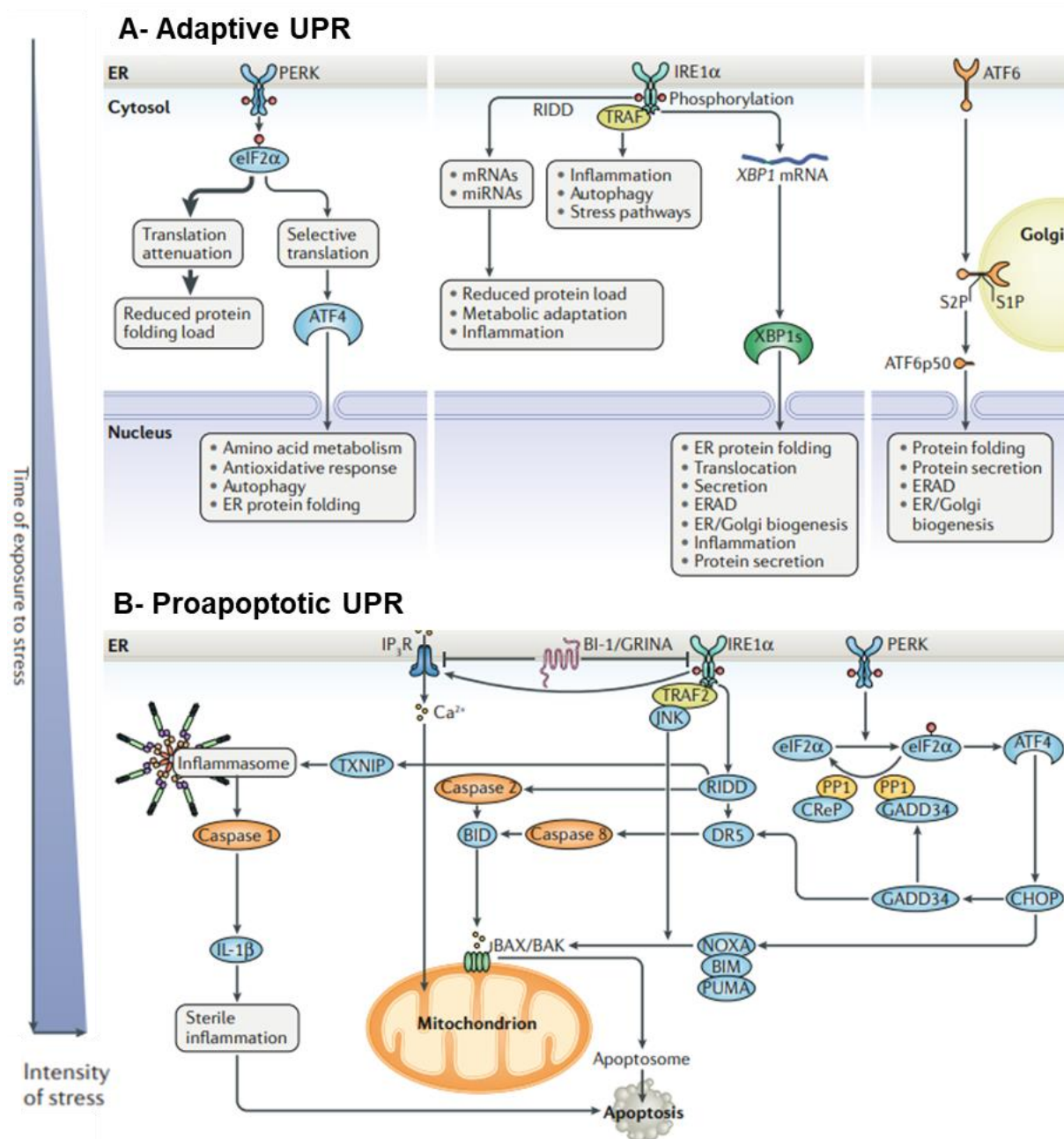
Figure 7. Unfolded protein response (UPR) pathway. A- Adaptive UPR. B- Proapoptotic UPR. Figure 7 is adopted from (Hetz and Papa 2018).

Renoprotective experiments in cultured mouse proximal tubular cells in fact provided

evidence that CsA toxicity was initially evident by pronounced ER stress which resulted

in ROS production, phenotypic alterations, and apoptosis (Sarró et al. 2012). *In vivo*

and *in vitro* experiments have shown epithelial phenotypic alterations that result in the

production of protomyofibroblasts and cellular damage in tubular cells (Pallet et al. 2008c; Pallet et al. 2008a; Bouvier et al. 2009). CsA hinders the ability of cyclophilins to fold proteins and causes UPR in the proximal tubule. Several lines of evidence suggest that CsA-toxicity associates with impaired proteostasis which in turn triggers maladaptive UPR and apoptosis, which is at variance to Tac (Kitamura 2010; Fedele et al. 2020).

UPR can regulate autophagy-related genes and modulate several kinases including the master regulators, adenosine monophosphate-activated protein kinase (AMPK) and mammalian target of rapamycin complex 1 (mTORC1) (Rashid et al. 2015; Ren et al. 2021). CNI nephrotoxicity is associated with impaired autophagy pathways (Pallet et al. 2008b; Li et al. 2021). Autophagy is a lysosomal-dependent catabolic process that plays a critical role in cellular adaptation to starvation and other forms of cellular stress through endolysosomal degradation and removal of misfolded proteins and other hazardous potentially components. Its membrane formations, creating autophagosomes, include initiation, elongation, maturation, and destruction phases. Its activity is also essential for cell division, differentiation, tumor suppression, innate and adaptive immunity, and cell death (Mizushima and Klionsky 2007). AMPK promotes autophagy by inhibiting the mTORC1 activity and phosphorylates Atg1/unc-51 like autophagy activating kinase 1 (ULK1) at several Ser residues to initiate autophagy. Through modulating the activity of ULK1 complex, mTOR inhibits autophagy by its phosphorylation at ser757 (Kim et al. 2011b; Al- Bari and Xu 2020). The final stage of the autophagy pathway is autophagosome-lysosomal fusion. The preservation of autophagic flux is directly related to the integrity of this process. Autophagosomes accumulate due to incomplete maturation and deficiencies in lysosome proteolysis capacity (Li et al. 2021). During endocytosis early and late endosomes are generated which eventually fuse with the lysosomes to form

endolysosomes with the characteristic capacities. These double-membrane bound organelles are involved in breaking down and recycling cell components by means of >60 hydrolases specific for their respective substrates including lipids, polysaccharides and proteins (Xu and Ren 2015). Lysosomal exocytosis may occur via their fusion with the plasma membrane for waste removal. (Perera and Zoncu 2016). ER stress response has further been linked to TFEB and TFE3 activation via PERK in a mTORC1- independent manner (Martina et al. 2016a). TFEB, substrate to calcineurin, regulates lysosomal biogenesis and exocytosis as well as autophagosome and autolysosome formation (Settembre et al. 2011; Medina et al. 2011; Paquette et al. 2021). In nutrient-rich condition, mTORC1 blocks its activity by phosphorylation, preventing its entry to the nucleus. In contrast, its nuclear translocation occurs during starvation, when endolysosomal calcium efflux via mucolipin 1 (MCOLN1) activates calcineurin to dephosphorylate TFEB (Martina et al. 2012).

1.3 Aim of the thesis

CNIs such as CsA and Tac are commonly used as immunosuppressive drugs after organ transplantation. Despite the short-term success, chronic use of CNIs may cause renal damage resulting in compromised renal allograft function. Although attempts have been made to eliminate or substitute CNIs with other immunosuppressants, the alternatives to CNIs are generally considered less effective. CsA and Tac have similar effects related with immunosuppression but differ with respect to their distinct degree of nephrotoxicity so that their impact on eventual renal dysfunction and pathology merits further evaluation. The aims of this study are:

Aim 1. To develop an *in vivo* rat model of gradually developing stages of CNI nephropathy by adequate drug application and dose tritration.

Aim 2. To use this model for the histological study of how CsA and Tac exposures affect the particular renal compartments differentially in gradually developing stages of nephropathy.

Aim 3. To include a multi-omics approach using transcriptomics, proteomics and phosphoproteomics for identification of mechanisms and associated biomarkers upon CsA vs. Tac.

2. Materials and methods

2.1 Materials

Materials are the machine, device, software, chemicals, solutions and other consumables used during the experiment.

2.1.1 Equipment

Table 1. List of devices.

Instrument	Company
Bioanalyzer 2100 system	Agilent
ECL Chemocam Imager	Chemostar, Intas Science Imaging Instruments
Electrophoresis Bio-Rad Power Pac 200	Bio-Rad Laboratories
Eppendorf ThermoMixer	Eppendorf
FEI TEM Tecnai G2	FEI
Leica RM 2125RT paraffin microtom	Leica Microsystems
LSM 5 Exciter confocal microscope	Carl Zeiss Microscopy
Microplate reader ASYS Expert 96	BioChrom
MIKRO200R centrifuge	Andreas Hettich
Mini-PROTEAN Tetra Vertical Electrophoresis Cell	Bio-Rad Laboratories
NanoPhotometer nanodrop	Implen
Novaseq HisEquation 4000 platform	Illumina
pH-Meter Knick 766 Calimatic	Knick
Q Exactive HF-X MS	Thermo Scientific
Sonoplus GM70 sonicator	BANDELIN electronic
timsTOF Pro 2 LC-MS/MS	Brucker
Ultimate 3000 RSLCnano	Thermo Scientific
Ultracut E ultramicrotome	Reichert Jung
ZEISS Axio Imager VarioUpright Microscope	Carl Zeiss Microscopy
Zeiss TEM 906 Leo	Carl Zeiss Microscopy

2.1.2 Chemicals, and commercial kits

Table 2. List of chemicals and kits.

Product	Supplier
3,3'diaminobenzidine (dab)	Sigma Aldrich
4',6-diamidino-2-phenylindol (dapi)	Sigma Aldrich
ACN	Thermo Fisher Scientific
Acrylamide solution 30%	Carl Roth

Ammonium persulfate (APS)	Carl Roth
Ammoniumbicarbonat	Carl Roth
Benzonase	Sigma Aldrich
Bovine serum albumin (BSA)	SERVA Electrophoresis
Bromophenol blue	Carl Roth
Chloroform	Merck
Cyclosporin A (Sandimmun)	Novartis
Difco skim milk	Becton, Dickinson
Dimethylsulfoxid (DMSO)	Sigma Aldrich
ECL chemiluminescence	GE Healthcare
Ethanol absolute	Merck
Eukitt Quick-hardening mounting medium	Sigma Aldrich
Formalin	Thermotex
Glycin rotipuran	Carl Roth
Hematoxylin solution, Mayer`s	Sigma Aldrich
HEPES	Carl Roth
Hydrogen peroxide (H$_2$O$_2$)	Sigma Aldrich
Hydroxyethyl starch (HES)	AK Scientific
Isofluran (100%)	Abbott
Isopropanol	Merck
Ketamin	CP-Pharma
Lysc Lysyl Endopeptidase	FUJIFILM Wako Chemicals
Methanol	Merck
MgCl	Sigma Aldrich
Na-cacodylate (Caco),	Serva
Nebnext RNA Library Prep Kit	New England BioLabs
Osmotic minipumps, 2ML4	Alzet
Paraformaldehyde (PFA)	Merck
PEG500	Sigma Aldrich
Peqgold trifast	VWR Life SCIENCE
Periodic acid reagent	Sigma Aldrich
PhosSTOP phosphatase inhibitor tablets	Roche Diagnostics
Polyvinylidene difluoride (PVDF)	Macherey-Nagel
Proteinase inhibitor cocktail tablets, complete	Roche Diagnostics
Protein marker precision plus protein dual color standard	Bio-Rad
Random hexamer primer	Bioline
RNA Nano 6000 assay kit	Agilent
SDS	Carl Roth
Sep-pak® c18 cartridges	Waters
Sodium azide	Merck
Sodium chlorid	Merck
Sodium citrate	Merck
Sodium dihydrogenphosphate	Merck
Sodium hydrogencarbonate	Merck
ß-mercaptoethanol	Sigma Aldrich

Sucrose	Carl Roth
Tacrolimus (FK506)	Selleckchem
TCEP	Sigma Aldrich
Tetramethylethylendiamin (TEMED)	Bio-Rad
TMT10	Thermo Fisher Scientific
TMTpro	Thermo Fisher Scientific
Triethanolamin (TEA)	AppliChem, PanReac, ITW Reagents
Tris-Base	Merck
Tris HCl	Merck
Triton X-100	Merck
Tween 20	SERVA Electrophoresis
Tyrpsin	Promega
Xylavet	Cp-Pharma
Xylene	Sigma Aldrich

2.1.3 Buffers and solutions

Table 3. List of buffers and solutions.

Buffer/solution	Composition
3% Paraformaldehyde solution	30 g paraformaldehyde and 90 ml distilled water mixed on a hot plate at 60 °C under a fume hood, ph 7.4
5% BSA/TBS	5 g BSA, 100 mL 1X TBS
5% Milk/TBS	5 g skim milk, 100 mL 1X TBS
Blocking solution for immunohistochemistry	1 g BSA, 0.1 g fish gelatin, 1 g normal goat serum, 100 ml 1X PBS
Electrophorase running buffer, 10X	0.25 M Tris-Base, 1.92 M glycin, 1% SDS, dissolved in 1L distilled water, ph 8.3
Gel buffer	3 M Tris-Base, 0.3% SDS, dissolved in 1 L distilled water, ph 8.45
Homogenization buffer	250 mM sucrose, 10 mM TEA, complete protease inhibitor cocktail tablet, PhosSTOP phosphatase inhibitor cocktail tablet, ph 8.45, 100 ml distilled water
Laemmli SDS loading buffer, 4X	252 mM Tris/HCl, 40% glycerin, 8% SDS, 0.04% bromphenol blue, 20% β-Mercaptoethanol, ph 6.8
Na-cacodylate, 0.1M	21.4 g Sodium cacodylate dissolved in 1 L distilled water, ph 7.4
Perfusion buffer	3% hydroxyethyl starch, 0.1 M Na-cacodylate, 3% paraformaldehyde, 1 L distilled water, ph 7.4
Phosphate-buffered saline (PBS), 10X	400 g NaCl, 12 g KH2PO4, 89 g Na2HPO4, 10 g KCl, dissolved in 5 L distilled water, ph 7.4
Separating gel, 10%, Western Blot	7 ml acrylamid, 7 mL gel buffer, 2.5 mL glycerol, 4 mL distilled water, 200 µL APS, 10 µL TEMED
Stacking gel, Western Blot	1 ml acrylamid, 2 mL gel buffer, 5 mL distilled water, 100 µL APS, 10 µL bromphenol blue, 10 µL TEMED
Transfer buffer, 10X	30 g Tris-Base, 144 g glycine dissolved in 1 L distilled water
Transfer buffer, 1X	100 ml 10X transfer buffer, 100 mL methanol, 800 mL distilled water
Tris-Buffered Saline (TBS), 10X	24.2 g Tris-Base, 80 g NaCl, dissolved in 1 L distilled water, ph 7.6

2.1.4 Softwares

Table 4. List of softwares.

Software	Company
ChemoStar Imager 2015	INTAS Science Imaging Instruments
GraphPad Prism 8	GraphPad Software Inc.
ImageJ	National Institutes of Health
MaxQuant version 1.6.7.0	MaxQuant, Perseus, and related software packages are developed by the Computational Systems Biochemistry (Max Planck Institute for Biochemistry, Martinsried, Munich) under Prof. Jürgen Cox.
Microsoft Office	Microsoft Corporation
R statistical programming software (version 4.1.1)	R Foundation for Statistical Computing, Vienna, Austria. URL: https://www.R-project.org/.
Zen Version 8	Carl Zeiss MicroImaging

2.1.5 Antibodies

Table 5. List of primary antibodies.

Antibody	Host & Clonality	Company	Catalogue Nr	Dilution IHC	Dilution WB
Anti-CD44	rabbit, monoclonal	Abcam	ab189524	1:2000, 5% BSA in TBS	
Anti-phospho-AMPKα (Thr172)	rabbit, polyclonal	Cell Signaling Technology	2531		1:1000, 5% BSA in TBS
Anti-phospho-mTOR (Ser2448)	rabbit, polyclonal	Cell Signaling Technology	2971		1:1000, 5% Milk in TBS
Anti-α-sma	mouse, monoclonal	Sigma-Aldrich	A2547	1:1000, 5% BSA in TBS	
Anti-AMPK	mouse, monoclonal	Invitrogen	MA5-15815		1:1000, 5% BSA in TBS
Anti-catalase	rabbit, polyclonal	Abcam	ab217793	1:3000, 5% BSA in TBS	
Anti-CD31	goat, polyclonal	R&D Systems	AF3628	1:500, 5% BSA in TBS	1:1000, 5% BSA in TBS
Anti-CD45	Rabbit, polyclonal	Abcam	ab10558	1:1000, 5% BSA in TBS	
Anti-cleaved caspase 3	rabbit, polyclonal	Cell Signaling Technology	9661		1:500, 5% BSA in TBS
Anti-integrin alpha 3	goat, polyclonal	Abcam	ab223661	1:2000, 5% BSA in TBS	
Anti-KIM1	goat, polyclonal	R&D Systems	AF3689	1:800, 5% BSA in TBS	
Anti-LAMP1	rabbit, polyclonal	Abcam	ab24170	1:2000, 5% BSA in TBS	
Anti-mTOR	rabbit, polyclonal	Cell Signaling Technology	2983		1:100, 5% BSA in TBS
Anti-phospho-	rabbit, polyclonal	Abcam	ab48187		1:1000, 5% BSA in TBS

IRE1α (phospho S724)					
Anti-phospho-PERK (Thr980)	rabbit, monoclonal	Cell Signaling Technology	3179		1:1000, 5% Milk in TBS
Anti-podocin	rabbit, polyclonal	Sigma-Aldrich	P0372	1:2000, 5% BSA in TBS	
Anti-renin	sheep, polyclonal	Acris	AP00945PU-N	1:1000, 5% BSA in TBS	
Anti-ß-actin	mouse, monoclonal	Sigma	A2228		1:20000, 5% BSA in TBS
Anti-sXBP1	rabbit, monoclonal	Abcam	ab220783		1:1000, 5% BSA in PBS
Anti-TFEB	goat, polyclonal	Abcam	ab2636		1:1000, 5% BSA in PBS
Anti-Wilms tumor protein-1 (WT-1)	rabbit, monoclonal	Abcam	ab89901	1:500, 5% BSA in TBS	

Table 6. List of secondary antibodies.

Secondary antibodies	Host & Clonality	Company	Catalogue Nr
Cy2-coupled donkey anti-goat IgG	donkey, polyclonal	Dianova	705-225-147
Cy2-coupled donkey anti-mouse IgG	donkey, polyclonal	Dianova	715-225-150
Cy2-coupled donkey anti-rabbit IgG	donkey, polyclonal	Dianova	711-225-152
Cy3-coupled donkey anti-goat IgG	donkey, polyclonal	Dianova	705-165-147
Cy3-coupled donkey anti-mouse IgG	donkey, polyclonal	Dianova	715-165-150
Cy3-coupled donkey anti-rabbit IgG	donkey, polyclonal	Dianova	711-165-152
Polyclonal goat anti mouse HRP		Dako	P0447
Polyclonal rabbit anti goat HRP		Dako	P044901-2
Polyclonal swine anti rabbit HRP		Dako	P0217

2.2 Methods

2.2.1 Animals

Animal experiments were carried out in accordance with the National Institute of Health guidelines in compliance with the German Animal Welfare Act and were approved by the State Office for Health and Social Affairs Berlin (application for animal experiments G0148/18). All animals were maintained in confined, air-conditioned rooms at 22 °C to 24 °C with a 12-hour day-night cycle, with ad libitum access to drinking water and standard rodent chow. The animals had unlimited access to water and food. Adult male Wistar rats around 10 to 12 weeks old and weighing more than 250 grams were

separated into four groups (n=6) receiving CsA (30 mg/kg b.w./d, Sandimmun, Novartis, Nürnberg, Germany; target plasma trough level 3 µg/ml) or the respective vehicle (saline), or Tac (2 mg/kg b.w./d, FK506, Selleckchem, Houston, TX, USA; target plasma trough level 3.5 ng/ml) or the respective vehicle (25% DMSO/75% PEG500, Sigma-Aldrich) via subcutaneously implanted osmotic minipumps (Alzet, 2ML4) for 4 weeks. Isoflurane inhalation was used to anesthetize animals before minipump implantation. To make space for the minipump, a skin incision on the neck was made, and the subcutaneous tissue was dilated. The pocket was then sealed up with metal clips once the filled pump was placed in. For physiological analysis, rats were kept in metabolic cages with access to food and water for 24 h on the second last day of each experiment in order to collect urine. On the last day, blood samples were collected from inferior vena cava after animals were anesthetized with Ketamin/Xylavet (90/10mg/kg b.w.; CP-Pharma GmbH, Germany) and laparotomy was performed. Urine and blood samples were evaluated by a commercial laboratory (IMD Labor Berlin, Germany). Before *in vivo* perfusion fixation, one kidney was clamped and removed for biochemical investigation, and the other kidney perfused with fixative. Alternatively, both kidneys were removed without fixation for biochemical analysis.

2.2.2 Blood and urine analysis

Using heparinized syringes, blood samples were drawn from the inferior vena cava, transferred into mini centrifuge tubes, allowed to clot for 30 min at room temperature (RT), and then centrifuged at 2000 × g for 10 min at 4 °C to separate the serum from the supernatant. Creatinine clearance (CrCl) was calculated calculated using the formula, CrCl (mL/min) = (urine creatinine [mg/dL] × urine flow [mL/min] / serum creatinine [mg/dl]). Fractional excretion of sodium (FeNa) was determined by the formula FeNa (%) = (urinary sodium [mg/dL] × serum creatinine [mg/dl]) / (serum sodium [mg/dl] × urinary creatinine [mg/dL]).

2.2.3 Perfusion fixation and tissue processing

Kidneys were perfused via the abdominal aorta for 20 to 30 seconds with 3% hydroxyethyl starch in 0.1 M Na-cacodylate buffer (Caco), followed by 5 minutes with 3% paraformaldehyde/3% hydroxyethyl starch in Caco. After that, kidneys were removed and dissected into halves or small pieces and then stored in PBS/sucrose (330 mOsm/kg) added with 0.02% NaN$_3$. For histology, kidneys were paraffin embedded after overnight postfixation in paraformaldehyde at 4 °C or, directly after perfusion, transferred to 800 mOsm sucrose in Caco at 4 °C overnight, frozen in 2-methyl butane, then in liquid nitrogen and stored at -80 °C for cryostat sectioning. For transmission electron microscopy (TEM) and scanning electron microscopy (SEM), tissues were post-fixed overnight at RT in 1.5% glutaraldehyde/1.5% paraformaldehyde containing 0.05% picric acid in Caco, then in 1% osmium tetroxide/0.8% potassium hexacyanoferrate in Caco for 1.5 h at RT for TEM, or in 1% aquaeous osmium tetroxide for SEM. Following dehydration, tissues were embedded in epoxy resin for semithin sectioning and light microscopy (LM) inspection, or for ultrathin sectioning and TEM examination. Samples for SEM were high-pressure critical-point dried and sputter-coated.

2.2.4 Histology and immunostaining

For immunohistochemistry (IHC), paraffin blocks were cut in 2-4 μm sections using a microtome (Leica RM2125RT, Leica Microsystems, Wetzlar, Germany), mounted on glass slides (Super Frost Plus, R. Langenbrinck GmbH, Germany). Sections were dewaxed with xylene (histological grade, Sigma-Aldrich) and rehydrated with a descending series of ethanol (100%, 96%, 80%, and 70%, histological grade, Sigma-Aldrich). Heat-induced antigen retrieval was performed by cooking the sections in citrate buffer (0.02 M citric acid, 0.09 M sodium citrate; pH 6) for 6 min a using pressure cooker and then placed in Tris buffered saline (TBS) to cool down. After another 5 min

washing step in TBS, non-specific antigens were blocked in 5% bovine serum albumin (BSA; Serva, SERVA Electrophoresis GmbH, Germany) or 5% skim milk (Sigma-Aldrich) in TBS for 30 min at RT. The respective primary antibody was diluted in blocking medium, applied and incubated in a humidity chamber at 4 °C overnight. Following a TBS wash, fluorescently labeled secondary antibodies were dissolved in 1% BSA/TBS and incubated at room temperature for 2h. 4,6-Diamino-2-phenylindol (DAPI) was used to stain nuclei (Sigma-Aldrich). Sections were then mounted in a PBS-glycerol (1:9) solution. For Immunoperoxidase staining, 4µm paraffin sections were dewaxed in xylene and rehydrated via grading ethanol series. Heat-induced epitope retrieval was conducted for 6 min in citrate buffer, pH 6, using a pressure cooker. After that sections were incubated in methanol (Merck, Darmstadt, Germany) containing 3% hydrogen peroxide (H_2O_2, Sigma-Aldrich), for 15 min in the dark, then washed in TBS. Next, 5% BSA/TBS was used as blocking solution (at 37 °C for 30 min) and than sections were incubated with primary antibody (antibodies listed in Table 5) at 4 °C overnight, followed by horseradish peroxidase (HRP)-conjugated secondary antibody diluted in 1% BSA/TBS for 1h at RT. 3,3'Diaminobenzidine (DAB, D8001, Sigma-Aldrich) containing 1% H_2O_2 was applied as chromogen. Staining was observed under the light microscope; reaction was terminated by rinsing with TBS. The samples were then dehydrated in a series of ascending concentrations of ethanol, cleared with xylene, and mounted in Eukitt Quick-hardening mounting medium (Sigma-Aldrich).

2.2.5 Microscopy and image processing

Fluorescence images were acquired, some of them with additional differential interference contrast (DIC) overlay using a Zeiss LSM 5 Exciter confocal microscope (LSM, Carl Zeiss Microscopy GmbH, Germany) equipped with an Imager.M1 stand and a NeoFluar oil immersion objective lens (40×63×/NA 1.3/1.4). The confocal microscope was equipped with 405, 488, 543, and 633 nm laser lines and operated

with Zen 2008 software. Brightfield images were taken with a Zeiss Axio Imager Z2 LM equipped with an ApoTome2 structured illumination acquisition system and a Plan-Apochromat 20x/0.8 objective and Zeiss ZEN 2012 software (blue edition). Image processing was performed entirely with ImageJ (National Institutes of Health, USA).

2.2.6 Morphometric analysis

In all evaluations, at least n=4 rats per group were assessed. All evaluations were performed in a blinded manner by a single operator. Quantification of α-SMA and renin were performed on immunoperoxidase stained sections, with hematoxylin nuclear counterstaining. α-SMA- and renin-immunoreactive regions of interest (ROI) were assessed using ImageJ on at least 15 non-overlapping optical fields. The average ROI-to-optical-field ratio (200× magnification) was calculated and graphed.

WT-1 immunofluorescence labeling on whole-kidney images was used on paraffin sections to count glomerular podocyte numbers. The number of podocytes per glomerulus was estimated from all glomeruli (at least 220 glomeruli per kidney/per animal).

Glomerular endothelial fenestral pore density was assessed in TEM per µm of GBM length; total length of GBM measured per animal was >750 µm. At least 6 glomeruli were examined per animal. Likewise, fenestration density of the cortical peritubular capillaries per µm of endothelial basement membrane length was measured over a total length >850 µm by TEM; 10 cross-sectional profiles were examined for each animal.

The mean glomerular tuft area was measured by using anti-podocin-stained paraffin sections from whole-kidney imaged with 3D-structured illumination microscopy (3D-SIM). The number of glomeruli that were analyzed per section ranged from 182 to 343. All accessible glomeruli with easily recognizable vascular pole were used. The podocin-immunoreactive region was measured in µm2 (NIPOKA, Greifswald).

Tubular anti-catalase immunofluorescence staining was quantified in 10 optical fields with at least 3 to 5 PCT profiles per slide and animal at 200× magnification were randomly chosen. Pinhole, laser, offset gain, and detector amplification below pixel saturation adjustments were all kept constant. Using ImageJ, the average catalase fluorescence intensity per PCT was calculated.

2.2.7 Filtration Slit Density Analysis

Dewaxed and rehydrated kidney paraffin sections (2 µm) were cooked in Tris-EDTA buffer (10 mM Tris, 1 mM EDTA, pH 9) for 5 min in a pressure cooker for antigen retrieval. Sections were transferred to blocking solution made (1% BSA, 0.1% fish gelatin, and 1% normal goat serum) for 1h at RT. Primary antibodies were then incubated overnight at 4 °C. After washing in PBS, secondary antibodies were applied for 1 h at RT. Nuclei were counterstained with DAPI. As a final step, sections were rinsed with distilled water and mounted in Mowiol 4-88 (Carl Roth, Karlsruhe, Germany) using high-precision cover glasses (Paul Marienfeld, Lauda-Königshofen, Germany). The filtration slit density (FSD) was evaluated according to podocyte exact morphology measurement procedure (PEMP) using 3D-SIM (Siegerist et al. 2017; Unnersjö-Jess et al. 2022). N-SIM super-resolution microscope (Nikon, Tokyo, Japan) equipped with a 100× silicone objective was used to get z-stacks of 19 planes with 488 and 561 nm channels acquired from the stained whole-kidney sections. The z-stacks were converted into a maximum intensity projection followed by the automatized identification of the filtration slit length. The z-stacks were transformed into a maximum intensity projection, and the filtration slit length was identified automatically as an index of foot process effacement. FSD was expressed as the ratio of filtration slit diaphragm per podocyte foot process areas; 20 glomeruli per animal evaluated in at least 3 rats per group.

2.2.8 TUNEL assay

Dewaxed rat kidney paraffin sections (4 μm) were refixed using 4% paraformaldehyde (PFA) and subjected to terminal deoxynucleotidyl transferase dUTP-mediated nick end labeling (TUNEL; Abcam, Ab66108) following manufacturer's instructions to detect DNA fragmentation and cell death. Nuclei were stained with DAPI. Apoptotic signals were evaluated using fluorescence microscopy at 200× magnification with DIC overlay. Signals were counted in randomly selected proximal tubular profiles of >10 adjacent optical fields per animal from at least 15 randomly chosen glomeruli per kidney and animal. The apoptosis rate was determined by calculating the ratio of TUNEL-positive nuclei to the total number of nuclei counted per field. Each experiment utilized a minimum of 4 rats per group. Image analysis was performed using ImageJ.

2.2.9 Electron microscopy

Perfusion-fixed kidney samples were post-fixed in a mixture of 1.5% glutaraldehyde, picric acid, and 0.1 M cacodylate buffer. Samples were further post-fixed with 1% osmium tetroxide (OsO_4), dehydrated, and either embedded in EPON for TEM or subjected to critical-point drying for SEM. Large-scale scanning TEM (STEM), was applied on Epon-embedded material. Semi-thin sections (1 μm) were obtained from Epon blocks using an ultramicrotome (Ultracut E, Reichert-Jung) and stained with Richardson's stain for LM evaluation to identify specific regions for further analysis. To examine pathological structures at the ultrastructural level, conventional or large-scale ultrathin sections (200 to 400 nm) were prepared (Dittmayer et al. 2021). Large-scale sections were digitized at a pixel size of 3 to 4 nm using TrakEM2 for stitching and nip2 for export to high-resolution TIFF files, which were then analyzed using QuPath. Qualitative and quantitative evaluations were conducted using a Gemini 300 field emission scanning electron microscope (FESEM, Zeiss) equipped with a STEM detector, SmartSEM, and Atlas 5 software, or a Zeiss EM901. Implementation on

www.nanotomy.org repository was done to allow open access for pan-and-zoom analysis; to this end, data sets were exported in a tiled browser-based file format using Atlas 5 software. For conventional 3D-SEM, dried and sputter-coated samples were evaluated using FESEM with a SEM detector.

2.2.10 Western Blotting

Whole rat kidney tissue was frozen in liquid nitrogen and then crushed into powder. The resulting powder was mixed with homogenization buffer containing 250 mM sucrose, 10 mM triethanolamine (AppliChem, PanReac, ITW Reagents) and protease inhibitor cocktail (cOmplete, Roche). The mixture was subjected to sonication (4 times for 1 second each, Sonoplus GM70, BANDELIN electronic GmbH, Germany) and centrifuged at 1000 × g for 10 min at 4 °C to obtain the supernatant containing the protein lysate. The protein concentration was determined using a Micro BCA protein assay kit (Micro BCA Protein Assay Kit, Fisher Scientific GmbH, Germany). The lysate was stored at -80 °C until further analysis. To prepare the samples for analysis, they were mixed with buffer (2% SDS, 10% glycerol, 5% ß-mercaptoethanol, 1% bromphenol blue, 95 mM Tris, pH 6.8) and heated for 10 min at 65 °C. Protein separation was accomplished using a sodium dodecylsulfate polyacrylamide gel electrophoresis (SDS-PAGE) using an electrophoresis chamber (Bio-Rad Laboratories GmbH, München, Germany) filled with running buffer (0.1% SDS, 192 mM glycin, 25 mM Tris, pH 8.3). Eight to 10% polyacrylamide gels were filled with 30 to 40 µg protein per lane, run, then blotted onto polyvinylidene difluoride membrane (PVDF, Macherey-Nagel GmbH & Co. KG, Germany). The membrane was then blocked with 5% milk or BSA/TBS and exposed to primary antibody overnight at 4 °C with rotation. Secondary antibody conjugated with HRP was then applied and the signal detected using chemiluminescent reagent (Amersham ECL Western blotting detection reagent, GE

Healthcare). Blots were captured using an Intas ECL ChemoCam Imager (Intas Science Imaging Instruments GmbH) and the protein bands quantified using ImageJ.

2.2.11 RNA extraction and qualification

Total RNA from kidneys was extracted using PeqGOLD TriFast (VWR Life SCIENCE) following the guidelines provided by the manufacturer. The purity of the RNA was assessed using a NanoPhotometer R spectrophotometer (IMPLEN). To determine the quantity and integrity of the RNA, an RNA Nano 6000 Assay Kit and Bioanalyzer 2100 system (Agilent Technologies) was employed.

2.2.12 RNA sequencing and data processing

RNA-sequencing (RNA-Seq) was conducted on RNA samples obtained from rat kidneys with a sample size of 4 to 6 per group. RNA samples (each 1 µg) were used to generate sequencing libraries with NEBNext RNA Library Prep Kit for Illumina (New England BioLabs). Index codes were added to identify each sample during sequencing. Clustering of the index-coded samples was performed using the cBot Cluster Generation System with the PE Cluster Kit cBot-HS (Illumina). Libraries were then sequenced on the Novaseq HisEquation 4000 platform (Illumina), generating paired-end reads of 150 bp. Differential expression analysis between two groups was carried out using the DESeq2 R package specifically designed for analyzing digital gene expression data. Resulting P-values were adjusted using the Benjamini and Hochberg method to control the False Discovery Rate (FDR). Genes with an adjusted P-value < 0.1 (without logFC cutoff) as determined by DESeq2 were considered differentially expressed genes. The RNA-Seq data were deposited in the Gene Expression Omnibus repository maintained by the National Center for Biotechnology Information (NCBI) with the accession number GSE225215.

2.2.13 Proteomics

Protein lysates from rat kidneys with a sample size of 4 to 6 per group were subjected to global proteomics analysis using established methodology at Charité Core Facility for High Throughput Mass Spectrometry, Berlin. Twenty-five µL of a benzonase (Sigma-Aldrich, solution containing 50 units enuyme), 50 mM ABC (Roth), and 2 mM MgCl were added to a protein lysate of 100 µg in 25 µL volume. The mixture was then incubated for 30 min at 37 °C with shaking. Next, the lysates were processed using the SP3 protocol on a Biomek i7 workstation, following an established method with a single-step reduction and alkylation (Müller et al. 2020). In brief, 16.6 µL of a reduction and alkylation buffer containing 40 mM TCEP (Sigma-Aldrich), 160 mM CAA (Merck/Millipore), and 200 mM ABC was added to the sample, which was then incubated at 95 °C for 5 minutes. To bind the proteins, a combination of hydrophilic and hydrophobic paramagnetic beads (in a 1:1 ratio) was employed, leading to protein precipitation with 50% ACN (Fisher Scinetific). The samples were subjected to two washes with ethanol and one wash with ACN. Following this, the proteins were reconstituted in 35 µL 100 mM ABC and digested in 20 µL trypsin (Promega) at 37 °C for 17 h. The reaction was halted by adding formic acid at a final concentration of 0.1%. The resulting tryptic peptides were analyzed by LC-MS/MS using a timsTOF Pro 2 mass spectrometer (Bruker). Peptide mixtures were separated using an Ultimate 3000 RSLCnano instrument (Thermo Fisher Scientific) equipped with a two-linear-column system. The digested samples were concentrated on a trapping guard column (PepMap C18, 5 mm × 300 m × 5 m, 100; Thermo Fisher Scientific) and subsequently eluted from an analytical nanoLC column (75 m inner diameter 500 mm nano Acclaim PepMap C18, 2 m, 100; Thermo Fisher Scientific). The separation was achieved by utilizing a mobile phase consisting of 0.1% formic acid (Buffer A) and 80% acetonitrile with 0.1% formic acid (Buffer B). A linear gradient was applied over 120 minutes, with

Buffer B increasing from 7.5% to 25% within 82.5 minutes, followed by a further increase to 40% within 30 minutes, at a flow rate of 300 nL/min. Q Exactive instrument was employed in data-independent mode with the settings, Orbitrap configured to acquire 40 DIA spectra with a precursor isolation window of 12 m/z (covering 500-1000 m/z). The DIA spectra were collected with a resolution of 17.500, an AGC target of 1e6, and a maximum inject time of 60 ms, utilizing an overlapping window pattern. Precursor MS spectra (m/z 494-1006) were interspersed with the DIA spectra, collected at a resolution of 35.000 after accumulating ions for 60 ms to reach a target value of 1e6 in profile mode. The mass spectrometric conditions were set, spray voltage set at 2.1 kV, no sheath or auxiliary gas flow. The heated capillary temperature was maintained at 275 °C, and the normalized HCD collision energy was set to 27%. Additionally, lock masses at m/z 391.28430 and 445.1200 were used to account for background ions. The raw data were processed using DIA-NN 1.8 with standard settings, employing MS1 and MS2 resolution of 10 ppm. Peptides were identified without relying on a predefined library, using the *Rattus norvegicus* UniProt sequence database (UP000002494_10116) downloaded on January 16, 2021, and the matched-between-runs (MBR) option. The output was filtered at a false discovery rate (FDR) of 0.01 at the peptide level. Subsequent analyses were performed using the R package DEP. Proteins with an adjusted *P*-value below 0.1 (without a logFC cutoff) were considered differentially expressed. The data have been deposited in the ProteomeXchange Consortium through the PRIDE partner repository, and the accession number is PXD038841.

2.2.14 Phosphoproteomics

Global phosphoproteomic analyses were perfomed according to adapted protocols from own previous work (Mertins et al. 2016). Cryo-pulverized tissue (n=4 to 5 per group) was lysed in SDC lysis buffer containing, 150 mM NaCl, 50 mM Tris-HCl pH 8,

1 mM EDTA, 10 mM DTT, 40mM CAA (2-chloroacetamide and phosphatase inhibitor cocktail II and III [Sigma Aldrich]). The lysates were heated at 95 °C for 10 minutes and then cooled to room temperature. Benzonase (Merck) was added and the samples were incubated at 37 °C for 30 minutes. Protein digests were performed using endopeptidase LysC (Wako) and trypsin (Promega) overnight at 37 °C with an enzyme-to-protein ratio of 1:100. The resulting peptides were desalted, dried, and dissolved in 50 mM HEPES. TMT labeling was performed according to the manufacturer's instructions, using TMT10 or TMTpro reagents (Thermo Fisher Scinetific). TMT channel assignment was randomized among the biological replicates. Samples within each TMT plex were pooled, cleaned up using tC18 Sep-Pak cartridges (Waters,100mg/1cc), and fractionated into 30 fractions using high-pH reversed-phase chromatography. For global proteome analysis, 10% of each fraction was used, while the remaining 90% was pooled into 15 fractions for phosphopeptide enrichment. The enrichment was carried out using Fe(III)-IMAC cartridges and the AssayMAP Bravo Platform (Agilent Technologies). Peptides were eluted in 1% ammonia, acidified, and dried down. To perform LC-MS/MS measurements, peptides were dissolved in a solution containing 3% acetonitrile with 0.1% formic acid. The separation of peptides was achieved using a reversed-phase column measuring 20 cm in length and with an inner diameter of 75 μm. The column was packed with C18-AQ 1.9 μm resin (Dr. Maisch GmbH). A high-performance liquid chromatography (HPLC) system (Thermo Fisher Scientific) was used for this purpose. The separation was carried out with a flow rate of 250 nL/min and a gradient over 98 minutes, gradually increasing the concentration of acetonitrile. The sample measurements were performed on a Q-Exactive HF-X instrument (Thermo Fisher Scientific). The instrument operated in data-dependent acquisition mode, employing specific settings. Full-scan acquisition was performed with an Automatic Gain Control (AGC) target of 3×10^6 at a resolution of

60K, scanning a range of 350-1500 m/z, and with a maximum injection time of 10 ms. For MS2 scans, the AGC target was set to 1 x 10^5 at a resolution of 45K, and the maximum injection time was 86 ms for non-enriched peptides and 100 ms for phosphopeptides. The precursor charge state ranged from 2 to 8, and the instrument conducted the top 20 MS2 scans per full scan. The normalized collision energy was set to 33 for TMT10 plex samples and 30 for TMTpro plex samples. Peptide samples were reconstituted and separated on a reversed-phase column using a gradient flow of increasing acetonitrile concentration. The separation was performed on an HPLC system. LC-MS/MS measurements were conducted using a Q-Exactive HF-X instrument in data-dependent acquisition mode. Full-scan and MS2 scans were acquired at specified resolutions and injection times. Different settings were used for enriched and non-enriched peptides, including normalized collision energy values. The RAW data were analyzed using the MaxQuant software package. The Andromeda search engine was employed to search MS2 spectra against a decoy rat UniProt database. Various modifications and parameters were set for the search, including variable and fixed modifications, peptide length, missed cleavages, and FDR thresholds. Quantification was performed using reporter ion MS2 and specific correction factors. Statistical analysis was conducted using the Perseus software, involving log2 transformation, filtering, and normalization of reporter ion intensities. Differential protein or phosphosite abundance was determined using Student's *t*-test with FDR-based cutoff of 5%. The data presented in the study are deposited in the ProteomeXchange Consortium via the PRIDE partner repository, accession number (PXD038546).

2.2.15 Gene ontology and pathway analyses

The analysis of Gene Ontology (GO) and pathways for the genes, proteins, and phosphoproteins that exhibited differential expression was conducted using the web-

based bioinformatics tool Enrichr available at https://maayanlab.cloud/Enrichr/. Pathways that demonstrated a significance level of $P < 0.05$ were considered as significantly regulated.

2.2.16 Statistical analysis of experimental data

The analysis of the results was carried out in a blinded manner, subjecting data to routine parametric statistical methods, assuming a normal distribution based on the experimental design. A comparison between two groups was performed using an unpaired t-test, while a comparative evaluation of multiple groups was conducted using ANOVA followed by Tukey's post-hoc tests. GraphPad Prism8 software was utilized for the analysis of the parameters. A significance level of $P < 0.05$ was considered statistically significant.

3. Results

3.1 Renal function

Renal function was evaluated by determining creatinine clearance, blood urea nitrogen (BUN), and FENa after CNI administration. Both CsA and Tac caused similar decreases in creatinine clearance (−27% and −14%, respectively) and FENa (−40% and −39%, respectively). In contrast, BUN was significantly elevated after CsA and Tac administration (18% and 30%, respectively), reflecting kidney dysfunction (Figure 8).
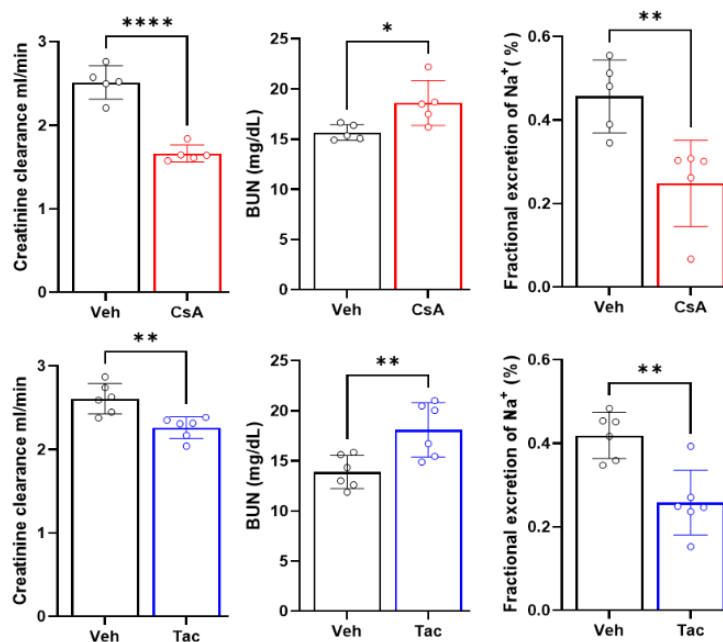
Figure 8. Physiologic parameters. Values for creatinine clearance, blood urea nitrogen (BUN), and fractional sodium excretion after 4 weeks of vehicle (Veh), cyclosporine A (CsA), or tacrolimus (Tac) treatment. Mean values from n= 5 to 6 rats ± SD, *$P < 0.05$, **$P < 0.01$, ****$P < 0.0001$.

3.2 Renal histology

The rats in the Veh-treated group were normal with respect to kidney structure and gene expression according to generally accepted criteria. In contrast, rats in the CNI-treated groups showed significant histopathological kidney abnormalities. As expected, the alterations varied from moderate onset stages to nephron damage. We

41

examined the CNI-induced changes in collagen expression by staining sections with Sirius Red. Areas with positive staining in the renal interstitium progressively increased to day 28 upon CNI compared to vehicle. These fibrous foci, which typically comprised 5 to 20 tubular profiles, were common in the subcapsular cortex and extended to deeper regions of the cortex and outer medulla, where they displayed typical patterns of striped fibrosis (Figure 9).
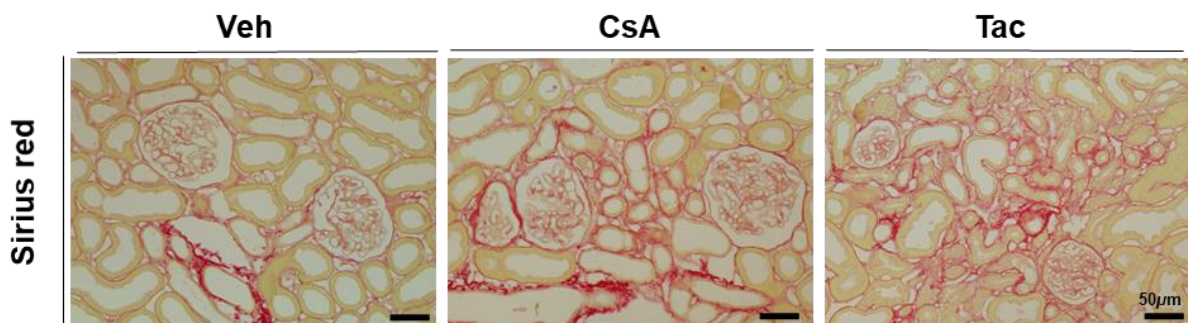

Figure 9. Kidney histopathology. Sirius red staining illustrating collagen deposits in representative views from vehicle (Veh), cyclosporine A (CsA), and tacrolimus (Tac) samples; note focal areas of tubular degeneration. Bars indicate magnification.

The impact of CNI on interstitial fibroblast conversion to myofibroblasts was studied by their expression of α-SMA. A substantial immunoreactive signal for α-SMA revealed intense profibrotic myofibroblast transdifferentiation and pericyte activation. Immunohistochemical labeling revealed more α-SMA-positive cells in the interstitium of CsA- and Tac-treated animals than Veh-treated animals. The α-SMA signal in CNI was particularly evident near atrophic or necrotic tubules and nearby glomeruli. These showed pericapsular α-SMA signal to varying degrees, with stronger signals in the CsA-treated group (9.55% per unit area) than in the Tac-treated group (8.24% per unit area; Figure 10A-D). CD45 staining was used to quantify the level of infiltrating cells. Anti-CD45 immunofluorescence staining of the corresponding CNI kidney section showed significant infiltration of leukocytes into the interstitium (Figure 10E-H).
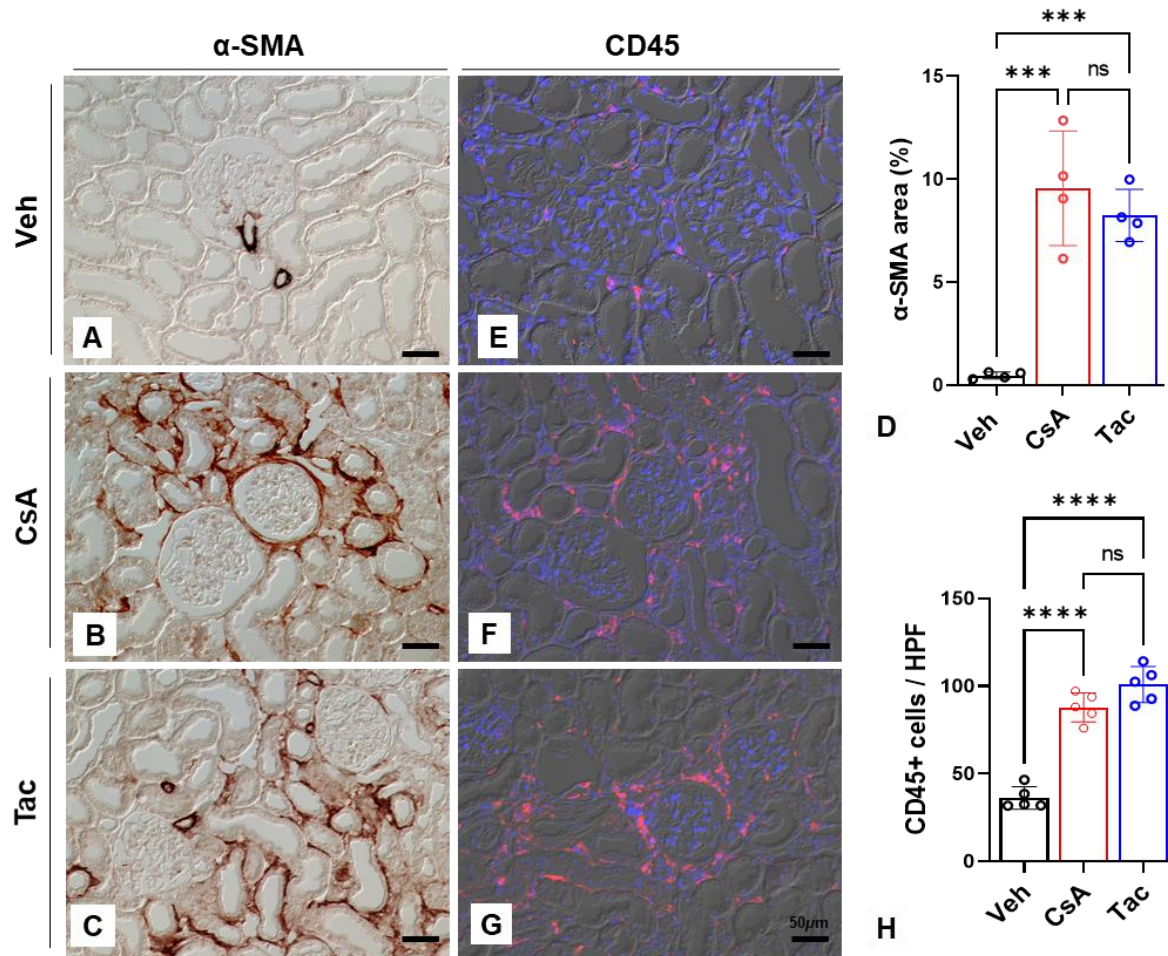
Figure 10. Smooth muscle actin (α-SMA) and leukocyte common antigen (CD45) staining. (A-D) Immunoperoxidase staining for anti-α-SMA in the vehicle (Veh) group (A) reveals signals within the vascular walls. In the cyclosporine A (CsA) and tacrolimus (Tac) groups, there is an increase in interstitial signals localized around tubules and glomeruli (B, C). Bar graphs represent the average size of α-SMA-stained cortical foci as a percentage of the unit sectional area (D); data represents the mean ± SD; *** P < 0.001; ns, not significant. (E-H) Immunofluorescence staining for CD45 demonstrates scattered interstitial cells in the cortex of the vehicle group (E), while CsA and Tac samples display clusters of interstitial signals within fibrotic regions (F, G). Bar graphs represent the average number of CD45 stained cells per unit sectional area. Data represents the mean ± SD; *** P < 0.001; ns, not significant. (H). Images were captured using DIC optics. Bars indicate magnification.

Ultrastructurally, arteriolar myocytes in the CsA-treated group were notably rich in the contractile apparatus of single-layered media, while those in the Tac-treated group were thin and layered (Figure 11A-C). The lumen-to-wall ratio was quantitatively assessed in the cross-sectional images. Media and endothelium of glomerular afferent arterioles were thickened in the CNI-treated groups. Endothelial cell expression of CD31 was slightly higher in the CsA- and Tac-treated groups (Figure 11D-G).
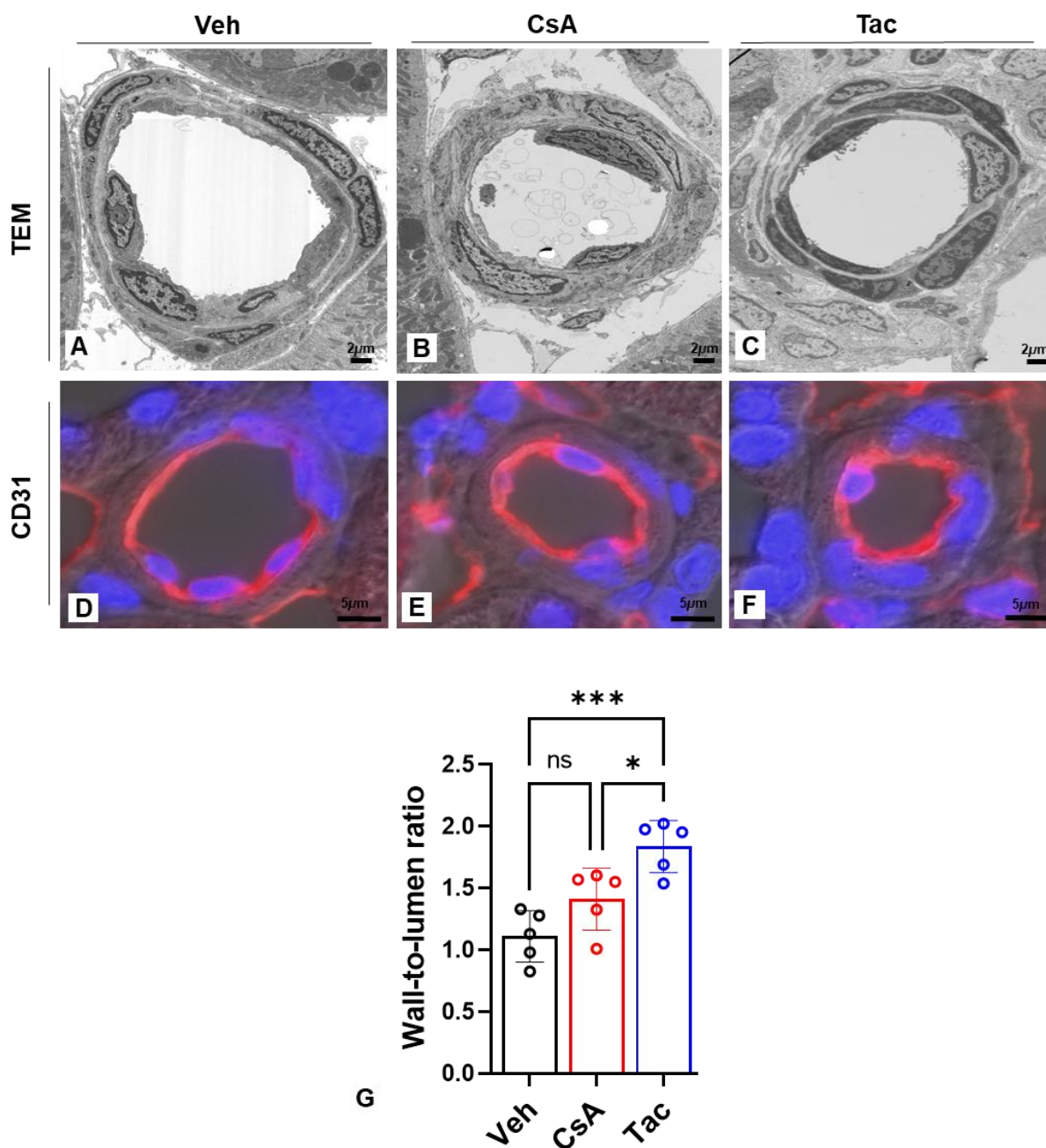
43

Figure 11. Arteriolar wall structure. (A-C) Transmission electron microscopy (TEM) images reveal distinct wall structures in the vehicle group (Veh) with regular architecture (A), increased myocyte contractile fibers in the cyclosporine A (CsA) group (B), and thinned but layered media cells in the tacrolimus (Tac) group along with increased interstitial matrix (C). Immunofluorescence staining of endothelial CD31 shows increased CD31 signal in the CsA and Tac groups. Blue nuclear staining, DAPI; DIC optics were used to capture structure (D-F). Bar graphs represent the wall-to-lumen ratio. Data represents the mean ± SD; * $P < 0.05$, *** $P < 0.001$; ns, not significant (G). Bars indicate magnification.

Renin expression in renal juxtaglomerular cells was examined using immunohistochemistry to determine RAS activation following CNI administration.

Immunoreactive renin was observed in normal juxtaglomerular position in the Veh group. In contrast, immunoreactive renin was observed along the terminal afferent arterioles upstream of the glomerulus in the CNI-treated groups. Renin quantification showed that the total renin-positive area of the kidney was 7-fold larger in the CsA-treated group and 8.8-fold larger in the Tac-treated group compared to the Veh-treated group (Figure 12A-D).
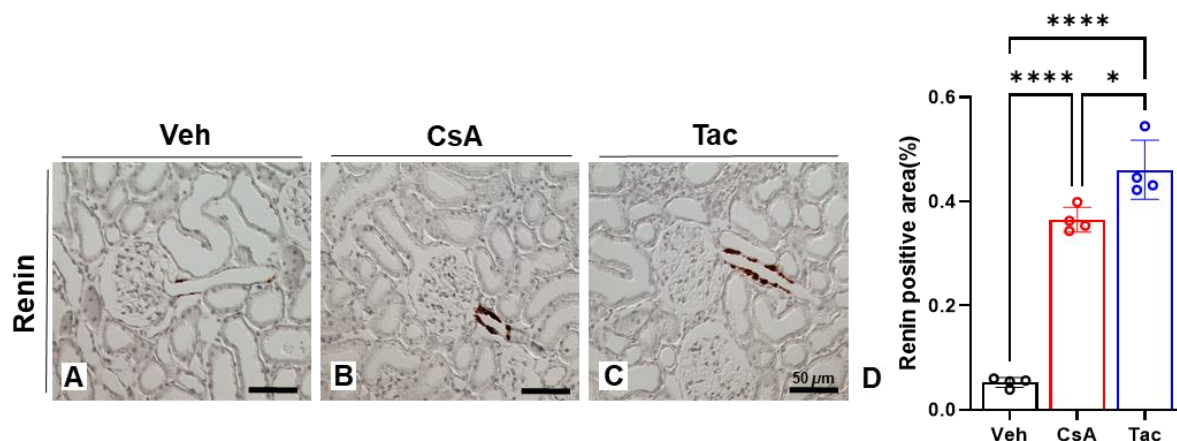

Figure 12. Juxtaglomerular apparatus - renin. (A-D) Immunoperoxidase staining with anti-renin antibody demonstrates normal distribution of renin signal in the preglomerular afferent arteriolar portion in the vehicle (Veh) group (A). In the cyclosporine A (CsA) group, there is a significant increase in renin signal (B), which is further elevated in the tacrolimus (Tac) group (C) as shown in representative views. Bar graphs illustrate the quantitative expression of renin, represented as the immunoreactive area in percent of unit sectional area. Data represents the mean ± SD; * $P < 0.05$, **** $P < 0.0001$; ns, not significant. Bars indicate magnification.

Glomeruli of Veh-treated rats appeared normal. While glomerular structure of the CNI-treated rats appeared identical to those of the Veh-treated rats, moderate sclerosis and/or retraction were observed near or within fibrotic foci. The glomerular tuft volume was analyzed using co-staining for podocin and integrin α3. The glomerular tuft area decreased by 18% in the CsA-treated group and 14% in the Tac-treated group. Glomerular capillaries were narrowed, and mesangial matrix expansion was observed in the CNI-treated groups compared to the vehicle-treated group (Figure 13A-D). In SEM, the glomeruli appeared normal, and most glomerular capillaries seemed adequately perfused in the Veh-treated group. Podocytes appeared normal with the

typical interdigitating pattern of foot processes. In contrast, CsA-treated rats frequently showed moderate foot process effacement, whereas Tac-treated rats showed more extensive and generalized effacement with substantial podocyte degeneration (Figure 13E-K).
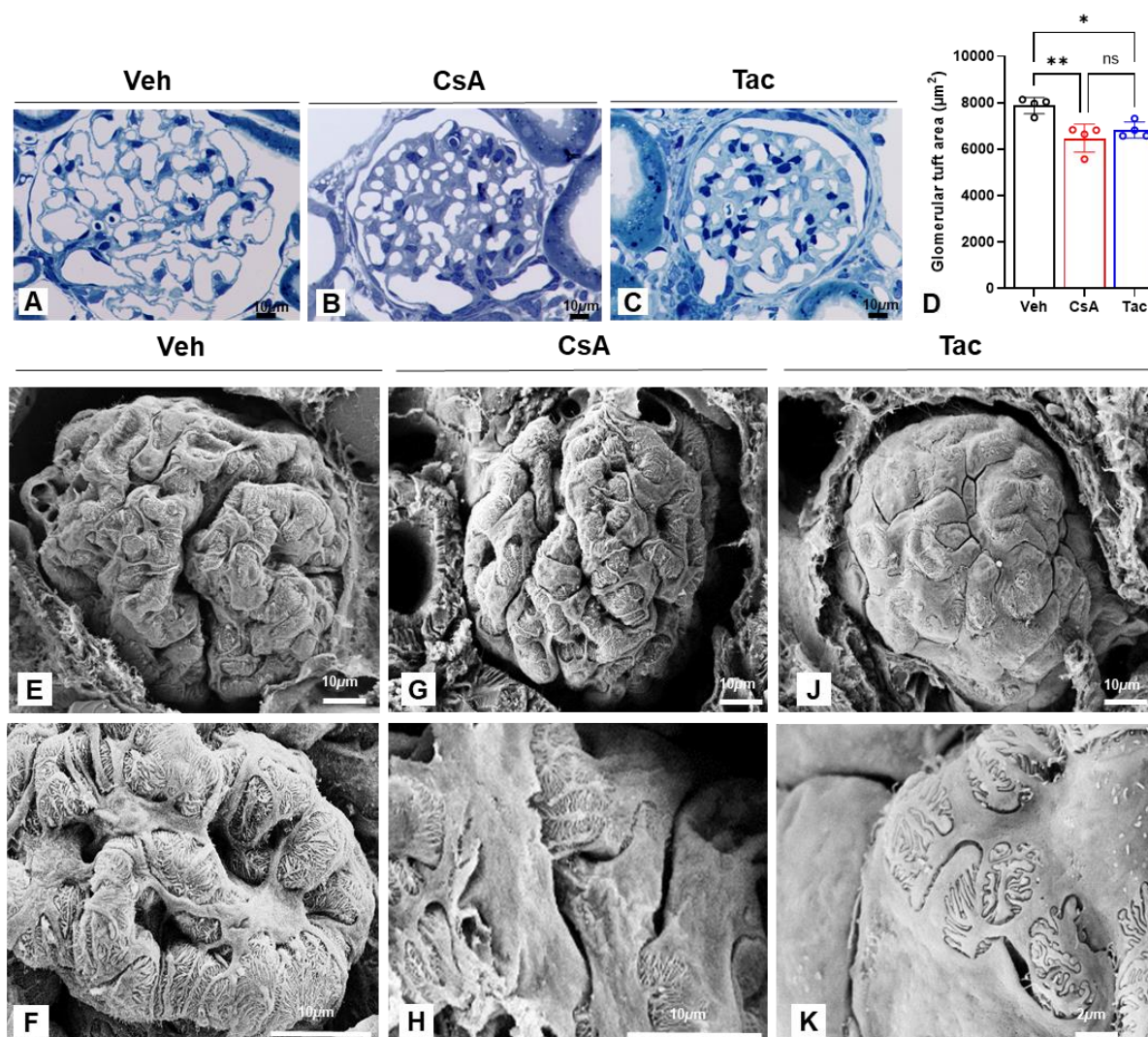

Figure 13. Glomerular structure. (A-D) Semithin sections stained with Richardson's blue stain reveal the intact structure of glomeruli in representative views from the vehicle (Veh) group (A). In the cyclosporine A (CsA) group, sclerotic glomeruli at the onset stage are frequently observed (B), and a similar pattern is seen in the tacrolimus (Tac) group (C). These sclerotic glomeruli exhibit a characteristic retracted appearance, with flattened podocytes and reduced width of capillary lumina. (D) A bar diagram demonstrates significant decreases in glomerular tuft size, quantified from podocin-immunostained sections. Data represents the mean ± SD; * $P < 0.05$, ** $P < 0.01$; ns, not significant. (E-F) In representative scanning electron microscope (SEM) views, the three-dimensional (3D) structure of the glomerular tuft is observed from the urinary space after the removal of Bowman's capsule. Veh samples had a regular morphology of the tuft with individual capillary loops covered by podocytes and their processes (E-F). In CsA samples, single capillaries display flattened podocytes with broadened cell bodies, as well

46

as retracted or fused processes indicating effacement (G-H). In Tac samples, effacement is more advanced, with overall flattened podocytes covering the capillaries using their extended cell bodies (J). A closer look reveals podocyte effacement with marked retraction of foot processes (K). Bars indicate magnification.

Bowman´s capsule showed some abnormalities in TEM, including an activated, thickened parietal epithelium with irregular vacuolization, basement membrane layering, and nearby hyaline inclusions in CNI (Figure 14A-B). Multiple synechiae with podocytes were frequently observed in CsA-treated (Figure 14C-E) and Tac-treated (Figure 14F) rats.
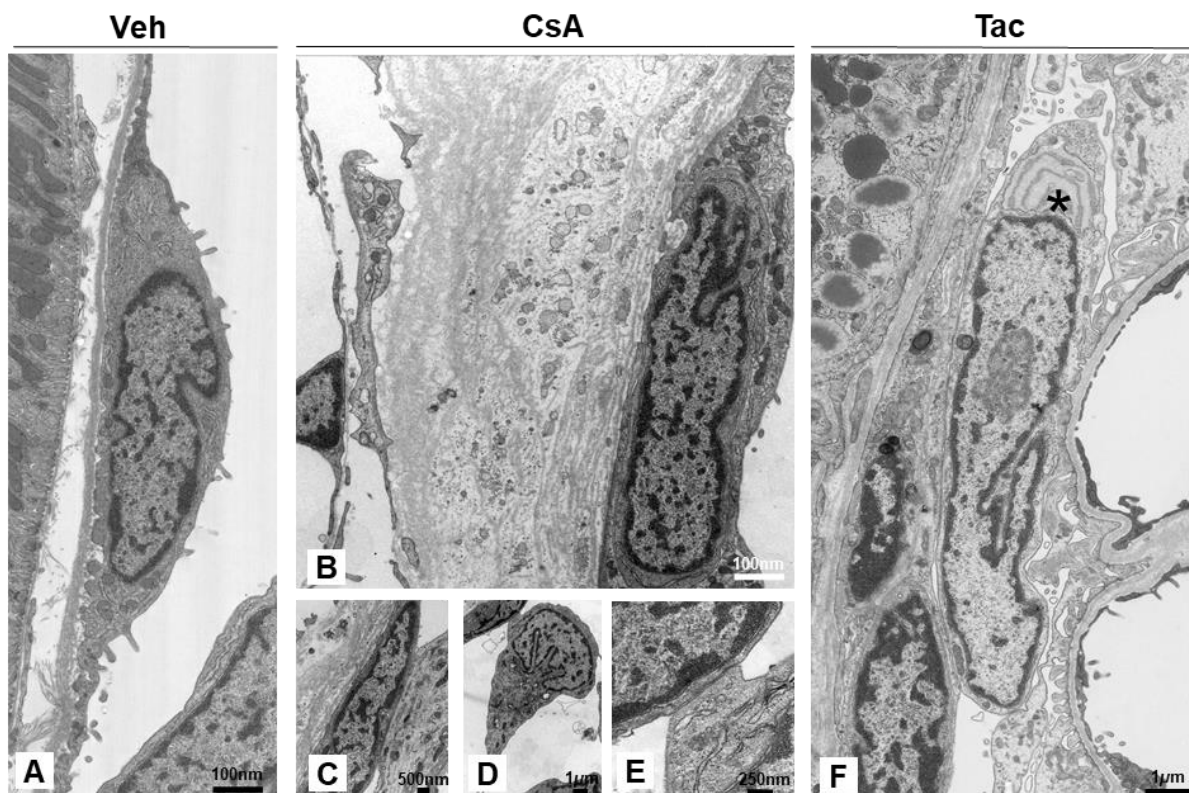
Figure 14. Changes in Bowman's capsule. (A-F) Transmission electron microscopy (TEM) representative images reveal the regular structure of Bowman's capsule in the vehicle (Veh) group (A), characterized by a flat parietal epithelium and a thin capsular basement membrane. (B) In the cyclosporine A (CsA) group, both the parietal epithelium and the capsular basement membrane show significant thickening, accompanied by the formation of extensive granular and hyaline matrix. (C) Synechiae with multiple contact points are formed in CsA, indicating adhesions between different structures. (D, E) Podocytes may also form synechiae, even in the urinary pole area, where they are prone to undergoing "tip lesions". (F) In Tac samples, a similar synechia between podocytes and the parietal epithelium is shown, along with the presence of a characteristic inclusion body within the podocyte's rough endoplasmic reticulum (rER). Bars indicate magnification.

Expression of CD44 was investigated in the kidneys of the vehicle and CNI groups. While in control rats immunofluorescence labeling revealed a few CD44-positive cells in the interstitium, the glomeruli showed almost no signals. In rats treated with CNI, the parietal epithelial cells lining Bowman's capsule showed enhanced CD44 expression compared to vehicle. In glomerular tuft, tubules, and interstitium cell numbers were higher, and so was intensity of staining (Figure 15 A-C). Anti-CD45 antibody was used to identify leukocyte infiltration. CD45-positive leukocytes in glomeruli differed dramatically between CNI groups with mild pericapsular signal in CsA and substantially higher signal in Tac (Figure 15 D-F).
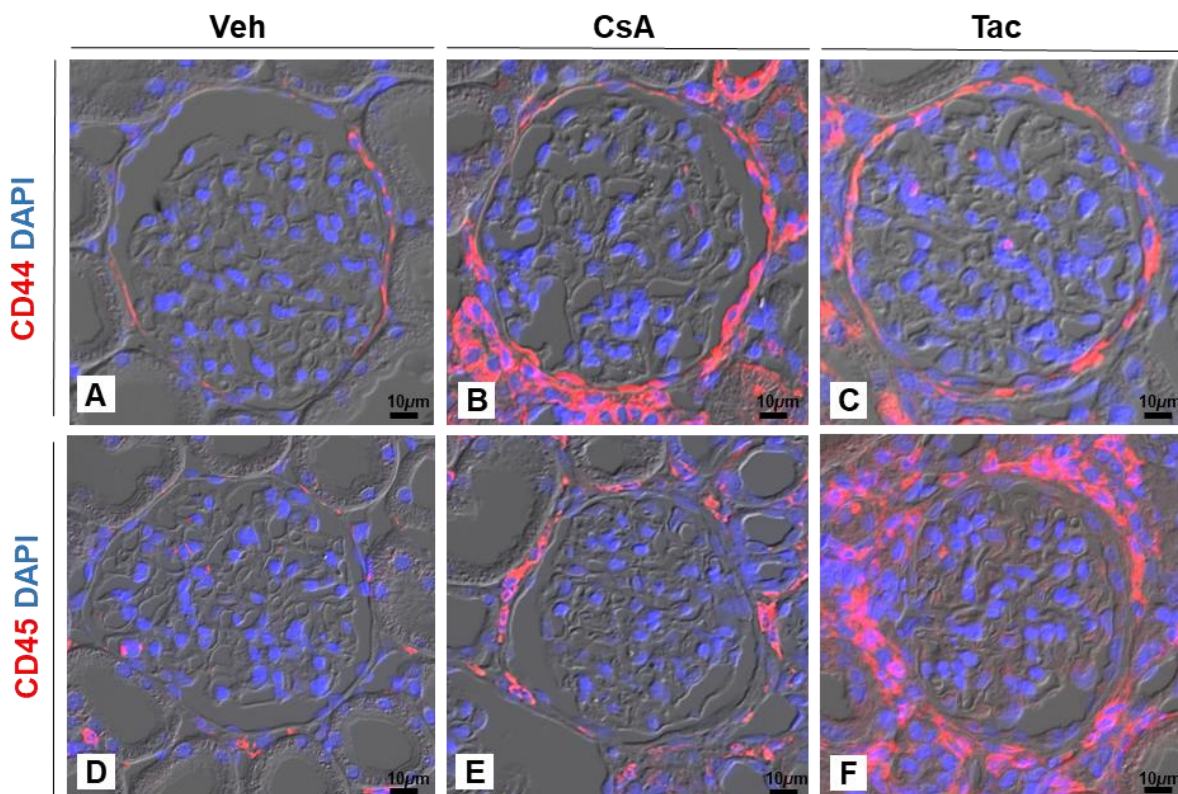
Figure 15. Glomerular CD44 and CD45 expression. (A-F) Immunofluorescence staining for anti-CD44 reveals sporadic and mild signals in Bowman's capsule of the vehicle (Veh) sample (A) whereas in cyclosporine A (CsA) and tacrolimus (Tac) samples, the activated parietal epithelium exhibits a high intensity signal along almost the entire perimeter (B, C). Conversely, anti-CD45 staining shows a few interstitial signals in the Veh sample (D), but a strong signal associated with the capsule in CsA (E), and even more so in Tac samples (F). Blue nuclear staining, DAPI, DIC optics were used to capture the structure. Bars indicate magnification.

Within the glomerular tuft, the degree of glomerular retraction and podocyte foot process effacement seemed to be characteristic for the histologic degenerative patterns observed in both CNI groups. Both further showed wrinkling of the GBM along the mesangial stalks. To observe foot-process morphology in detail, we used 3D-SIM and PEMP to evaluate podocyte filtration slit density as a marker for podocyte effacement. Anti-podocin staining was used as a marker of the slit diaphragm located between the foot processes. In addition, we stained for anti-integrin α3 to visualize the GBM. Within the glomeruli, some regions displayed an intact foot process architecture, while others showed foot process retraction and erratic arrangement or had entirely lost podocin staining, indicating complete effacement. TEM showed that focal effacement was significantly more severe in the Tac- than in the CsA-treated group (Figure 16A and B).
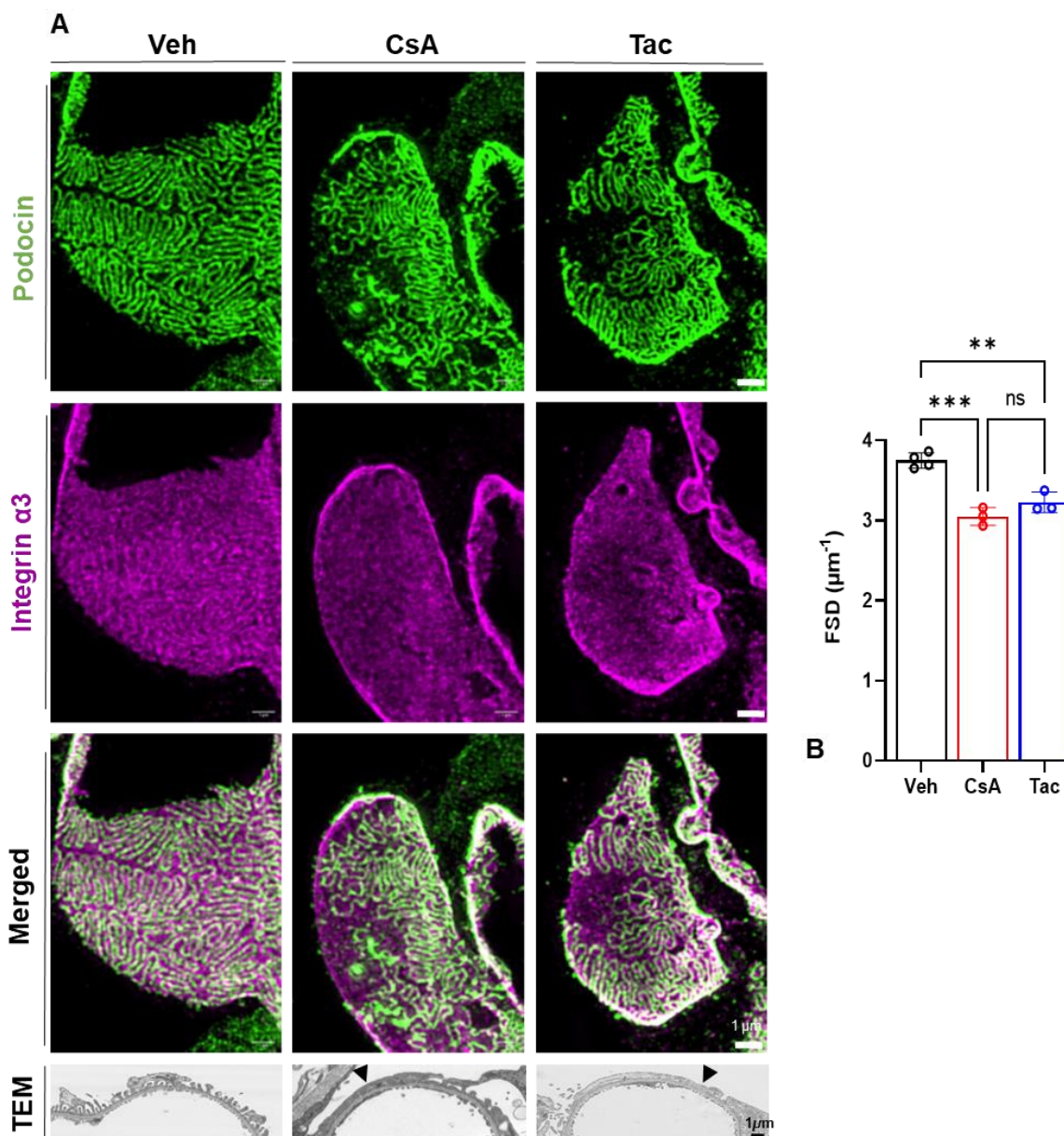
Figure 16. Glomerular capillaries – podocyte foot process effacement, changes in filtration slit density. (A) To assess the filtration slit density (FSD), a double-immunostaining technique was employed using anti-podocin antibody to label the filtration slit and anti-integrin α3 antibody to label the glomerular basement membrane (GBM). This evaluation was conducted using 3D-structured illumination microscopy (3D-SIM) and Podocyte Exact Morphology Measurement Procedure (PEMP). Optically, when examining flat sections of capillary loops at high magnification, a regular arrangement of filtration slits covering the GBM is observed in the vehicle (Veh). However, in cyclosporine A (CsA) and tacrolimus (Tac) samples, areas of effacement (indicated by white circles in the merged images) can be identified by the absence of slit diaphragms in regions that otherwise react positively for integrin α3, indicating the presence of the GBM. Representative transmission electron microscopy (TEM) images of the filtration barrier demonstrate the regular structure of podocyte foot processes in a Veh sample, while portions of the capillary perimeter typically exhibit flattened epithelium due to foot process effacement in the CsA and Tac samples (indicated by arrows). (B) A bar diagram illustrates a significant reduction in FSD in both the CsA and Tac groups compared to the Veh group. Data

represents mean ± SD; ** P <0.01, *** P < 0.001; ns, not significant. Bars indicate the magnification.

SEM showed normal endothelial fenestration on the endothelial side of the glomerular capillary lumen in the vehicle-treated group. However, in the CNI-treated groups fenestral pore density was decreased, again markedly more in the Tac- than in the CsA-treated group (Figure 17A-D). These alterations were confirmed by TEM and associated with significant endothelial cell condensation primarily in the Tac-treated group. Regions of decreased pore density were often adjacent to regions of podocyte effacement (Figure 17E-K). Significant reductions in pore density were quantitatively confirmed (Figure 17L).
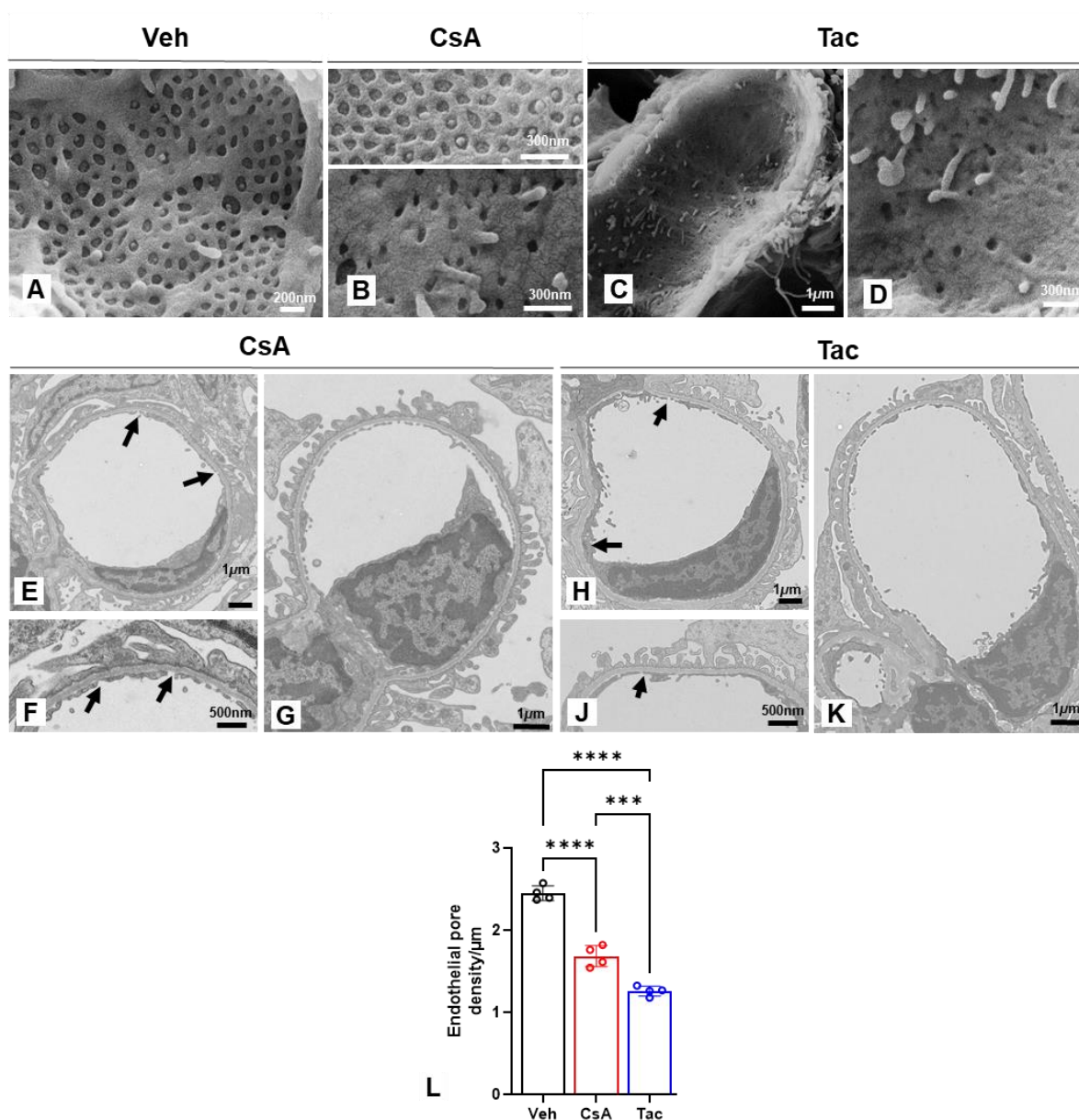
Figure 17. Glomerular capillaries - endothelial pore density. (A-D) Representative scanning electron microscopy (SEM) images depict the structure of glomerular capillary endothelium. Vehicle (Veh) group demonstrates normal endothelial fenestration with a regular pore density (A). In the cyclosporine A (CsA) group, both normal (top) and reduced pore density can be observed (B). In the tacrolimus (Tac) group, there is a substantial reduction in pore density (C) and smaller pore size compared to the samples treated with calcineurin inhibitors (CNI) (D). (E-G) Transmission electron microscopy (TEM) images show the characteristic structure of capillary endothelium in CsA. Capillaries with obvious pore losses (between arrows) can be detected (E, F), as well as capillaries without apparent pore losses (G). It is noteworthy that the endothelial morphology is otherwise similar in images (E) and (G), indicating the presence or absence of pore losses. (H-K) In Tac samples, capillaries with noticeable pore losses (between arrows) and capillaries without apparent pore losses can also be observed. However, when displaying pore losses, the endothelium exhibits striking condensation and darkening (H). The bars in the images indicate the magnification level. (L) A bar diagram presents a significant decrease in pore density per µm of glomerular basement membrane (GBM), as

quantified from TEM sections. Data represents the mean ± SD; *** $P < 0.001$, **** $P < 0.0001$; ns, not significant. Bars indicate magnification.

TUNEL immunofluorescence of the tuft showed significant nuclear signal increases in the Tac-treated group but less so in the CsA-treated group. In contrast, parietal epithelial cells showed a higher signal in the CsA- than in the Tac-treated group (Figure 18A-C). WT-1 labeling was used to determine glomerular podocyte expression strength. WT-1 positive podocyte numbers were significantly lower in the Tac-treated group than in the CsA- and vehicle-treated groups (Figure 18D-F). TUNEL labeling was inversely related to the number of WT-1-positive cells in glomeruli in the Tac-treated group. The quantification of numbers support these observations (Figure 18G-J).
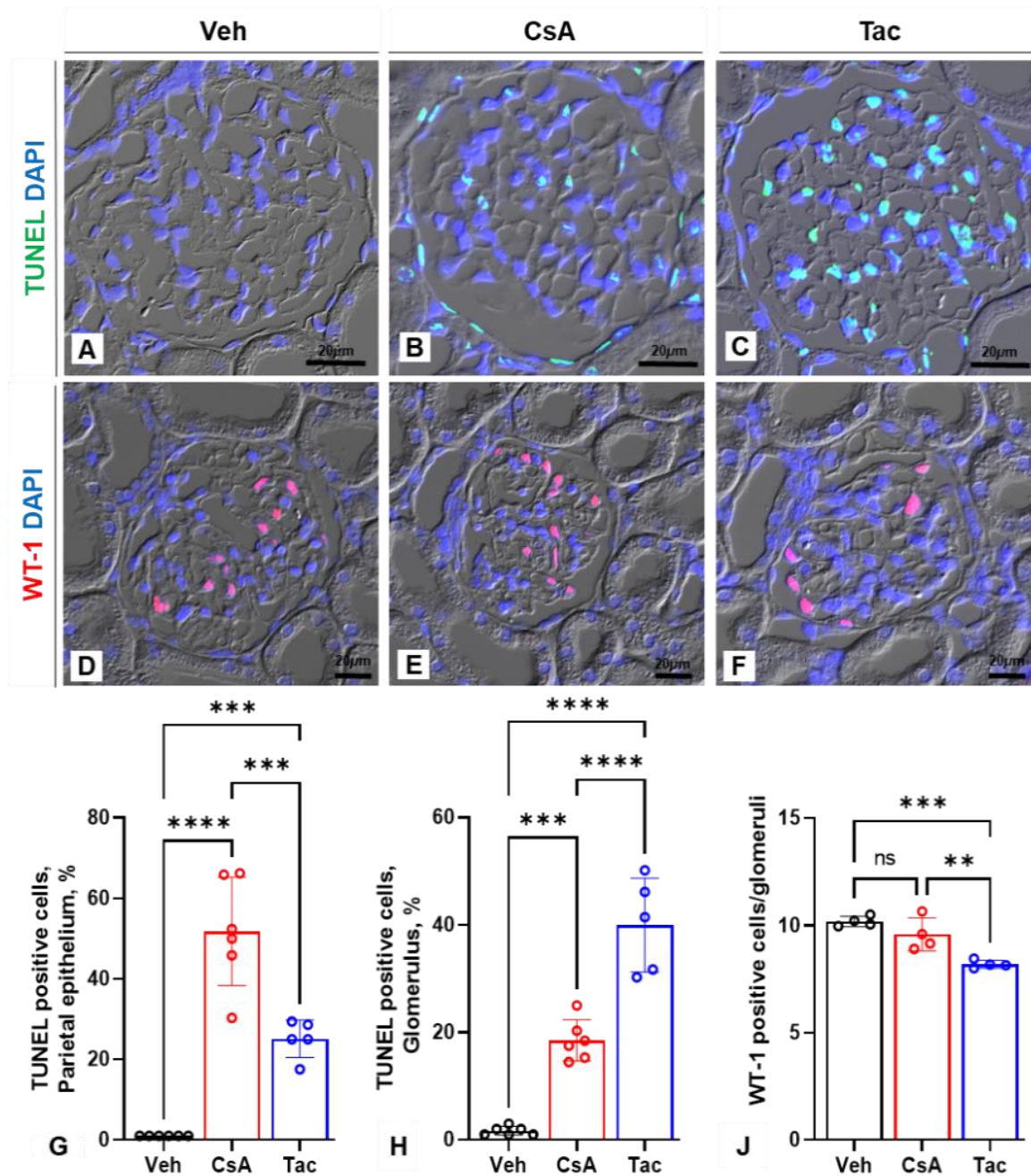
Figure 18. Glomerular TUNEL labeling and WT-1 expression. TUNEL immunofluorescence staining reveals a green nuclear signal. No signal is detected in the vehicle (Veh) group (A), but a significant signal is observed in the glomerular tuft and parietal epithelium of rats treated with cyclosporine A (CsA) (B). In tacrolimus (Tac) samples, numerous signals are particularly observed within the glomerular tuft, although to a lesser extent in the parietal epithelium (C). Anti-WT1 antibody immunofluorescence staining labels podocyte nuclei in representative glomeruli from Veh, CsA, and Tac samples (D-F). In Tac samples, the number of positively stained podocyte number was significantly reduced. Data represents the mean ± SD; ** $P < 0.01$ *** $P < 0.001$, **** $P < 0.0001$; ns, not significant. Bars indicate the magnification.

TEM showed that apical vesicular compartments, endosomes, fields of dense apical

tubules (DATs), and autophagic vesicles with membraneous content, anastomosing

with budding DAT, regularly occurred in the PCTs of the vehicle-treated group (Figure 19), whereas these areas were typically dominated by the heterolysosomes in the CsA-treated group. Lysosomes showed a near-normal phenotype in Tac-treated group.
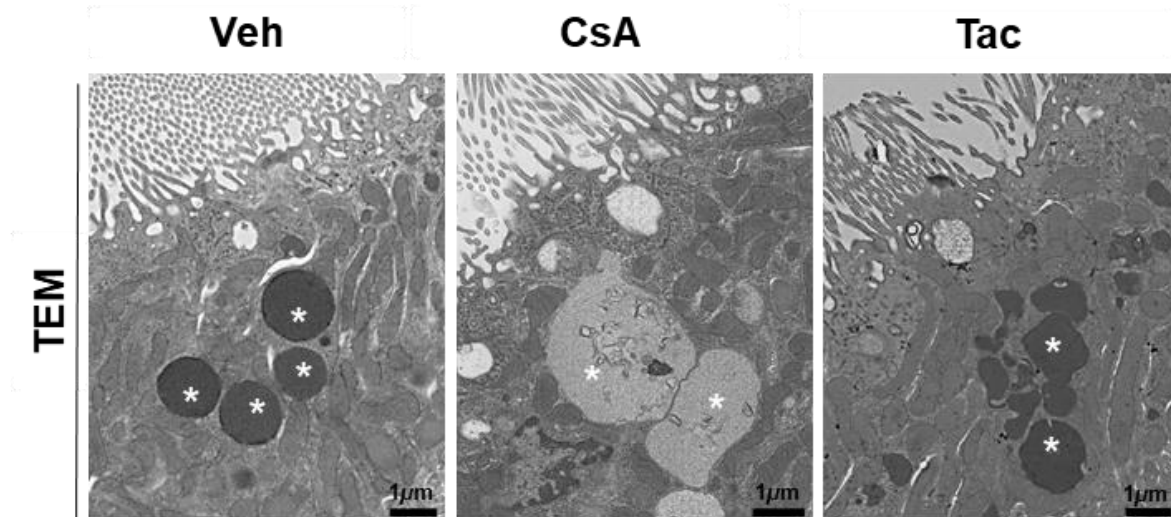

Figure 19. Lysosomal changes in proximal tubule. Transmission electron microscopy (TEM) images revealed distinct lysosomal phenotypes in the PCT epithelia based on the treatment received. In the vehicle group, large and regular lysosomes (asterisks) are observed in the middle of the epithelium. In CsA-treated samples, multiple heterolysosomes (asterisks) form chains in an apico-basal orientation. In Tac-treated samples, the lysosomes exhibit regular but multiform shapes (asterisks) and contain heterogeneous inclusions.

TUNEL immunofluorescence showed high numbers of nuclear signals in the PCT and PST of the CsA-treated group. In contrast, a few scattered signals were observed in the Tac-treated group. In the vehicle-treated group nuceli were unreactive (Figure 20A-F). This finding was confirmed through numerical measurements (Figure 20G-J).
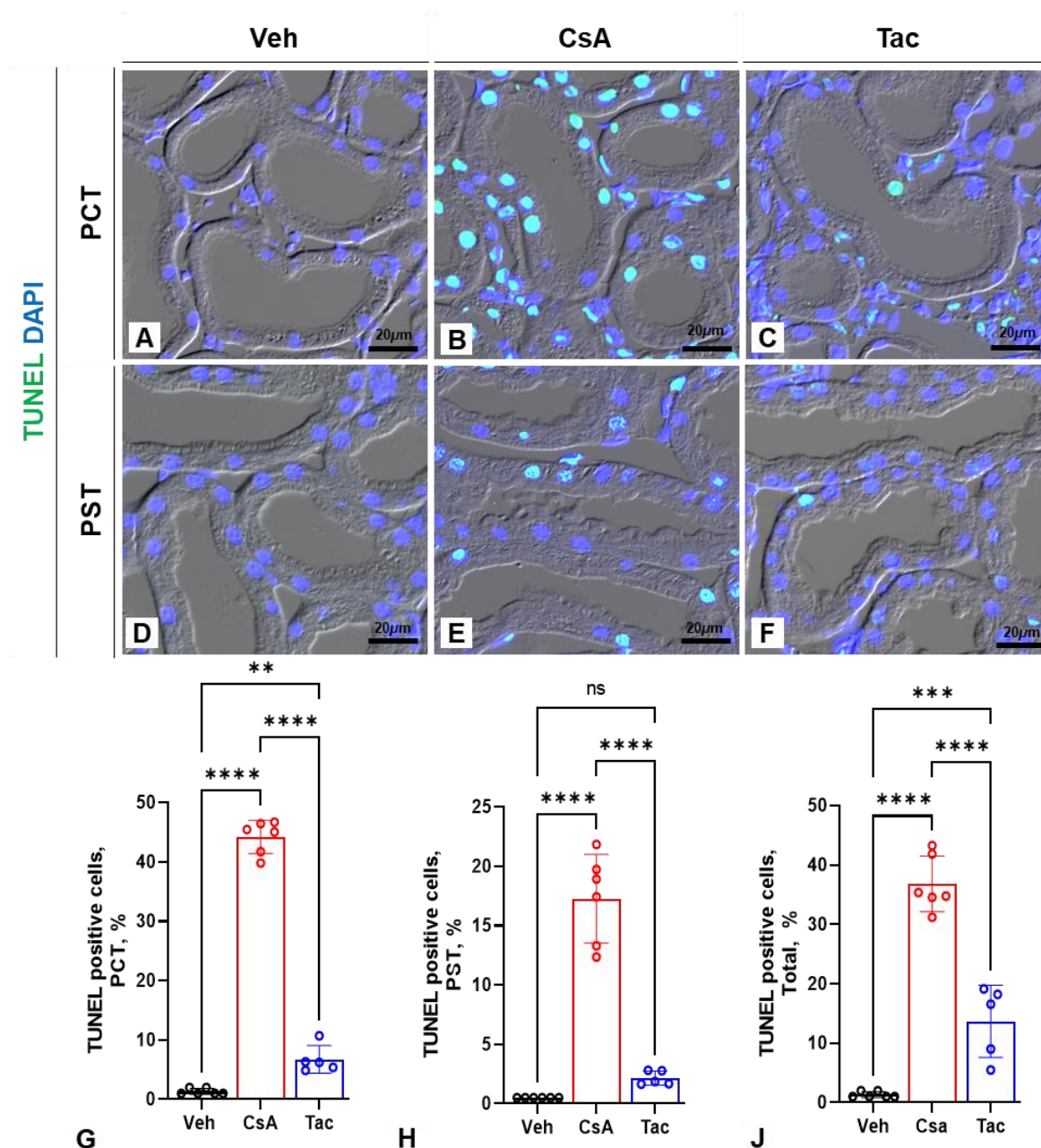
Figure 20. Proximal tubular TUNEL labeling. (A-F) Immunofluorescence staining using TUNEL assay reveals a green nuclear signal in representative images. No signal is detected in the PCT profiles of a vehicle (Veh) sample (A), while a strong signal is observed in the PCT profiles of a cyclosporine A (CsA) sample (B), and a weaker signal is present in scattered PCT profiles in the tacrolimus (Tac)-treated sample (C). Similar results are observed in the PST, with a lower density of signal in CsA samples. (G-J) Bar diagrams present the quantitative evaluation of TUNEL labeling in the PCT (G) and PST (H) regions. The total TUNEL signal in the entire kidney is also displayed for comparison (J). The values represent the percent of total nuclei counts. Data represents the mean ± SD; ** $P < 0.01$, *** $P < 0.001$ **** $P < 0.0001$; ns: not significant. Blue nuclear staining, DAPI; DIC optics were used to capture the structure. Bar indicate magnification.

Immunofluorescence staining and western blotting for catalase, a marker of oxidative

stress resistance, showed significantly higher signals in the CsA- than in the Veh-

treated group; however, there was no difference between both CNI groups (Figure 21A-E).
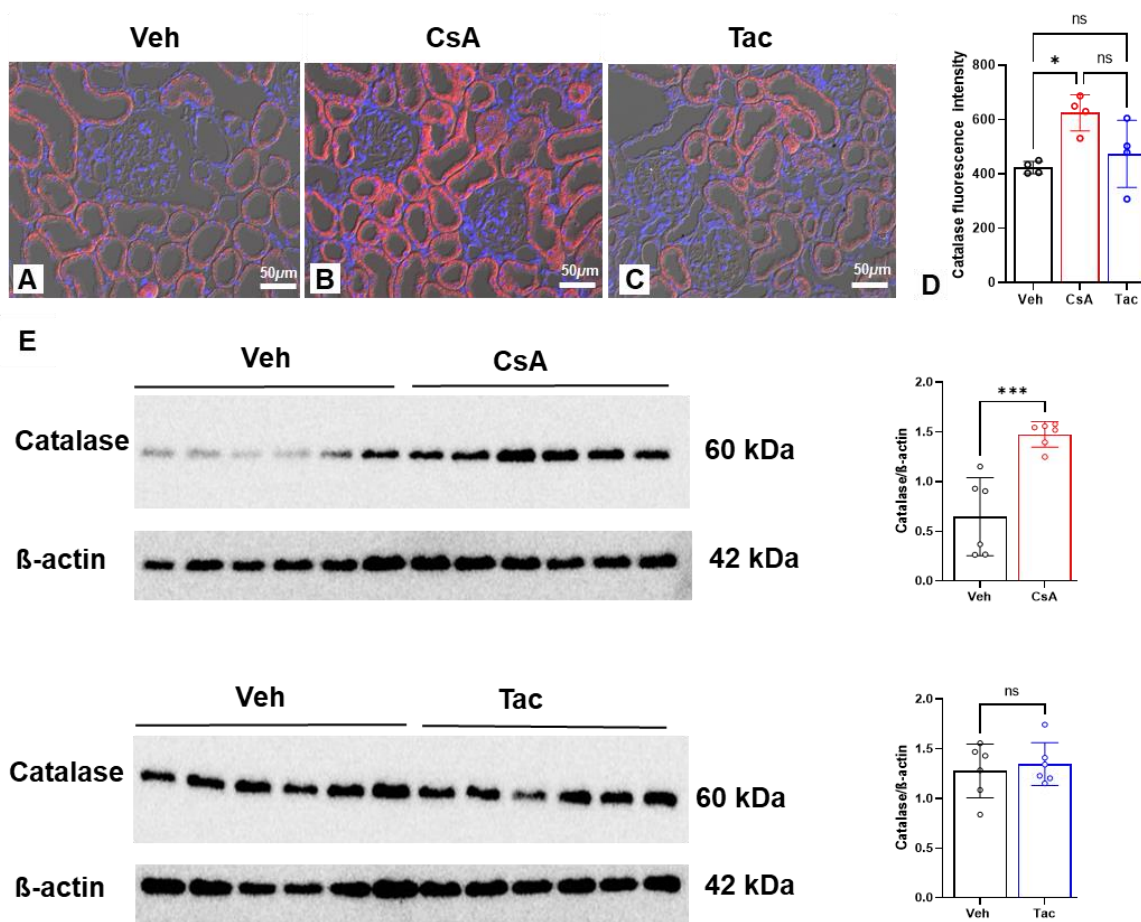

Figure 21. Catalase abundance in the proximal tubule. (A-D) Immunofluorescence staining using an anti-catalase antibody reveals abundant staining in the PCT of vehicle (Veh) (A), cyclosporine A (CsA) (B), and tacrolimus (Tac) samples (C). The inserts in the images provide a closer look at the punctuated nature of the signal, and DAPI is used for blue nuclear staining, DIC optics were used to capture the structure. It is worth noting that the signal appears intensified in CsA samples. (D) A bar diagram illustrates the quantification of the enhanced fluorescence signal per unit sectional area obtained from catalase-immunostained sections. Data represents the mean ± SD; *$P<0.05$, *** $P<0.001$; ns, not significant. Bars indicate magnification. (E) Western blots display the presence of immunoreactive catalase (60 kDa) in kidney extracts from CsA, Tac, and their respective vehicle groups (n=6 each). ß-actin (42 kDa) is included as a loading control. Densitometric evaluation is provided on the right side of the respective blots. Data represents the mean ± SD; *** $P < 0.001$; ns, not significant.

The CD31 immunofluorescence analysis revealed a robust signal in the capillary network of the cortical interstitium in the vehicle-treated group, as illustrated in Figure 22 A. In the CsA- and Tac-treated groups, there was no change of capillary signal

intensity in intact tissue regions, while fibrotic regions displayed many rounded, sprouting capillaries that were more strongly positive for CD31 (Figure 22 B and C). Western blots confirmed these increases in CD31 expression (Figure 22 D). Changes in the number of interstitial endothelial fenestrations were calculated on TEM sections. It was observed that CNI had significantly reduced the fenestral pore density with minor decreas in CsA but significant reduction in Tac (Figure 22 E-H).
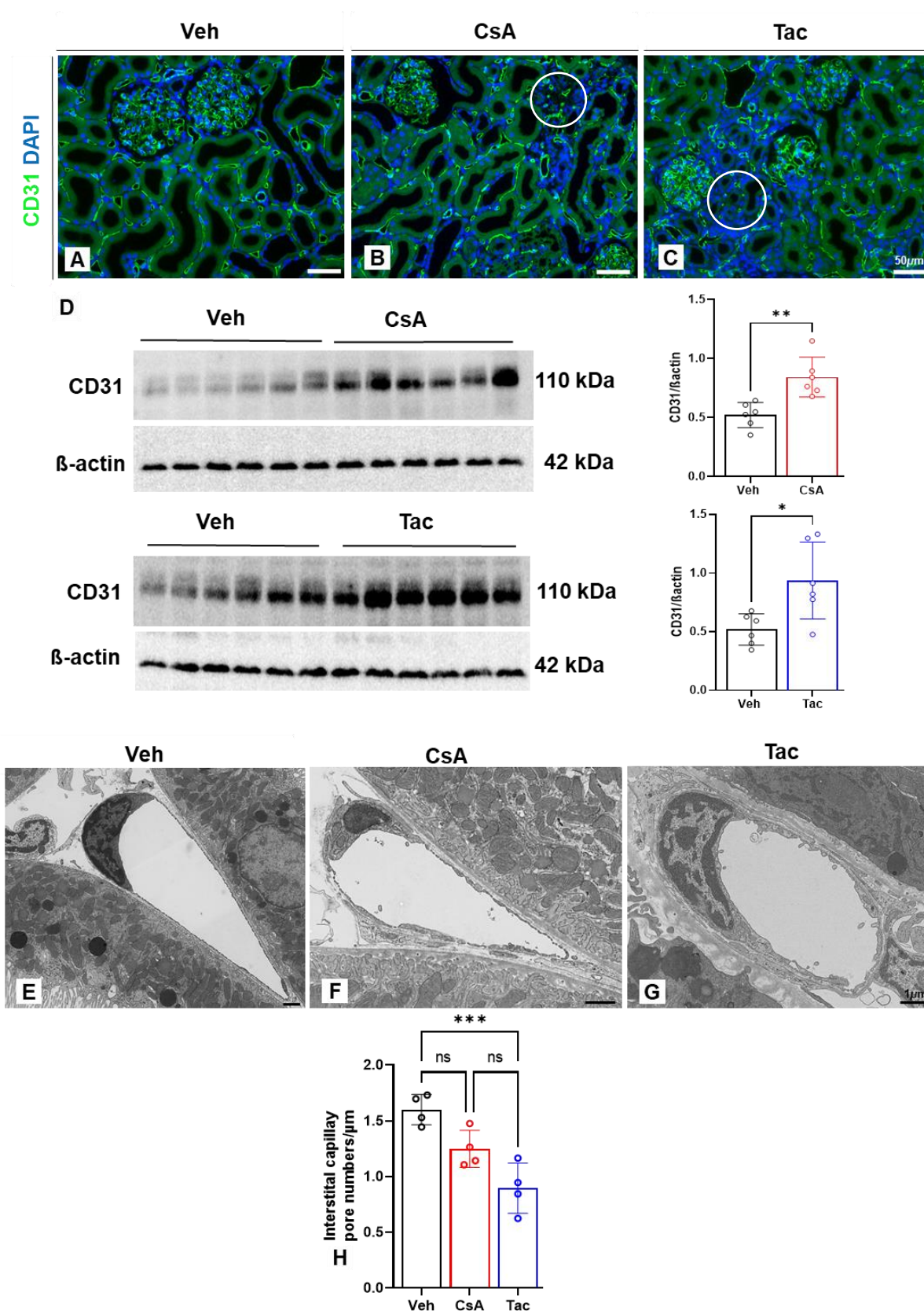
Figure 22. Changes in cortical interstitial vasculature. (A-C) Immunofluorescence staining using an anti-CD31 antibody reveals strong labeling of interstitial capillaries adjacent to proximal tubule profiles in a representative vehicle (Veh) sample (A). In cyclosporine A (CsA) and tacrolimus (Tac) samples, the signal in intact interstitial spaces appears similar to the Veh

level (B, C). However, in fibrotic foci, numerous strongly positive capillaries of a rounded, sprouting type can be observed (encircled areas in B, C). DAPI is used for nuclear blue staining. (D) Western blots display the presence of immunoreactive CD31 (110 kDa) in kidney extracts from CsA, Tac, and their respective Veh groups (n=6 each). ß-actin (42 kDa) is included as a loading control. Densitometric evaluation is provided on the right side of the respective blots. Data represents the mean ± SD; *$P < 0.05$, **$P < 0.01$. (E-G) Transmission electron microscopy (TEM) images of cortical interstitial capillaries reveal normal fenestrated endothelium in a representative cortical Veh sample (E). In CsA (F) and Tac (G), sprouting-type capillaries within cortical fibrotic foci are demonstrated, with the absence of fenestrae observed in both cases. Additionally, endothelial swelling or ridge formation is particularly noticeable in (G). (H) A bar diagram illustrates changes in pore density quantified from TEM sections. Data represents the mean ± SD; ***$P < 0.001$; ns, not significant. Bars indicate magnification.

3.2 Multi-omics

We conducted whole-kidney total mRNA next-generation sequencing (RNA-Seq) on 4 to 6 rats for each treatment group to gain insights into the *in vivo* molecular mechanism underlying CNI nephrotoxicity and provide a complete data source meant to be useful in future CNI nephrotoxicity investigations. To examine gene expression profiles in depth, we used fragments per kilobase of transcript per million mapped read (FPKM) values when analyzing the RNA-seq data at the gene level. Significantly differentially expressed genes (DEGs) were identified using the *DESeq2* R package using an adjusted *P* value threshold of 0.1 to filter DEGs in each CNI-treated group relative to the vehicle-treated group. Our data showed that CsA and Tac induced the differential expression of 1003 (507 upregulated and 496 downregulated) and 323 (105 upregulated and 218 downregulated) genes, respectively. The common and unique DEGs from the different CNI-treated groups were visualized using a Venn diagram. We found that only ten DEGs (*Ren*, *Csdc2*, *Tns4*, *Egr1*, *Gabrp*, *Dcdc2*, *Gata2*, *Mapkapk3*, *Lpin2*, and *Prkab1*) were commonly upregulated and six DEGs downregulated (*Calb1*, *Sfrp2*, *Slc16a7*, *Slc2a4*, *Osbpl1a*, and *Prlr*) in the two CNI-treated groups (Figure 23).
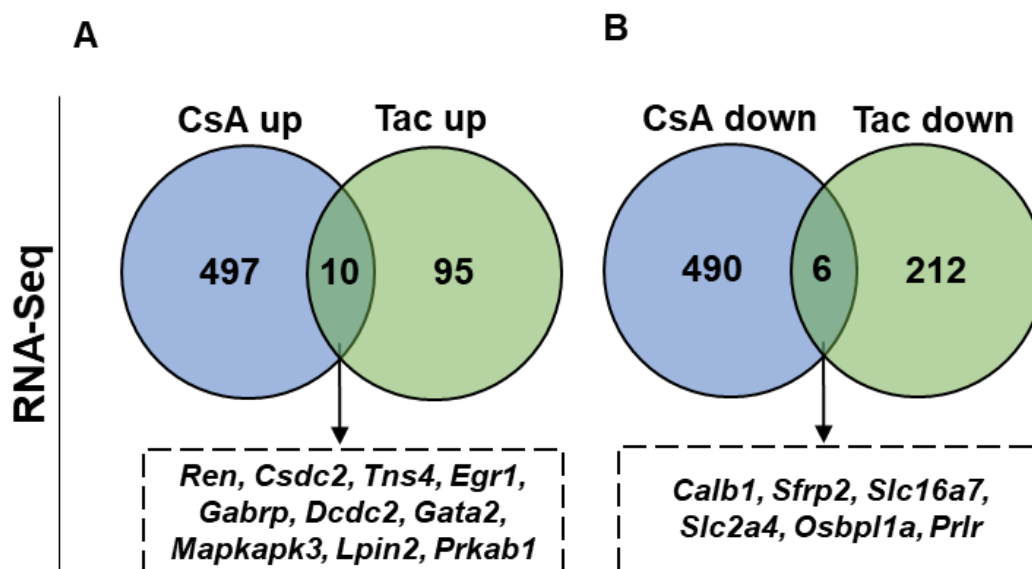
Figure 23. Venn diagram of RNA-seq analysis. (A-B). Differentially expressed genes.

Next, we performed gene ontology (GO) biological process enrichment analysis and pathway enrichment analysis (hallmark [HM] gene sets, canonical pathway gene sets derived from Reactome [RC], WikiPathways [WP], and Kyoto Encyclopedia of Genes and Genomes [KEGG]) of CNI-induced DEGs using Enrichr. Pathway analyses of DEGs indicated that some of the genes upregulated by CsA were associated with TNF-alpha signaling via NF-κB, response to oxidative stress, apoptotic process, response to hypoxia, actin cytoskeleton organization, vasculature development, and glomerular visceral epithelial cell differentiation. In contrast, some of the genes downregulated by CsA were associated with proximal tubule transport and metabolic pathways. In addition, some of the genes upregulated by Tac were associated with biological oxidation, negative regulation of TORC1 signaling, renin-angiotensin system, oxidative stress-induced senescence, blood vessel endothelial cell proliferation involved in sprouting angiogenesis, and vascular wound healing. In contrast, some genes downregulated by Tac were associated with the AMPK signaling pathway, vasculature development, mTORC1 signaling, and actin filament organization. These findings were

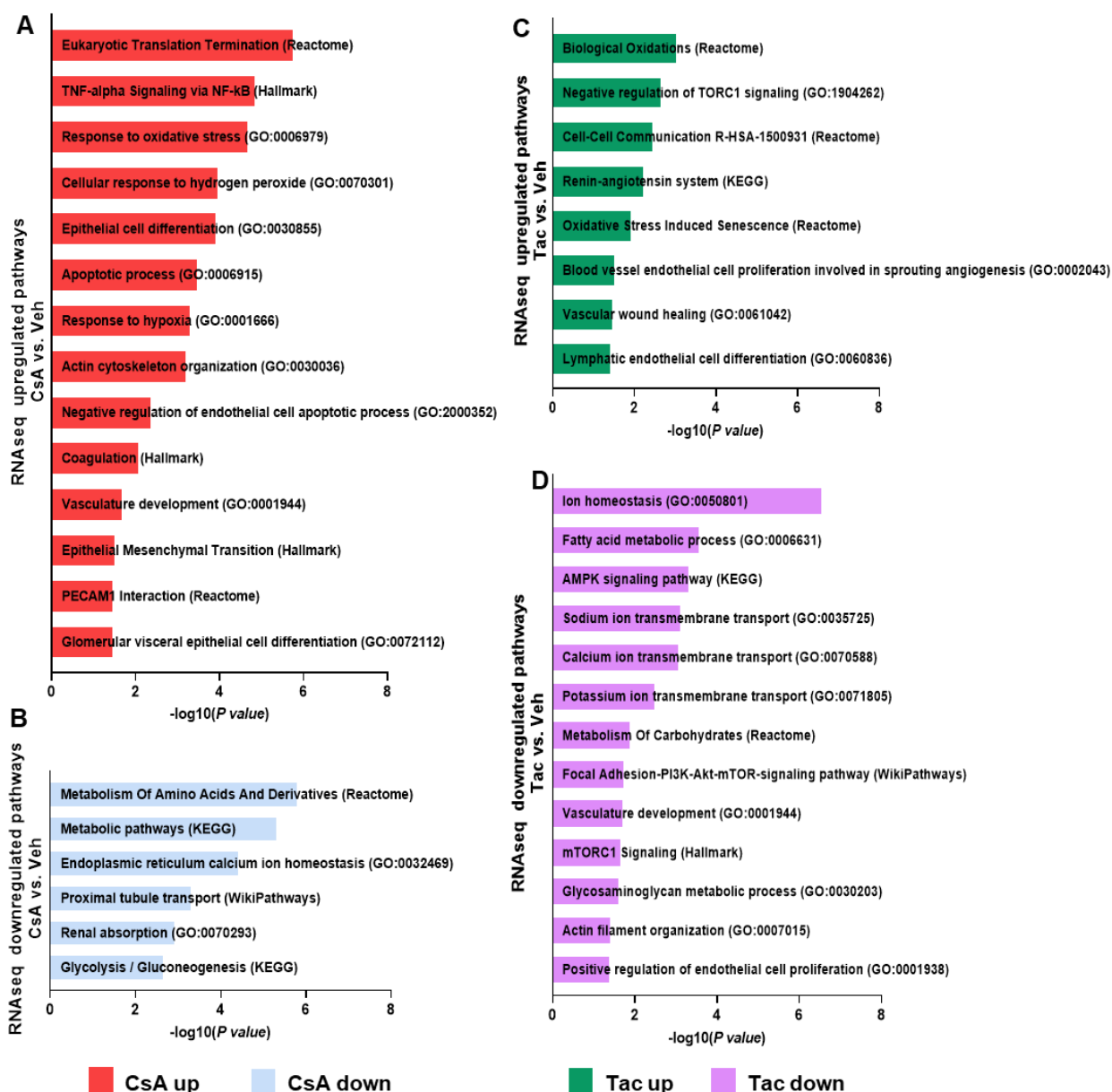consistent with typical Tac-induced morphological changes (Figure 24).

Figure 24. Pathway enrichment analysis of differentially expressed genes affected by CNI treatments. Treatment with CsA and Tac leads to different molecular pathway responses in chronic CNI nephrotoxicity. Significantly enriched pathways in genes upregulated (A) and downregulated (B) in CsA versus vehicles. Significantly enriched pathways in genes upregulated (C) and downregulated (D) in Tac versus vehicles. Term lists used in this analysis were GO_Biological_Processes, WikiPathways, Reactome, KEGG, and Hallmark to determine enriched processes and pathways from DEG (EnrichR webtool). Horizontal bar lines represent *P* value cutoff (*P* < 0.05).

We conducted a comprehensive quantitative global proteomics analysis using large-scale LC-MS/MS to investigate protein-level responses. Following quality assessment we identified 115 differentially expressed proteins (DEPs) after CsA treatment (52 up-

and 63 downregulated with an adjusted $P < 0.1$) and 269 DEPs after Tac treatment (199 up and 70 downregulated) relative to the vehicle-treated group. The similarities and differences in the DEPs between CsA and Tac treatment were visualized using a Venn diagram. We found that only three DEPs were commonly upregulated (CES2H, ETHE1, and REN1) and ten DEPs downregulated (ALDH5A1, ATP2B4, BCAT2, CALB1, CNNM2, PFKM, PRPS2, SLC12A3, SLC8A1, and STK39) in the two CNI-treated groups (Figure 25).
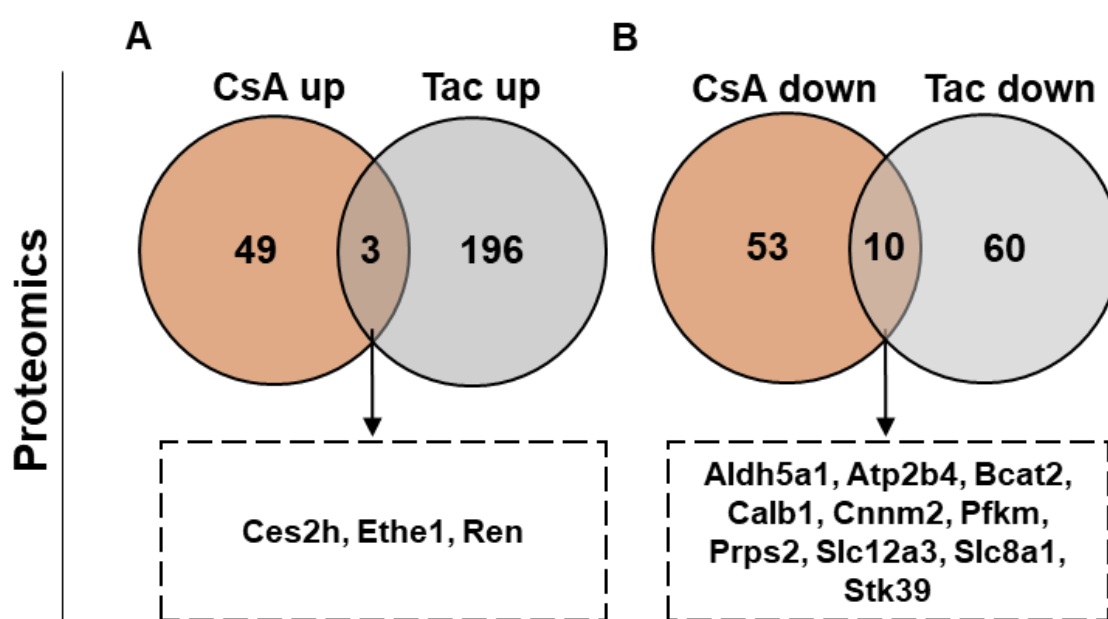

Figure 25. Venn diagram of proteomic analysis. (A-B). Differentially expressed proteins.

We performed GO and pathway analyses to investigate the molecular processes and biological pathways associated with the DEPs in all comparisons. Pathway enrichment analyses showed that the upregulated DEPs were enriched in the peroxisome, the regulation of vascular endothelial cell proliferation, apoptosis, the unfolded protein response (UPR), blood vessel development, and autophagy. DEPs associated with metabolic pathways were downregulated in the CsA-treated group. DEPs associated with the response to oxidative stress, TNF-alpha signaling pathway, and oxidation by cytochrome P450 were upregulated in the Tac-treated group, while those associated

63

with mTORC1 signaling, the AMPK signaling pathway, and glomerular visceral epithelial cell differentiation were downregulated (Figure 26).
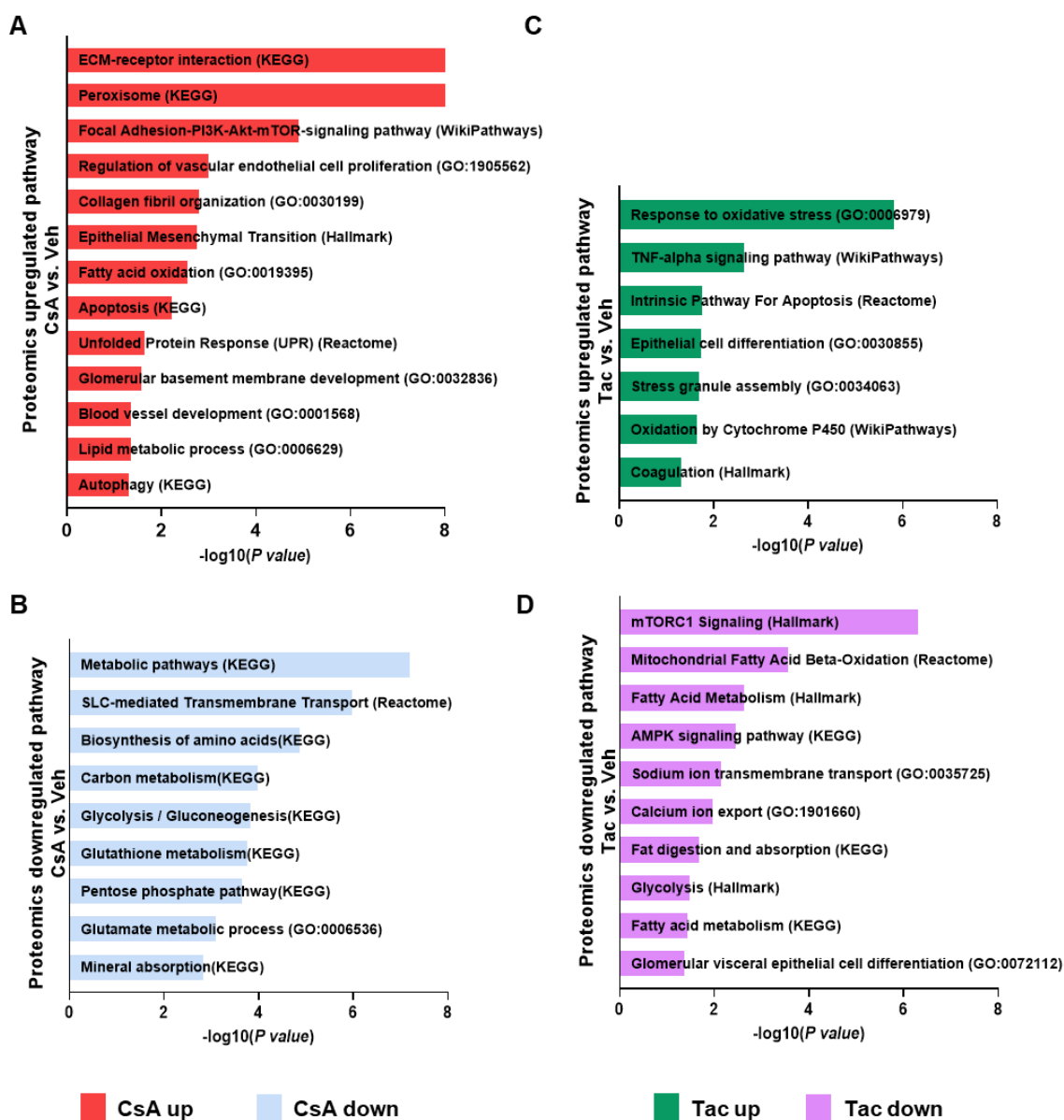

Figure 26. Pathway enrichment analysis of differentially expressed proteins (DEPs) affected by CNI treatments. Significantly enriched pathways in proteins up- (A) and downregulated (B) in CsA versus Veh. Significantly enriched pathways in proteins up- (C) and downregulated (D) in Tac versus vehicles. Term lists used in this analysis were GO_Biological_Processes, WikiPathways, Reactome, KEGG, and Hallmark to determine enriched processes and pathways from DEPs (EnrichR webtool). Horizontal bar lines represent P value cutoff ($P <$ 0.05).

Next, we performed quantitative phosphoproteomic studies of whole kidney lysates using multiplex tandem mass tag labeling coupled with liquid chromatography-mass spectrometry. A comparison of the CsA- and Veh-treated groups identified 59

significantly altered phosphopeptides (42 were upregulated and 17 were downregulated with an FDR < 0.5). A comparison of the Tac- and Veh-treated groups identified 60 significantly altered phosphorylation sites (35 were upregulated and 25 were downregulated with an FDR<0.5; Figure 27).
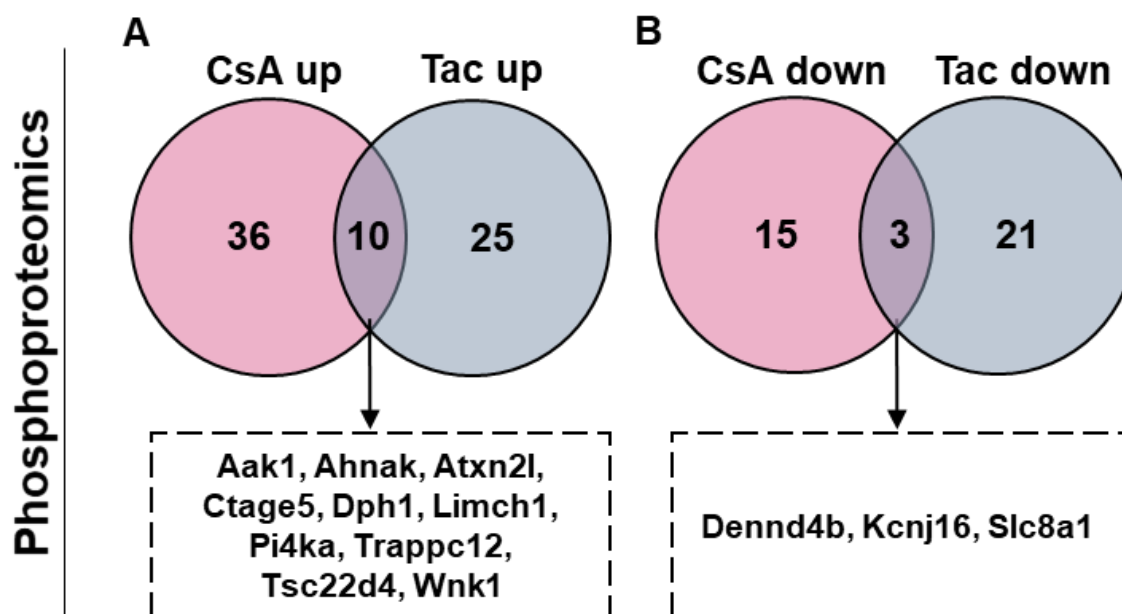

Figure 27. Venn diagram of phosphoproteomic analysis. (A-B). Differentially expressed phosphoproteins.

The differentially expressed phosphoproteins (DEPPs) were subjected to functional enrichment analysis using GO databases to identify potential signaling pathways involved in the renal phosphoproteome. Among the upregulated pathways, the most relevant for the CsA-treated group were the calcineurin-NFAT signaling cascade and the regulation of the response to endoplasmic reticulum stress. The DEPPs in the Tac-treated group were enriched in multiple biological processes, including phosphorylation and actin filament organization (Figure 28).
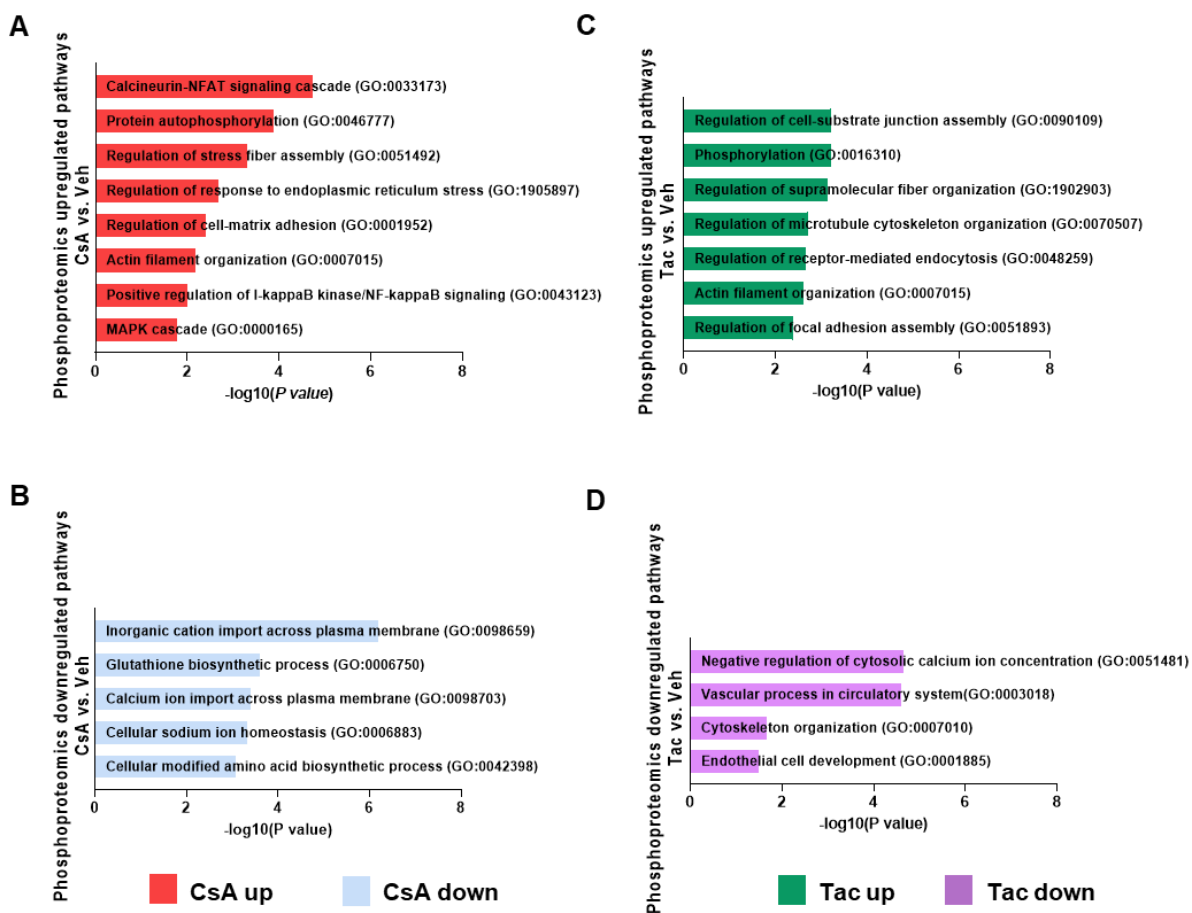
Figure 28. Pathway enrichment analysis of differentially expressed phosphoproteins (DEPPs) affected by CNI treatments. Significantly enriched pathways in phosphoproteins up- (A) and downregulated (B) in CsA *versus* vehicles. Significantly enriched pathways in phosphoproteins upregulated (C) and downregulated (D) in Tac versus vehicles. Term lists used in this analysis were GO_Biological_Processes to determine enriched processes and pathways from DEPPs (EnrichR webtool). Horizontal bar lines represent P value cutoff ($P < 0.05$).

The observation that genes involved in the vasculature and in blood vessel development pathways were significantly downregulated in the Tac- but upregulated in the CsA-treated group is notable. These findings support our hypothesis that Tac has a more deleterious impact on the glomerulus and vasculature. It is plausible that some altered pathways are associated explicitly with vascular development and endothelial proliferation. These multi-omic results indicate that the nephrotoxic effects of CsA and Tac may include differentially regulated pathways. CsA-treated samples showed upregulated levels of PDIA5 and phosphorylated PERK (EIF2AK3) which are key components of the UPR pathway. HMGB1 and CTSD, which contribute to

66

regulating autophagy, were also upregulated. In contrast, Tac-treated samples showed downregulated *Prkce*, *Prkd1*, *Ptger4*, and *Cav1* genes and CAV1, DDAH2 and phosphorylated PRKD1 protein expression. These factors are associated with endothelial function and contribute to vascular changes. Furthermore, we observed downregulation of SYNPO (transcript and protein), PALLD (transcript and phosphoprotein), PODXL (protein), and phosphorylated CD2AP all of which are relevant to podocyte biology.

The findings from both proteomic and phosphoproteomic analyses corresponded to the transcriptomic data and provided further evidence of a significantly upregulated UPR pathway in CsA- but not in Tac-treated samples. This observation was validated by western blotting which confirmed the increased expression of UPR marker proteins after CsA treatment. Specifically, the phosphorylation levels of PERK, IRE1α, sXBP1, and caspase-3 cleavage were significantly elevated after CsA treatment (Figure 29).
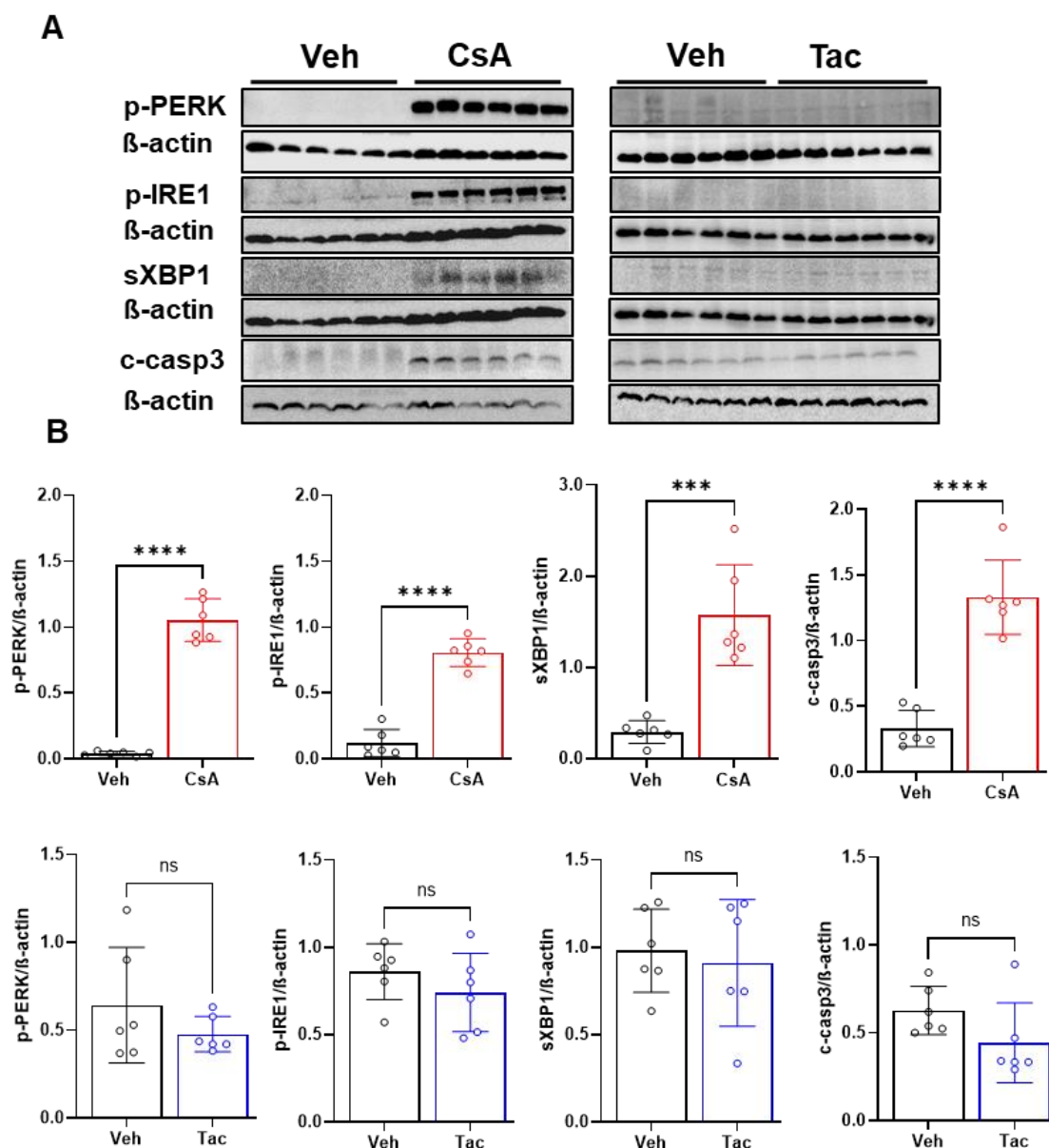
Figure 29. Western blot verification of UPR parameters. (A) p-PERK (Thr980, 150 kDa), p-IRE1 (Ser724, 110 kDa), sXBP1 (55 kDa), c-casp3 (17 kDa), and ß-actin (42 kDa), rat kidney. (B) Below, corresponding densitometric evaluations are shown in the bar graphs. Data represents means ± SD; n=6 per group. *$P < 0.05$, **$P < 0.01$, ***$P < 0.001$, ****$P < 0.0001$; ns, not significant.

We compared all DEGs ($P < 0.05$) to gain insight into changes specific to different compartments. Specifically, we used a previously published list of 193 genes specific to the proximal tubule in rat kidneys. We observed 100 DEGs in the CsA-treated group (20 up- and 80 downregulated) but only 33 DEGs in the Tac-treated group (25 were upregulated and 8 were downregulated). These findings confirm that CsA treatment

results in more substantial changes in the proximal tubule than Tac treatment Figure 30).

Differentially expressed PT marker genes / Csa vs. Veh
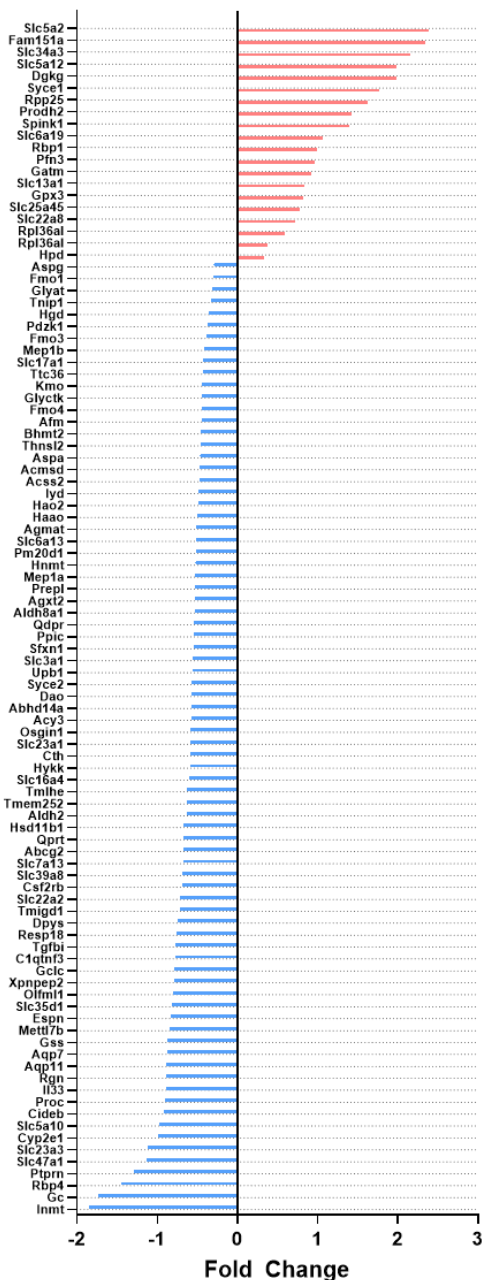
Differentially expressed PT marker genes / Tac vs. Veh
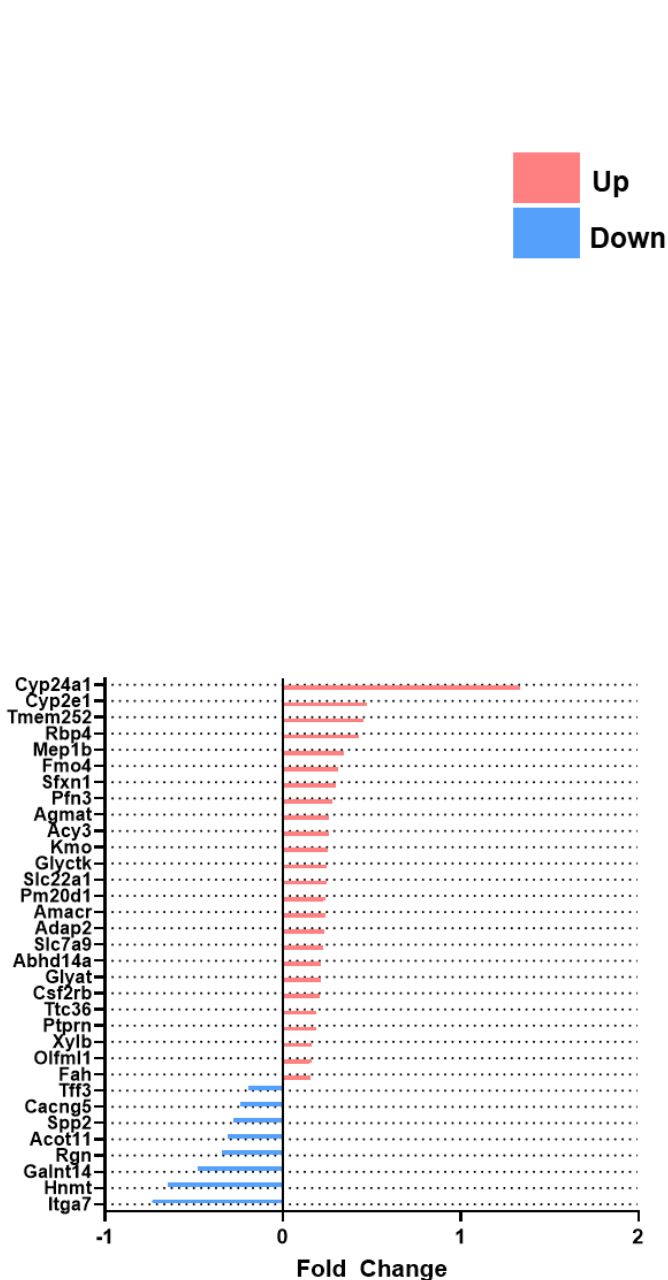
Down	Up
80	20

Down	Up
8	25

Figure 30. Differentially expressed genes with endogenous expression in proximal tubule. Bar graph on a published RNA-seq data set of segmental profiles of the adult rat nephron (Lee et

al. 2015) showing 193 genes endogenously expressed in proximal tubule, 100 of these are differentially expressed in the CsA group but only 33 in Tac (P value < 0.05).

We further assessed the differential mRNA expression levels of established kidney injury markers. *Timp2*, osteopontin (*Spp1*), *Ngal* (*Lcn2*), *Il18*, and *Kim1* (*Havcr1*) showed significantly increased expression in the CsA-treated samples. In contrast, only *Kim1* and *Ngal* showed significantly increased expression in the Tac-treated samples (P < 0.05; Figure 31).
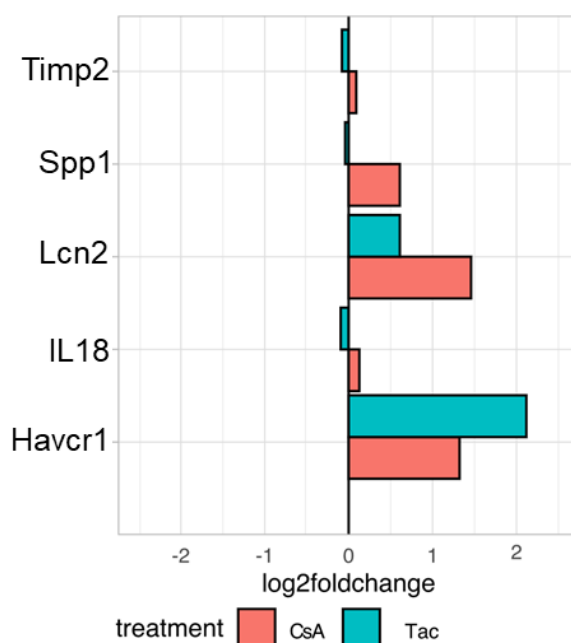
Figure 31. Evaluation of kidney injury markers. Bar graph displaying the degree of differential expression for known injury marker genes (adjusted P < 0.05).

Multiomics data further suggested relevant changes in the AMPK-mTORC1-TFEB pathway in the CNI-treated groups. We showed by western blots that phospho-mTOR, phospho-AMPK, and TFEB were differentially upregulated in the CsA-treated group. In contrast, mTOR, phospho-mTOR, AMPK, phospho-AMPK, and TFEB were downregulated in the Tac-treated group (Figure 32).
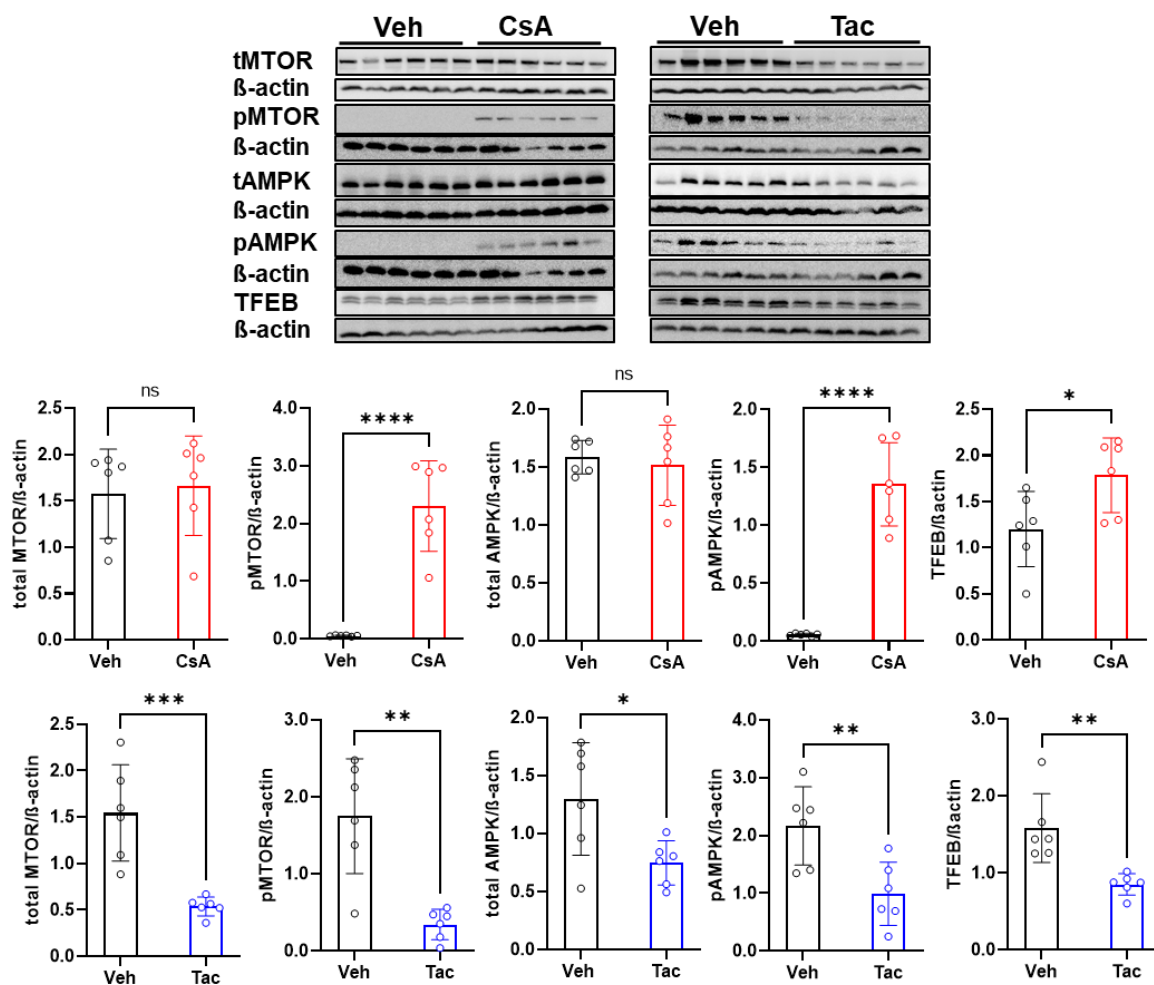
Figure 32. Western blot verification of AMPK-mTORC1-TFEB pathway. Total mTOR (290 kDa) pmTOR (Ser2448; 290 kDa), total AMPK (60 kDa), pAMPK (Thr172, 60 kDa), TFEB (70 kDa), and ß-actin (42 kDa), in whole kidney homogenates from CsA and Tac treated rats. Below, corresponding densitometric evaluations are shown in the bar graphs. Data represents means ± SD; n=6 per group. *$P < 0.05$, **$P < 0.01$, ***$P < 0.001$, ****$P < 0.0001$.

Therefore, we propose a mechanism by which TFEB regulation may contribute to

CsA and Tac nephrotoxicity (Figure 33).
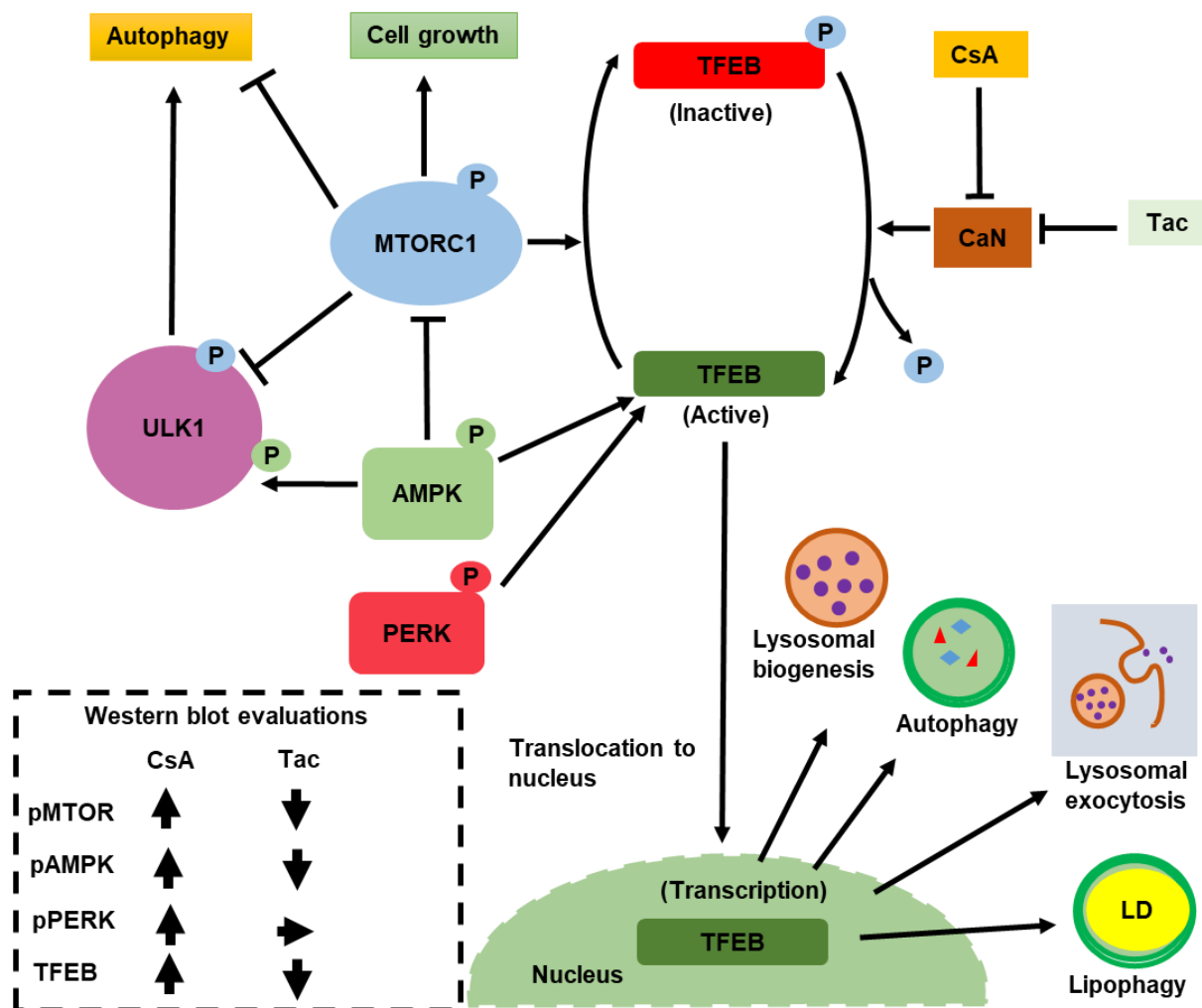
Figure 33. Proposed mechanism of how the regulation of TFEB contributes to CsA and Tac nephrotoxicity. mTOR, AMPK, and UPR are activated consequent to CsA effect, resulting in, increased TFEB expression, stimulating lysosome biogenesis, autophagy, and lysosomal exocytosis. Contrastingly, Tac downregulates TFEB, with opposing downstream effects. Box with interrupted lines indicates regulatory differences between CsA and Tac. CaN, calcineurin; LD, lipid droplet; P, phosphate (Own design).

4. Discussion

In this study, we used an integrative approach to investigate the mechanisms underlying chronic nephrotoxicity associated with CNI, specifically focusing on the differential pathogenesis between CsA and Tac. We used high-resolution histopathology and comprehensive multi-omics (RNA-seq, proteomics, and phosphoproteomics) analyses to explore and identify novel protein signatures associated with CNI nephropathy. We observed distinct responses to the two treatments and identified potential biomarkers specific to each CNI.

4.1 Physiological parameters and renal function

In this study, both CNIs caused renal dysfunction, indicated by significantly increased BUN and decreased creatinine clearance and fractional sodium excretion. The whole blood trough levels of both CNIs agreed with published data in rodents (Andoh et al. 1996; Shihab et al. 2000; Klawitter et al. 2010).

4.2 Histopathology overview

The overall pathological assessment revealed significant tissue damage in both treatment groups, with only minor differences observed in the cortical location. These findings are consistent with previous studies on early chronic nephrotoxicity induced by CsA or Tac in rat models (Fasel et al. 1987; Stillman et al. 1995). In order to detect structural histological damage and fibrosis, kidney morphology was examined in paraffin sections by Sirius red and anti-α-SMA staining. The presence of demarcated foci characterised by atrophic tubules, partially retracted glomeruli, mild fibrosis with induced α-SMA, and moderate inflammation with increased CD45-positive inflammatory cells validated our approach to studying CNI nephrotoxicity at its subclinical stage before advanced pathology obscures crucial regulatory or phenotypic

changes at their source. Interestingly, these observations also indicated unexpected similarities in the effects of the two CNIs.

4.3 Vascular compartment

Upon detailed examination of the renal compartments, however, we observed significant disparities in the development of nephrotoxicity induced by the two CNIs. Despite the established understanding of CNI-related vasoconstriction, vascular wall alterations, and renin-angiotensin system stimulation our experimental model revealed distinct and notable changes within the vascular compartment. CsA-treated samples showed a greater reduction in creatinine clearance than Tac-treated samples. We observed mild hyalinosis in the solid arteriolar media in CsA-treated samples, while there was a smaller microvascular lumen-to-wall ratio with mildly hypotrophic myocytes in Tac-treated samples. RNA-Seq and proteomic analyses showed that the renin expression level was highly stimulated in both groups. Tac-treated samples showed even higher levels than CsA-treated samples, consistent with preglomerular renin staining.

Several research groups have investigated renin's involvement in the development and progression of CNI nephropathy (Lassila 2002). *In vivo* studies on rat kidneys treated with CNIs have earlier shown renin recruitment in afferent arterioles, leading to substantial hemodynamic alterations in the renal microvasculature (Cui et al. 2011). Previous investigation also revealed a correlation between increased renin, angiotensin II (Ang II) and also ROS levels in rats treated with CsA (Nishiyama et al. 2003). Similarly, it has been reported that Tac induces increased sensitivity of the afferent arteriole to Ang II through RhoA signalling, accompanied by reduced GFR and enhanced ROS production (Wang et al. 2022).

The action of vasodilator prostaglandin E_2 (PGE2), mediated by the G-protein coupled E-prostanoid (EP) receptors EP_1, EP_2, EP_3, and EP_4, may have been involved as well.

In the kidney, the EP$_4$ receptor (*Ptger4*) is primarily expressed in the glomerulus (Breyer and Breyer 2000). *Ptger4* was downregulated in the Tac group, implying a negative effect on eNOS function (Hristovska et al. 2007).

The specific decrease in PKC-epsilon (PKC-ε; *Prkce*) expression observed specifically in Tac-treated samples indicated compromised VEGF signalling. Protein kinase C (PKC) stands for a crucial intracellular signalling pathway comprising 12 distinct serine-threonine kinases. It plays a significant role in multiple cellular processes, including proliferation, hypertrophy, apoptosis, and adhesion. PKC-ε, a recently identified PKC isoform, is involved in signalling associated with cell survival (Ding et al. 2002). Allen et al. showed that taurosporine- and c-Myc-induced apoptosis of vascular smooth muscle cells was protected by insulin-like growth factor 1 (IGF1)-mediated PKC-ε activation (Allen et al. 2005). Compromised VEGF signalling became evident with *Prkce* knockdown in bovine endothelial cells to reduce AKT, eNOS, and ERK1/2 phosphorylation, NOS activity, and VEGF-induced DNA synthesis. This in turn may have been related with decreased VEGFR2 tyrosine phosphorylation and VEGFR2 protein and mRNA expression (Rask-Madsen and King 2008).

Caveolae are tiny invaginations found in plasma membranes, expressing caveolin, a 21 to 24 kDa protein that exists in multiple isoforms (caveolin-1, 2, and 3). Caveolin-1 (*Cav1*) is a versatile protein and primary constituent of caveolar membranes to transmit signals adjusting vascular tone, angiogenesis, endocytosis, and transcytosis (Vallés et al. 2007). Our findings of decreased *Cav1* mRNA and protein levels in Tac- but not in CsA-treated samples provided further evidence of impaired VEGF function, eventually causing reduced NO production (Sonveaux et al. 2004; Tahir et al. 2009).

The specific increase in DDAH2 expression in the Tac group may have affected vascular function further. DDAH2 is responsible for breaking down endogenous NOS inhibitors such as ADMA and monomethyl arginine, suggesting a possible

compensatory mechanism in Tac-treated samples to preserve an adequate NO level (Baylis 2008). ADMA is an endogenous amino acid in the bloodstream and excreted in urine. It is also a competitive inhibitor of all three NOS isoforms (Vallance and Leiper 2005). Multiple studies have shown a correlation between increased plasma ADMA levels and CKD (Leone et al. 1992; Zoccali et al. 2001; Matsumoto et al. 2007). The primary metabolic pathway for ADMA also involves its enzymatic breakdown by the enzymes DDAH1 and DDAH2. DDAH2 is predominantly found in vascular endothelia (Hannemann et al. 2022).

Elevated leukocyte attachment, shown by CD45 immunofluorescence, was observed more in Tac- than in CsA-treated samples which suggests inflammation of and, hence, damage to the endothelial surface (Gallego et al. 1996; Rodrigues-Diez et al. 2016; Karolin et al. 2022). In clinical practice, the primary purpose of using CD45 antisera is to validate the existence of inflammatory cells (Zheng and Epstein 2021). Inflammation, in turn, may impair vascular function (Charo and Taubman 2004).

The upregulation of adhesion molecules like ICAM-1, VCAM-1, and CD31 can be understood as additional indication of inflammatory activation (Gu et al. 2017). In this study, activation of endothelial CD31 in both groups may suggest a protective response to changes in shear stress or serve as an adaptation for leukocyte migration (Wang et al. 2005; Cheung et al. 2015; Sluiter et al. 2021).

4.4 Glomerular compartment

CNIs have been identified as potential causes of glomerular injury, contributing to renal dysfunction in various clinical scenarios. Analyses of patient biopsies with CNI-induced nephrotoxicity revealed distinct forms of glomerular damage such as thickening of glomerular capsule, glomerular congestion, or presence of focal segmental or global sclerosis which collectively contribute to development of chronic allograft nephropathy. (Nankivell et al. 2016). Moreover, a recent study by Kidokoro et al. explored the

underlying mechanisms of Tac-induced glomerular injury in an experimental model. They found that Tac promoted oxidative stress and inflammation within the glomeruli, resulting in glomerular injury (Kidokoro et al. 2012). Findings so far underscore the importance of monitoring glomerular function in patients receiving CNI and discuss alternative immunosuppressive strategies to mitigate CNI-induced glomerular injury in clinical practice.

In this thesis work glomerular phenotypes showed several significant changes including tuft retraction and a decrease in filtration slit density which both occurred to similar extent in CsA- and Tac-treated samples. Also observed, glomerular tuft retraction may have been associated with decreased microvascular perfusion and capillary collapse as observed previously (Perico et al. 1991; Perico et al. 1996; Kim et al. 2016).

Early and advanced glomerular affection in CsA- and Tac-treated samples was characterised by α-SMA staining intensities of Bowman's capsule, and activated parietal epithelium was indicated by enhanced CD44 signal, and adherent inflammatory CD45$^+$ cell accumulations characterized the pericapsular interstitium. Increased CD44 expression at this site has recently been recognised as a valuable marker of early CNI nephrotoxicity in human grafts (Hayashi et al. 2022). These characteristics along withfibrous podocyte synechiae indicated the early phases of sclerotic lesions and initiation of inflammation in our model, as confirmed elsewhere (Kuppe et al. 2015; Bernhardt et al. 2017).

Assessment of filtration slit density in podocytes by NIPOKA revealed crucial characteristics of podocytopathy in our model, making use of 3D-SIM and PEMP (Siegerist et al. 2017; Artelt et al. 2018b). A significant reduction in the density of filtration slits could thus be shown in both CNI groups. Adding 3D SEM technology, we further demonstrated that foot process effacement was in fact more extensive in Tac-

than in CsA-treated samples, which was coincident with a notable decrease in fenestral pore density within the glomerular capillaries, higher in Tac than in CsA. These changes may well be associated with altered VEGF signalling. The role of VEGF in regulating endothelial fenestration was first proposed by Breier et al., who observed that fenestrated endothelia are typically positioned close to epithelial cells with high VEGF expression. They also noted that mature glomerular podocytes expressed particularly high VEGF mRNA levels (Breier et al. 1992). In line with this, human kidney-specific microvascular endothelial cells had reduced VEGF signalling and fenestrae impairment after CsA treatment (Nagao et al. 2022). Our multiomics data showed that protein kinase D1 (PRKD1) mRNA and phosphorylation levels were specifically lowered in Tac-treated samples. PRKD1 is known to regulate VEGFR2 and may affect the activity of the transcription factor AP-2 through disinhibition (Wang et al. 2019). During development, VEGF expression in podocytes is initiated at the S-shaped stage, coinciding with the migration of glomerular endothelial cells into the cleft prior to development of fenestration (Quaggin and Kreidberg 2008). At this stage, glomerular endothelial cells start expressing VEGFR2, which is sustained throughout their maturation process (Robert et al. 2000). Targeted removal of one VEGF-A allele specifically in podocytes led to the formation of glomeruli with undifferentiated endothelia, i.e., with a flattened and continuous phenotype (Eremina et al. 2003). A mouse study confirmed the effects of VEGF on pore density in conjunction with TNF-α signalling (Xu et al. 2014). In the Tac-treated group, elevated TNF-α levels may have been involved in causing the observed microvascular damage contributing to gradual functional decline, as we concluded from the present multiomic data. These data further revealed that *Cav1* mRNA and protein expression were significantly decreased in Tac-treated samples. This reduction in *Cav1* expression further suggests a potential association with impaired angiogenesis and decreased pore formation in the

glomerular barrier. This finding is consistent with previous studies highlighting the role of CAV1 in angiogenesis and pore regulation (Satchell and Braet 2009; Tahir et al. 2009).

The glomerular endothelium has a protective layer known as the endothelial surface layer (ESL), which comprises a membrane-bound glycocalyx. This ESL comprises negatively charged proteoglycans, glycoproteins, and glycolipids attached to the endothelium. The glycocalyx forms a network that helps to maintain the glomerular barrier's charge-selective function and prevents the leakage of proteins into the urine (Haraldsson and Nyström 2012). Preserving ESL is crucial for preventing endothelial dysfunction and the progression of renal and cardiovascular diseases (Rabelink and de Zeeuw 2015). We detected a significant decrease in the expression of specific ESL products syndecan-4 (*Sdc4*), lumican (*Lum*), and glycoprotein 3 (*Gp3*) in the Tac-treated samples. Therefore, our studies suggest possible glomerular endothelial injury via ESL loss (Ebefors et al. 2019; Khramova et al. 2021).

Podocytopathy may cause glomerulosclerosis, and in many types of glomerular disease, podocyte loss gradually contributes to CKD (Kim et al. 2001). In our results, deterioration of the glomerular filtration barrier was evident through the reduction of WT-1 expression and increase of TUNEL signals, particularly exacerbated in the Tac-treated samples. The decrease in WT-1, a well-established podocyte marker (Guo 2002), suggests a loss of essential barrier functions (Guo 2002; Wagner et al. 2004) and indicates early alterations associated with glomerulosclerosis (Asfahani et al. 2018).

In our hands, the Tac-treated kidneys showed a notable downregulation of key podocyte genes, including palladin, CD2AP, synaptopodin, nephronectin, and podocalyxin. These genes constitute crucial structural components in these cells. Their downregulation indicates greater damage to podocytes in Tac- than in CsA-treated

samples. With altered podocyte shape, motility of their podocyte foot processes should have been impaired (Artelt et al. 2018a; Menon et al. 2022). The decrease in CD2AP phosphorylation at Ser 404, which serves as a stabilising protein in the slit diaphragm, further suggested loss of function in this particular group (Tossidou et al. 2019). Together, while a longitudinal histological cohort study by Nankivell et al. (Nankivell et al. 2016) reported similar glomerular damage scores between CsA- and Tac-treated indivuals, our findings indicate a selectively greater burden on glomeruli in the Tac-treated group, particularly at an early stage.

4.5 Tubular compartment

Previous discussions have extensively addressed tubular damage caused by CNI-nephrotoxicity. However, it has remained unclear whether the damage is primarily due to direct toxicity to the tubular epithelial cells or if it results from upstream effects caused by affected vasculature or glomerular alterations. Published data suggest that the proximal tubule is crucially involved in CNI-associated tubular damage. These studies have reported various distinct patterns of CNI-related abnormalities in the proximal tubule. These included vacuolisation, BBM loss, impaired energy metabolism, atrophy, and fibrotic changes. Of note, no significant causal distinction has been established between CsA and Tac regarding their impact on tubular damage (Mihatsch et al. 1998; Zmijewska et al. 2021). Our study, however, revealed significant differences in proximal tubular damage consequent to these drug applications. Of note, our findings did not show the commonly observed isometric vacuolisation, which is observed acutely in humans chiefly upon CsA administration; this phenomenon is believed to be reversible and caused by temporary ER dilatations (Charney et al. 2009).

Proximal tubular cells are recognised for their high activity in protein synthesis and folding. Consequently, the efficient clearance of misfolded or denatured proteins is

crucial, and this task is primarily performed by the autophagosome/lysosome system (Kirkin et al. 2009). In our study, the significant increase in activated PERK, a critical regulator and essential component of the UPR, along with the upregulation of IRE1, another key UPR transducer, as well as downstream acting spliced XBP1 (sXBP1) indicates the activation of canonical UPR pathways. These are likely responsible for the observed elevation in cleaved caspase-3 (c-CASP3) and apoptosis, specifically in the CsA- but not in the Tac-treated group. Already in previous studies the involvement of the UPR cascade has been detected under chronic CsA administration (Han et al. 2008; Cybulsky 2017; Hetz and Papa 2018). Consistently, our study and those by Fedele et al. (Fedele et al. 2020) and Yilmaz et al. (Yilmaz et al. 2022b) have demonstrated impaired proteostasis and UPR-induced proapoptotic ER stress to occur specifically in CsA- but not in Tac-treated samples at least at short term. Additionally, we observed an upregulation of PDIA5 in the CsA-treated rats, which is a disulfide isomerase required for ATF6 activation; this likely suggests involvement of the third UPR cascade (Higa et al. 2014).

Our main observation was the extensive accumulation and luminal extrusion of multiform heterolysosomes predominantly in the CsA-treated group. The observed upregulation of ADP-ribosylation factor-like protein 8B (*Arl8b*) expression, indicative of increased lysosomal exocytosis, in the proximal tubule of the CsA-treated group provides evidence for the pronounced lysosomal abnormalities identified here (Wu et al. 2020). In contrast, tubular changes in the Tac-treated group showed a much lesser association with lysosomal abnormalities. It remained unclear whether this increase resulted from the division of existing lysosomes or whether CsA stimulated the process of lysosomal biogenesis. TFEB is a key transcriptional regulator controlling lysosomal biogenesis, exocytosis, and autophagy processes (Sardiello et al. 2009). mTORC1 is currently recognised as an effective regulator of TFEB. mTORC1 negatively controls

catabolic processes including autophagy by directly phosphorylating and, thereby, inhibiting TFEB at Ser 211 and 142. The action of TFEB activation is facilitated by AMPK, inhibiting mTORC1 activity. Furthermore, the pharmacological activation of AMPK leads to TFEB nucear translocation, with mTOR phosphorylation unaffected (El-Houjeiri et al. 2019).

ER stress and consequent PERK upregulation may also induce TFEB activation even under CNI condition (Martina et al. 2016b). Our pathway enrichment analysis showed that "mTORC1 signalling" and "AMPK signalling" pathways were significantly downregulated by Tac treatment as opposed to upregulation of the "autophagy" pathway under CsA. Western blots to validate this confirmed that CsA treatment substantially stimulated TFEB expression and phosphorylated mTOR and AMPK levels. Conversely, Tac treatment significantly decreased TFEB, phospho-mTOR, and phospho-AMPK levels. This result suggests that TFEB regulation in response to CsA occurs via AMPK and UPR activation but is independent of calcineurin and mTORC1. TFEB activation by CsA thus promotes the autophagy-lysosomal pathway, which in turn appears to alleviate the accumulation of unfolded or misfolded proteins. Multiple lines of evidence suggest that these specific pathways are predominantly localised in the proximal tubule. This conclusion is supported by previous studies (Han et al. 2008; Yilmaz et al. 2022b) and our findings of selective TUNEL signal and apoptotic cell characteristics. Therefore, it is reasonable to infer that CsA-related cytotoxicity primarily targets this principal tissue component, potentially through the apoptotic branch of the UPR.

Oxidative stress may have added to the observed disorders, indicated by the selective stimulation of catalase in CsA-treated samples and the activation of peroxisomes in the proximal tubules, indicating enhanced ROS scavenging (Godin et al. 2010). This finding suggests that CsA-related cytotoxicity primarily affects proximal tubules.

Additional support for CsA's selective impact on epithelial cells was obtained by comparing our DEG signatures with published library data specific to the proximal tubule. Here, the tenfold fewer transcriptionally downregulated genes observed in CsA- than in Tac-treated samples corresponds to the loss of function in this nephron segment. Further in the CsA group, several products indicate a tendency towards fibrosis and CKD, such as upregulated solute carrier family 5 (sodium/glucose cotransporter) member 2 (*Slc5a2/Sglt2*) pointing to profibrotic changes of the S1 and S2 segments (Castoldi et al. 2021). A few downregulated parameters further characterized the changes in CsA. Diminished expression of hydroxyacid oxidase 2 *(Hao2)* suggests decreased fatty acid metabolism (Li et al. 2022), while downregulated *Qdpr* indicates stimulation of TGFß1 possibly related with fibrosis (Gu et al. 2013). Downregulated transmembrane and immunoglobulin domain containing 3 (*Tmigd3*) may indicate impaired protection from oxidative cell injury (Arafa et al. 2015) upon presumed alteration in radical oxygen handling. Downregulated complement c1q tumour necrosis factor-related protein 3 (*C1qtnf3*) further agrees with enhanced TGFß1 and interstitial fibrosis (Chen et al. 2019b). Downregulated kynurenine 3-monooxygenase (*Kmo*) harmonizes with epithelial injury and allograft rejection (Lassiter et al. 2021).

4.6 Interstitium

Fibrotic areas in both CNI groups showed increased immunoreactive signals for the endothelial cell marker CD31 particularly in regions with sprouting-type capillaries. Elevated CD31 protein abundance under CNI suggests the induction of angiogenesis which may serve as a compensatory mechanism to counteract CNI-induced endothelial toxicity (Park et al. 2010). These findings contradict previous studies in mice that reported decreased CD31 levels after CsA treatment (Labes et al. 2022); the discrepancy could be attributed to species-related differences since mice generally

exhibit milder phenotypes of CNI nephrotoxicity and require higher drug dosage. In addition, reduced fenestration of interstitial capillaries was observed, consistent with the reductions in venous and glomerular endothelial abundance. This effect was not limited to the fibrotic areas but was found also in healthy appearing tissue.

4.7 Medulla

While previous theories have highlighted the significance of distal tubular epithelia within the medulla and cortical medullary rays as the central contributors to CNI nephrotoxicity (Stillman et al. 1995), our data did not support this pattern. We observed only minor fibrotic foci within TAL segments which showed minimal epithelial damage. In fact, collapsed TAL lumina were infrequently observed. Again, this discrepancy may have have been related with differences in model and drug application.

4.8 Limitation of the study

Our study deals with modeling immunosuppression in patients including those who received one or several allografts. Consequently, lack of an alloimmune response in this model of native kidneys is a limitation potentially diminishing its translational impact in the transplant context. Using e.g. transplanted rat kidneys could, however, have induced other confounding effects which I planned to avoid. To confirm protein signatures as pathognomonic biomarkers in the human setting requires further validation. The chosen CsA dosage was higher than in patients (trough levels 3040 ng/mL in rat vs. 100-600 ng/mL in humans), which potentially reduced its translational validity; yet, high CsA dosage in rats has been earlier established to safely induce nephrotoxicity, and is therefore inherent to the model. The levels resulted from applying approximately 30 mg CsA per kg/d by minipump, without giving additional low salt diet (LSD). Compared to published literature, these levels have commonly been used in rats or mice, and even much higher doses (up to 100 mg/kg/d) have been applied in the past, often enough in combination with LSD, to achieve

nephrotoxicity (Labes et al. 2022, Fasel et al; 1987). Human Tac trough levels commonly range between 5 and 15 ng/ml. In this study, rat Tac trough levels with 3.4 ng/mL were lower; this limitation had to be set for a species-specific reason, since Tac dose-dependently showed higher toxicity in the rat. The levels resulted from applying approximately 2 mg/kg/d Tac by minipump, without giving additional LSD. Compared to published literature these levels were commonly targeted in rats or mice (Andoh et al. 1996).

5. Conclusion

In summary, our findings provide insights into potential mechanisms underlying CNI nephropathy during early chronic phase. We observed distinct patterns of pathogenesis in renal compartments between CsA and Tac treatments. While both CNIs caused common effects such as fibrosis and atrophy, notable differences were observed in pathological detail with regard to the predominant impact on the filtration barrier in the Tac group as compared to the deterioration of the PCT in CsA group. Through selective probing and multiomics analysis, we identified relevant protein signatures specific to the renal microenvironments associated with each medication. These included disruptions in VEGF/VEGFR2 signalling primarily in Tac-treated kidneys, while cytotoxic UPR signalling and altered autophagic flux characterised CsA-treated kidneys. The products identified through multiomics analysis were further characterised as differential, potentially pathognomonic biomarkers. As an outlook, detecting these markers in patients using multiplexed technology may enable early diagnosis and prognosis of CNI nephrotoxicity, ultimately helping to prevent allograft failure. Our data provide useful information serving in the attempt to balance CNI administration in long-term maintenance immunosuppression and will be helpful in future designing of nephroprotective strategies aimed to minimize the harmful side effects.

References

Adler SH, Turka LA (2002) Immunotherapy as a means to induce transplantation tolerance. Current Opinion in Immunology 14(5):660–665. https://doi.org/10.1016/S0952-7915(02)00376-X

Akool E-S, Doller A, Babelova A, Tsalastra W, Moreth K, Schaefer L, Pfeilschifter J, Eberhardt W (2008) Molecular Mechanisms of TGFβ Receptor-Triggered Signaling Cascades Rapidly Induced by the Calcineurin Inhibitors Cyclosporin A and FK506. The Journal of Immunology 181(4):2831–2845. https://doi.org/10.4049/jimmunol.181.4.2831

Al-Bari MdAA, Xu P (2020) Molecular regulation of autophagy machinery by mTOR-dependent and -independent pathways. Ann NY Acad Sci 1467(1):3–20. https://doi.org/10.1111/nyas.14305

Allen TR, Krueger KD, Hunter WJ, Agrawal DK (2005) Evidence that insulin-like growth factor-1 requires protein kinase C-ε, PI3-kinase and mitogen-activated protein kinase pathways to protect human vascular smooth muscle cells from apoptosis. Immunol Cell Biol 83(6):651–667. https://doi.org/10.1111/j.1440-1711.2005.01387.x

Alpern RJ, Seldin DW, Giebisch G (eds) (2008) Seldin and Giebisch's the kidney: physiology and pathophysiology. Elsevier, Acad. Press, Amsterdam

Andoh TF, Burdmann EA, Fransechini N, Houghton DC, Bennett WM (1996) Comparison of acute rapamycin nephrotoxicity with cyclosporine and FK506. Kidney International 50(4):1110–1117. https://doi.org/10.1038/ki.1996.417

Ansermet C, Centeno G, Pradervand S, Harmacek D, Garcia A, Daraspe J, Kocherlakota S, Baes M, Bignon Y, Firsov D (2022) Renal tubular peroxisomes are dispensable for normal kidney function. JCI Insight 7(4):e155836. https://doi.org/10.1172/jci.insight.155836

Apelt K, Bijkerk R, Lebrin F, Rabelink TJ (2021) Imaging the Renal Microcirculation in Cell Therapy. Cells 10(5):1087. https://doi.org/10.3390/cells10051087

Arafa E, Bondzie PA, Rezazadeh K, Meyer RD, Hartsough E, Henderson JM, Schwartz JH, Chitalia V, Rahimi N (2015) TMIGD1 Is a Novel Adhesion Molecule That Protects Epithelial Cells from Oxidative Cell Injury. The American Journal of Pathology 185(10):2757–2767. https://doi.org/10.1016/j.ajpath.2015.06.006

Ares GR, Caceres PS, Ortiz PA (2011) Molecular regulation of NKCC2 in the thick ascending limb. American Journal of Physiology-Renal Physiology 301(6):F1143–F1159. https://doi.org/10.1152/ajprenal.00396.2011

Artelt N, Ludwig TA, Rogge H, Kavvadas P, Siegerist F, Blumenthal A, van den Brandt J, Otey CA, Bang M-L, Amann K, Chadjichristos CE, Chatziantoniou C, Endlich K, Endlich N (2018a) The Role of Palladin in Podocytes. JASN 29(6):1662–1678. https://doi.org/10.1681/ASN.2017091039

Artelt N, Siegerist F, Ritter AM, Grisk O, Schlüter R, Endlich K, Endlich N (2018b) Comparative Analysis of Podocyte Foot Process Morphology in Three Species by 3D Super-Resolution Microscopy. Front Med 5:292. https://doi.org/10.3389/fmed.2018.00292

Asfahani RI, Tahoun MM, Miller-Hodges EV, Bellerby J, Virasami AK, Sampson RD, Moulding D, Sebire NJ, Hohenstein P, Scambler PJ, Waters AM (2018) Activation of podocyte Notch mediates

early Wt1 glomerulopathy. Kidney International 93(4):903–920. https://doi.org/10.1016/j.kint.2017.11.014

Azzi JR, Sayegh MH, Mallat SG (2013) Calcineurin Inhibitors: 40 Years Later, Can't Live Without …. The Journal of Immunology 191(12):5785–5791. https://doi.org/10.4049/jimmunol.1390055

Bartlett CS, Jeansson M, Quaggin SE (2016) Vascular Growth Factors and Glomerular Disease. Annu Rev Physiol 78:437–461. https://doi.org/10.1146/annurev-physiol-021115-105412

Baylis C (2008) Nitric oxide deficiency in chronic kidney disease. American Journal of Physiology-Renal Physiology 294(1):F1–F9. https://doi.org/10.1152/ajprenal.00424.2007

Bentata Y (2020) Tacrolimus: 20 years of use in adult kidney transplantation. What we should know about its nephrotoxicity. Artif Organs 44(2):140–152. https://doi.org/10.1111/aor.13551

Benzing T (2004) Signaling at the Slit Diaphragm. Journal of the American Society of Nephrology 15(6):1382–1391. https://doi.org/10.1097/01.ASN.0000130167.30769.55

Bernhardt A, Fehr A, Brandt S, Jerchel S, Ballhause TM, Philipsen L, Stolze S, Geffers R, Weng H, Fischer K-D, Isermann B, Brunner-Weinzierl MC, Batra A, Siegmund B, Zhu C, Lindquist JA, Mertens PR (2017) Inflammatory cell infiltration and resolution of kidney inflammation is orchestrated by the cold-shock protein Y-box binding protein-1. Kidney International 92(5):1157–1177. https://doi.org/10.1016/j.kint.2017.03.035

Blaine J, Dylewski J (2020) Regulation of the Actin Cytoskeleton in Podocytes. Cells 9(7):1700. https://doi.org/10.3390/cells9071700

Borel JF, Feurer C, Gubler HU, Stähelin H (1976) Biological effects of cyclosporin A: A new antilymphocytic agent. Agents and Actions 6(4):468–475. https://doi.org/10.1007/BF01973261

Bouvier N, Flinois JP, Gilleron J, Sauvage F-L, Legendre C, Beaune P, Thervet E, Anglicheau D, Pallet N (2009) Cyclosporine triggers endoplasmic reticulum stress in endothelial cells: a role for endothelial phenotypic changes and death. American Journal of Physiology-Renal Physiology 296(1):F160–F169. https://doi.org/10.1152/ajprenal.90567.2008

Breier G, Albrecht U, Sterrer S, Risau W (1992) Expression of vascular endothelial growth factor during embryonic angiogenesis and endothelial cell differentiation. Development 114(2):521–532. https://doi.org/10.1242/dev.114.2.521

Breyer MD, Breyer RM (2000) Prostaglandin E receptors and the kidney. American Journal of Physiology-Renal Physiology 279(1):F12–F23. https://doi.org/10.1152/ajprenal.2000.279.1.F12

Calò LA, Ravarotto V, Simioni F, Naso E, Marchini F, Bonfante L, Furian L, Rigotti P (2017) Pathophysiology of Post Transplant Hypertension in Kidney Transplant: Focus on Calcineurin Inhibitors Induced Oxidative Stress and Renal Sodium Retention and Implications with RhoA/Rho Kinase Pathway. Kidney Blood Press Res 42(4):676–685. https://doi.org/10.1159/000483023

Castoldi G, Carletti R, Ippolito S, Colzani M, Barzaghi F, Stella A, Zerbini G, Perseghin G, Zatti G, di Gioia CRT (2021) Sodium-glucose cotransporter 2 inhibition prevents renal fibrosis in cyclosporine nephropathy. Acta Diabetol 58(8):1059–1070. https://doi.org/10.1007/s00592-021-01681-2

Cattaneo D, Perico N, Gaspari F, Remuzzi G (2004) Nephrotoxic aspects of cyclosporine. Transplantation Proceedings 36(2):S234–S239. https://doi.org/10.1016/j.transproceed.2004.01.011

Chapman JR (2011) Chronic Calcineurin Inhibitor Nephrotoxicity—Lest We Forget. American Journal of Transplantation 11(4):693–697. https://doi.org/10.1111/j.1600-6143.2011.03504.x

Charney DA, Bhaskaran M, Molmenti E (2009) Calcineurin inhibitor toxicity in a renal transplant recipient. Clinical Kidney Journal 2(2):175–176. https://doi.org/10.1093/ndtplus/sfp007

Charo IF, Taubman MB (2004) Chemokines in the Pathogenesis of Vascular Disease. Circulation Research 95(9):858–866. https://doi.org/10.1161/01.RES.0000146672.10582.17

Chen L, Clark JZ, Nelson JW, Kaissling B, Ellison DH, Knepper MA (2019a) Renal-Tubule Epithelial Cell Nomenclature for Single-Cell RNA-Sequencing Studies. J Am Soc Nephrol 30(8):1358–1364. https://doi.org/10.1681/ASN.2019040415

Chen X, Wu Y, Diao Z, Han X, Li D, Ruan X, Liu W (2019b) C1q/tumor necrosis factor-related protein-3 improves renal fibrosis via inhibiting notch signaling pathways. Journal Cellular Physiology 234(12):22352–22364. https://doi.org/10.1002/jcp.28801

Cheung K, Ma L, Wang G, Coe D, Ferro R, Falasca M, Buckley CD, Mauro C, Marelli-Berg FM (2015) CD31 signals confer immune privilege to the vascular endothelium. Proc Natl Acad Sci USA 112(43). https://doi.org/10.1073/pnas.1509627112

Chou Y-H, Chu T-S, Lin S-L (2018) Role of renin-angiotensin system in acute kidney injury-chronic kidney disease transition: Role of RAS system in AKI-CKD. Nephrology 23:121–125. https://doi.org/10.1111/nep.13467

Christians U, Braun F, Schmidt M, Kosian N, Schiebel HM, Ernst L, Winkler M, Kruse C, Linck A, Sewing KF (1992) Specific and sensitive measurement of FK506 and its metabolites in blood and urine of liver-graft recipients. Clin Chem 38(10):2025–2032

Cortinovis M, Perico N, Ruggenenti P, Remuzzi A, Remuzzi G (2022) Glomerular hyperfiltration. Nat Rev Nephrol 18(7):435–451. https://doi.org/10.1038/s41581-022-00559-y

Creamer TP (2020) Calcineurin. Cell Commun Signal 18(1):137. https://doi.org/10.1186/s12964-020-00636-4

Cui Y, Huang Q, Auman JT, Knight B, Jin X, Blanchard KT, Chou J, Jayadev S, Paules RS (2011) Genomic-Derived Markers for Early Detection of Calcineurin Inhibitor Immunosuppressant–Mediated Nephrotoxicity. Toxicological Sciences 124(1):23–34. https://doi.org/10.1093/toxsci/kfr217

Cybulsky AV (2017) Endoplasmic reticulum stress, the unfolded protein response and autophagy in kidney diseases. Nat Rev Nephrol 13(11):681–696. https://doi.org/10.1038/nrneph.2017.129

Ding L, Wang H, Lang W, Xiao L (2002) Protein Kinase C-ε Promotes Survival of Lung Cancer Cells by Suppressing Apoptosis through Dysregulation of the Mitochondrial Caspase Pathway. Journal of Biological Chemistry 277(38):35305–35313. https://doi.org/10.1074/jbc.M201460200

Dittmayer C, Goebel H-H, Heppner FL, Stenzel W, Bachmann S (2021) Preparation of Samples for Large-Scale Automated Electron Microscopy of Tissue and Cell Ultrastructure. Microsc Microanal 27(4):815–827. https://doi.org/10.1017/S1431927621011958

Dobrian AD (2012) ADMA and NOS regulation in chronic renal disease: beyond the old rivalry for l-arginine. Kidney International 81(8):722–724. https://doi.org/10.1038/ki.2011.496

Dong R, Xu Y (2022) Glomerular cell cross talk in diabetic kidney diseases. Journal of Diabetes 14(8):514–523. https://doi.org/10.1111/1753-0407.13304

Drenckhahn D, Franke RP (1988) Ultrastructural organization of contractile and cytoskeletal proteins in glomerular podocytes of chicken, rat, and man. Lab Invest 59(5):673–682

Dumas SJ, Meta E, Borri M, Luo Y, Li X, Rabelink TJ, Carmeliet P (2021) Phenotypic diversity and metabolic specialization of renal endothelial cells. Nat Rev Nephrol 17(7):441–464. https://doi.org/10.1038/s41581-021-00411-9

Ebefors K, Lassén E, Anandakrishnan N, Azeloglu EU, Daehn IS (2021) Modeling the Glomerular Filtration Barrier and Intercellular Crosstalk. Front Physiol 12:689083. https://doi.org/10.3389/fphys.2021.689083

Ebefors K, Wiener RJ, Yu L, Azeloglu EU, Yi Z, Jia F, Zhang W, Baron MH, He JC, Haraldsson B, Daehn I (2019) Endothelin receptor-A mediates degradation of the glomerular endothelial surface layer via pathologic crosstalk between activated podocytes and glomerular endothelial cells. Kidney International 96(4):957–970. https://doi.org/10.1016/j.kint.2019.05.007

Eckardt K-U, Coresh J, Devuyst O, Johnson RJ, Köttgen A, Levey AS, Levin A (2013) Evolving importance of kidney disease: from subspecialty to global health burden. The Lancet 382(9887):158–169. https://doi.org/10.1016/S0140-6736(13)60439-0

El-Houjeiri L, Possik E, Vijayaraghavan T, Paquette M, Martina JA, Kazan JM, Ma EH, Jones R, Blanchette P, Puertollano R, Pause A (2019) The Transcription Factors TFEB and TFE3 Link the FLCN-AMPK Signaling Axis to Innate Immune Response and Pathogen Resistance. Cell Reports 26(13):3613-3628.e6. https://doi.org/10.1016/j.celrep.2019.02.102

Eremina V, Cui S, Gerber H, Ferrara N, Haigh J, Nagy A, Ema M, Rossant J, Jothy S, Miner JH, Quaggin SE (2006) Vascular endothelial growth factor a signaling in the podocyte-endothelial compartment is required for mesangial cell migration and survival. J Am Soc Nephrol 17(3):724–735. https://doi.org/10.1681/ASN.2005080810

Eremina V, Sood M, Haigh J, Nagy A, Lajoie G, Ferrara N, Gerber H-P, Kikkawa Y, Miner JH, Quaggin SE (2003) Glomerular-specific alterations of VEGF-A expression lead to distinct congenital and acquired renal diseases. J Clin Invest 111(5):707–716. https://doi.org/10.1172/JCI17423

Farouk SS, Rein JL (2020) The Many Faces of Calcineurin Inhibitor Toxicity—What the FK? Advances in Chronic Kidney Disease 27(1):56–66. https://doi.org/10.1053/j.ackd.2019.08.006

Fasel J, Kaissling B, Ludwig KS, Ryffel B, Mihatsch MJ (1987) Light and Electron Microscopic Changes in the Kidney of Wistar Rats following Treatment with Cyclosporine A. Ultrastructural Pathology 11(4):435–448. https://doi.org/10.3109/01913128709048438

Fedele AO, Carraro V, Xie J, Averous J, Proud CG (2020) Cyclosporin A but not FK506 activates the integrated stress response in human cells. Journal of Biological Chemistry 295(44):15134–15143. https://doi.org/10.1074/jbc.RA120.014531

Fridén V, Oveland E, Tenstad O, Ebefors K, Nyström J, Nilsson UA, Haraldsson B (2011) The glomerular endothelial cell coat is essential for glomerular filtration. Kidney International 79(12):1322–1330. https://doi.org/10.1038/ki.2011.58

Fulton D, Gratton J-P, McCabe TJ, Fontana J, Fujio Y, Walsh K, Franke TF, Papapetropoulos A, Sessa WC (1999) Regulation of endothelium-derived nitric oxide production by the protein kinase Akt. Nature 399(6736):597–601. https://doi.org/10.1038/21218

Gallego MJ, Zoja C, Morigi M, Micheletti G, Imberti B, Foppolo M, Remuzzi A, Remuzzi G (1996) Cyclosporine enhances leukocyte adhesion to vascular endothelium under physiologic flow conditions. American Journal of Kidney Diseases 28(1):23–31. https://doi.org/10.1016/S0272-6386(96)90126-2

Garg P (2018) A Review of Podocyte Biology. Am J Nephrol 47(Suppl. 1):3–13. https://doi.org/10.1159/000481633

Godin N, Liu F, Lau GJ, Brezniceanu M-L, Chénier I, Filep JG, Ingelfinger JR, Zhang S-L, Chan JSD (2010) Catalase overexpression prevents hypertension and tubular apoptosis in angiotensinogen transgenic mice. Kidney International 77(12):1086–1097. https://doi.org/10.1038/ki.2010.63

Graef IA, Chen F, Chen L, Kuo A, Crabtree GR (2001) Signals Transduced by Ca2+/Calcineurin and NFATc3/c4 Pattern the Developing Vasculature. Cell 105(7):863–875. https://doi.org/10.1016/S0092-8674(01)00396-8

Gu P, Theiss A, Han J, Feagins LA (2017) Increased Cell Adhesion Molecules, PECAM-1, ICAM-3, or VCAM-1, Predict Increased Risk for Flare in Patients With Quiescent Inflammatory Bowel Disease. Journal of Clinical Gastroenterology 51(6):522–527. https://doi.org/10.1097/MCG.0000000000000618

Gu Y, Gong Y, Zhang H, Dong X, Zhao T, Burczynski FJ, Wang G, Sun S, Zhu B, Han W, Wang H, Li P (2013) Regulation of transforming growth factor beta 1 gene expression by dihydropteridine reductase in kidney 293T cells. Biochem Cell Biol 91(3):187–193. https://doi.org/10.1139/bcb-2012-0087

Guo J-K (2002) WT1 is a key regulator of podocyte function: reduced expression levels cause crescentic glomerulonephritis and mesangial sclerosis. Human Molecular Genetics 11(6):651–659. https://doi.org/10.1093/hmg/11.6.651

Han SW, Li C, Ahn KO, Lim SW, Song HG, Jang YS, Cho YM, Jang YM, Ghee JY, Kim JY, Kim SH, Kim J, Kwon OJ, Yang CW (2008) Prolonged Endoplasmic Reticulum Stress Induces Apoptotic Cell Death in an Experimental Model of Chronic Cyclosporine Nephropathy. Am J Nephrol 28(5):707–714. https://doi.org/10.1159/000127432

Hannemann J, Zummack J, Hillig J, Rendant-Gantzberg L, Böger R (2022) Association of Variability in the DDAH1, DDAH2, AGXT2 and PRMT1 Genes with Circulating ADMA Concentration in Human Whole Blood. JCM 11(4):941. https://doi.org/10.3390/jcm11040941

Haraldsson B, Nyström J (2012) The glomerular endothelium: new insights on function and structure. Current Opinion in Nephrology & Hypertension 21(3):258–263. https://doi.org/10.1097/MNH.0b013e3283522e7a

Hayashi A, Okamoto T, Nio-Kobayashi J, Iwahara N, Suzuki R, Ueda Y, Takahashi T, Yasuyuki SATO, Iwanaga T, Hotta K (2022) CD44 as a pathological marker for the early detection of calcineurin inhibitor-induced nephrotoxicity post kidney transplantation. Biomed Res 43(5):181–186. https://doi.org/10.2220/biomedres.43.181

Hetz C, Papa FR (2018) The Unfolded Protein Response and Cell Fate Control. Molecular Cell 69(2):169–181. https://doi.org/10.1016/j.molcel.2017.06.017

Higa A, Taouji S, Lhomond S, Jensen D, Fernandez-Zapico ME, Simpson JC, Pasquet J-M, Schekman R, Chevet E (2014) Endoplasmic Reticulum Stress-Activated Transcription Factor ATF6α Requires the Disulfide Isomerase PDIA5 To Modulate Chemoresistance. Mol Cell Biol 34(10):1839–1849. https://doi.org/10.1128/MCB.01484-13

Honda T, Hirakawa Y, Nangaku M (2019) The role of oxidative stress and hypoxia in renal disease. Kidney Res Clin Pract 38(4):414–426. https://doi.org/10.23876/j.krcp.19.063

Hošková L, Málek I, Kopkan L, Kautzner J (2017) Pathophysiological Mechanisms of Calcineurin Inhibitor-Induced Nephrotoxicity and Arterial Hypertension. Physiol Res :167–180. https://doi.org/10.33549/physiolres.933332

Hristovska A-M, Rasmussen LE, Hansen PBL, Nielsen SS, Nüsing RM, Narumiya S, Vanhoutte P, Skøtt O, Jensen BL (2007) Prostaglandin E $_2$ Induces Vascular Relaxation by E-Prostanoid 4 Receptor-Mediated Activation of Endothelial Nitric Oxide Synthase. Hypertension 50(3):525–530. https://doi.org/10.1161/HYPERTENSIONAHA.107.088948

Huber TB, Köttgen M, Schilling B, Walz G, Benzing T (2001) Interaction with Podocin Facilitates Nephrin Signaling. Journal of Biological Chemistry 276(45):41543–41546. https://doi.org/10.1074/jbc.C100452200

Ichimura K, Kurihara H, Sakai T (2003) Actin Filament Organization of Foot Processes in Rat Podocytes. J Histochem Cytochem 51(12):1589–1600. https://doi.org/10.1177/002215540305101203

Jeansson M, Haraldsson B (2006) Morphological and functional evidence for an important role of the endothelial cell glycocalyx in the glomerular barrier. American Journal of Physiology-Renal Physiology 290(1):F111–F116. https://doi.org/10.1152/ajprenal.00173.2005

Jeon SH, Piao YJ, Choi KJ, Hong F, Baek HW, Kang I, Ha J, Kim SS, Chang S-G (2005) Prednisolone suppresses cyclosporin A-induced apoptosis but not cell cycle arrest in MDCK cells. Archives of Biochemistry and Biophysics 435(2):382–392. https://doi.org/10.1016/j.abb.2005.01.003

Jorgensen KA, Koefoed-Nielsen PB, Karamperis N (2003) Calcineurin Phosphatase Activity and Immunosuppression. A Review on the Role of Calcineurin Phosphatase Activity and the Immunosuppressive Effect of Cyclosporin A and Tacrolimus. Scand J Immunol 57(2):93–98. https://doi.org/10.1046/j.1365-3083.2003.01221.x

Kaissling B, Le Hir M (2008) The renal cortical interstitium: morphological and functional aspects. Histochem Cell Biol 130(2):247–262. https://doi.org/10.1007/s00418-008-0452-5

Kapturczak MH, Meier-Kriesche HU, Kaplan B (2004) Pharmacology of calcineurin antagonists. Transplantation Proceedings 36(2):S25–S32. https://doi.org/10.1016/j.transproceed.2004.01.018

Karolin A, Escher G, Rudloff S, Sidler D (2022) Nephrotoxicity of Calcineurin Inhibitors in Kidney Epithelial Cells is Independent of NFAT Signaling. Front Pharmacol 12:789080. https://doi.org/10.3389/fphar.2021.789080

Khramova A, Boi R, Fridén V, Granqvist AB, Nilsson U, Tenstad O, Oveland E, Haraldsson B, Ebefors K, Nyström J (2021) Proteoglycans contribute to the functional integrity of the glomerular endothelial cell surface layer and are regulated in diabetic kidney disease. Sci Rep 11(1):8487. https://doi.org/10.1038/s41598-021-87753-3

Kidokoro K, Satoh M, Nagasu H, Sakuta T, Kuwabara A, Yorimitsu D, Nishi Y, Tomita N, Sasaki T, Kashihara N (2012) Tacrolimus Induces Glomerular Injury via Endothelial Dysfunction Caused by Reactive Oxygen Species and Inflammatory Change. Kidney Blood Press Res 35(6):549–557. https://doi.org/10.1159/000339494

Kim HW, Lim JH, Kim MY, Chung S, Shin SJ, Chung HW, Choi BS, Kim Y-S, Chang YS, Park CW (2011a) Long-term blockade of vascular endothelial growth factor receptor-2 aggravates the diabetic renal dysfunction associated with inactivation of the Akt/eNOS-NO axis. Nephrology Dialysis Transplantation 26(4):1173–1188. https://doi.org/10.1093/ndt/gfq610

Kim J, Kundu M, Viollet B, Guan K-L (2011b) AMPK and mTOR regulate autophagy through direct phosphorylation of Ulk1. Nat Cell Biol 13(2):132–141. https://doi.org/10.1038/ncb2152

Kim JH, Lee YH, Lim BJ, Jeong HJ, Kim PK, Shin JI (2016) Influence of cyclosporine A on glomerular growth and the effect of mizoribine and losartan on cyclosporine nephrotoxicity in young rats. Sci Rep 6(1):22374. https://doi.org/10.1038/srep22374

Kim YH, Goyal M, Kurnit D, Wharram B, Wiggins J, Holzman L, Kershaw D, Wiggins R (2001) Podocyte depletion and glomerulosclerosis have a direct relationship in the PAN-treated rat. Kidney International 60(3):957–968. https://doi.org/10.1046/j.1523-1755.2001.060003957.x

Kino T, Goto T (1993) Discovery of FK-506 and Update. Ann NY Acad Sci 685(1 Immunomodulat):13–21. https://doi.org/10.1111/j.1749-6632.1993.tb35846.x

Kirkin V, McEwan DG, Novak I, Dikic I (2009) A Role for Ubiquitin in Selective Autophagy. Molecular Cell 34(3):259–269. https://doi.org/10.1016/j.molcel.2009.04.026

Kitamura M (2010) Induction of the unfolded protein response by calcineurin inhibitors: a double-edged sword in renal transplantation. Nephrology Dialysis Transplantation 25(1):6–9. https://doi.org/10.1093/ndt/gfp516

Klawitter J, Klawitter J, Kushner E, Jonscher K, Bendrick-Peart J, Leibfritz D, Christians U, Schmitz V (2010) Association of Immunosuppressant-Induced Protein Changes in the Rat Kidney with Changes in Urine Metabolite Patterns: A Proteo-Metabonomic Study. J Proteome Res 9(2):865–875. https://doi.org/10.1021/pr900761m

Koch S, Claesson-Welsh L (2012) Signal transduction by vascular endothelial growth factor receptors. Cold Spring Harb Perspect Med 2(7):a006502. https://doi.org/10.1101/cshperspect.a006502

Kortenoeven MLA, Pedersen NB, Rosenbaek LL, Fenton RA (2015) Vasopressin regulation of sodium transport in the distal nephron and collecting duct. American Journal of Physiology-Renal Physiology 309(4):F280–F299. https://doi.org/10.1152/ajprenal.00093.2015

Kriz W, Kaissling B (2008) Structural Organization of the Mammalian Kidney. In: Seldin and Giebisch's The Kidney. Elsevier, pp 479–563

Kriz W, Lemley KV (2015) A potential role for mechanical forces in the detachment of podocytes and the progression of CKD. J Am Soc Nephrol 26(2):258–269. https://doi.org/10.1681/ASN.2014030278

Kriz W, Shirato I, Nagata M, LeHir M, Lemley KV (2013) The podocyte's response to stress: the enigma of foot process effacement. American Journal of Physiology-Renal Physiology 304(4):F333–F347. https://doi.org/10.1152/ajprenal.00478.2012

Kuppe C, Gröne H-J, Ostendorf T, van Kuppevelt TH, Boor P, Floege J, Smeets B, Moeller MJ (2015) Common histological patterns in glomerular epithelial cells in secondary focal segmental glomerulosclerosis. Kidney International 88(5):990–998. https://doi.org/10.1038/ki.2015.116

Kurtz A, Bruna RD, Kühn K (1988) Cyclosporine A enhances renin secretion and production in isolated juxtaglomerular cells. Kidney International 33(5):947–953. https://doi.org/10.1038/ki.1988.92

Labes R, Brinkmann L, Kulow VA, Roegner K, Mathia S, Balcerek B, Persson PB, Rosenberger C, Fähling M (2022) Daprodustat prevents cyclosporine-A–mediated anemia and peritubular capillary loss. Kidney International 102(4):750–765. https://doi.org/10.1016/j.kint.2022.04.025

Lamas S (2005) Cellular mechanisms of vascular injury mediated by calcineurin inhibitors. Kidney International 68(2):898–907. https://doi.org/10.1111/j.1523-1755.2005.00472.x

Lassila M (2002) Interaction of Cyclosporine A and the Renin-Angiotensin System New Perspectives. CDM 3(1):61–71. https://doi.org/10.2174/1389200023337964

Lassiter R, Merchen TD, Fang X, Wang Y (2021) Protective Role of Kynurenine 3-Monooxygenase in Allograft Rejection and Tubular Injury in Kidney Transplantation. Front Immunol 12:671025. https://doi.org/10.3389/fimmu.2021.671025

Lee JW, Chou C-L, Knepper MA (2015) Deep Sequencing in Microdissected Renal Tubules Identifies Nephron Segment-Specific Transcriptomes. J Am Soc Nephrol 26(11):2669–2677. https://doi.org/10.1681/ASN.2014111067

Leiper JM, Santa Maria J, Chubb A, MacAllister RJ, Charles IG, Whitley GS, Vallance P (1999) Identification of two human dimethylarginine dimethylaminohydrolases with distinct tissue distributions and homology with microbial arginine deiminases. Biochem J 343 Pt 1(Pt 1):209–214

Leone A, Moncada S, Vallance P, Calver A, Collier J (1992) Accumulation of an endogenous inhibitor of nitric oxide synthesis in chronic renal failure. The Lancet 339(8793):572–575. https://doi.org/10.1016/0140-6736(92)90865-Z

Li X, Liu C, Yang A, Shen Y, Xu J, Zuo D (2022) Role of HAO2 in rats with chronic kidney disease by regulating fatty acid metabolic processes in renal tissue. Cancer Biology

Li Z, An N, Huang X, Yang C, Wu H, Chen X, Pan Q, Liu H (2021) Cyclosporine A blocks autophagic flux in tubular epithelial cells by impairing TFEB-mediated lysosomal function. J Cell Mol Med 25(12):5729–5743. https://doi.org/10.1111/jcmm.16593

Lim BJ, Yang JW, Do WS, Fogo AB (2016) Pathogenesis of Focal Segmental Glomerulosclerosis. J Pathol Transl Med 50(6):405–410. https://doi.org/10.4132/jptm.2016.09.21

Liptak P, Ivanyi B (2006) Primer: histopathology of calcineurin-inhibitor toxicity in renal allografts. Nat Rev Nephrol 2(7):398–404. https://doi.org/10.1038/ncpneph0225

Marieb EN, Brady P, Mallatt J (2020) Human anatomy, Ninth edition. Pearson Education, Inc, New Jersey

Martina JA, Chen Y, Gucek M, Puertollano R (2012) MTORC1 functions as a transcriptional regulator of autophagy by preventing nuclear transport of TFEB. Autophagy 8(6):903–914. https://doi.org/10.4161/auto.19653

Martina JA, Diab HI, Brady OA, Puertollano R (2016a) TFEB and TFE 3 are novel components of the integrated stress response. EMBO J 35(5):479–495. https://doi.org/10.15252/embj.201593428

Martina JA, Diab HI, Brady OA, Puertollano R (2016b) TFEB and TFE 3 are novel components of the integrated stress response. The EMBO Journal 35(5):479–495. https://doi.org/10.15252/embj.201593428

Martinez-Martinez S, Redondo J (2004) Inhibitors of the Calcineurin / NFAT Pathway. CMC 11(8):997–1007. https://doi.org/10.2174/0929867043455576

Matsumoto Y, Ueda S, Yamagishi S, Matsuguma K, Shibata R, Fukami K, Matsuoka H, Imaizumi T, Okuda S (2007) Dimethylarginine Dimethylaminohydrolase Prevents Progression of Renal Dysfunction by Inhibiting Loss of Peritubular Capillaries and Tubulointerstitial Fibrosis in a Rat Model of Chronic Kidney Disease. Journal of the American Society of Nephrology 18(5):1525–1533. https://doi.org/10.1681/ASN.2006070696

Medina DL, Fraldi A, Bouche V, Annunziata F, Mansueto G, Spampanato C, Puri C, Pignata A, Martina JA, Sardiello M, Palmieri M, Polishchuk R, Puertollano R, Ballabio A (2011) Transcriptional Activation of Lysosomal Exocytosis Promotes Cellular Clearance. Developmental Cell 21(3):421–430. https://doi.org/10.1016/j.devcel.2011.07.016

Medyouf H, Ghysdael J (2008) The calcineurin/NFAT signaling pathway: A NOVEL therapeutic target in leukemia and solid tumors. Cell Cycle 7(3):297–303. https://doi.org/10.4161/cc.7.3.5357

Menon R, Otto EA, Berthier CC, Nair V, Farkash EA, Hodgin JB, Yang Y, Luo J, Woodside KJ, Zamani H, Norman SP, Wiggins RC, Kretzler M, Naik AS (2022) Glomerular endothelial cell-podocyte stresses and crosstalk in structurally normal kidney transplants. Kidney International 101(4):779–792. https://doi.org/10.1016/j.kint.2021.11.031

Merrill JP (1956) SUCCESSFUL HOMOTRANSPLANTATION OF THE HUMAN KIDNEY BETWEEN IDENTICAL TWINS. JAMA 160(4):277. https://doi.org/10.1001/jama.1956.02960390027008

Mertins P, Mani DR, Ruggles KV, Gillette MA, Clauser KR, Wang P, Wang X, Qiao JW, Cao S, Petralia F, Kawaler E, Mundt F, Krug K, Tu Z, Lei JT, Gatza ML, Wilkerson M, Perou CM, Yellapantula V, Huang K, Lin C, McLellan MD, Yan P, Davies SR, Townsend RR, Skates SJ, Wang J, Zhang B, Kinsinger CR, Mesri M, Rodriguez H, Ding L, Paulovich AG, Fenyö D, Ellis MJ, Carr SA, NCI CPTAC (2016) Proteogenomics connects somatic mutations to signalling in breast cancer. Nature 534(7605):55–62. https://doi.org/10.1038/nature18003

Mescher AL (2021) Junqueira's basic histology: text and atlas, 16th ed. McGraw-Hill, New York

Mihatsch MJ, Kyo M, Morozumi K, Yamaguchi Y, Nickeleit V, Ryffel B (1998) The side-effects of ciclosporine-A and tacrolimus. Clin Nephrol 49(6):356–363

Mizushima N, Klionsky DJ (2007) Protein Turnover Via Autophagy: Implications for Metabolism. Annu Rev Nutr 27(1):19–40. https://doi.org/10.1146/annurev.nutr.27.061406.093749

Mohamed T, Sequeira-Lopez MLS (2019) Development of the renal vasculature. Seminars in Cell & Developmental Biology 91:132–146. https://doi.org/10.1016/j.semcdb.2018.06.001

Morozumi K, Takeda A, Uchida K, Mihatsch MJ (2004) Cyclosporine nephrotoxicity: how does it affect renal allograft function and transplant morphology? Transplantation Proceedings 36(2):S251–S256. https://doi.org/10.1016/j.transproceed.2004.01.027

Mortensen LA, Bistrup C, Thiesson HC (2017) Does Mineralocorticoid Receptor Antagonism Prevent Calcineurin Inhibitor-Induced Nephrotoxicity? Front Med 4:210. https://doi.org/10.3389/fmed.2017.00210

Müller T, Kalxdorf M, Longuespée R, Kazdal DN, Stenzinger A, Krijgsveld J (2020) Automated sample preparation with SP 3 for low-input clinical proteomics. Mol Syst Biol 16(1). https://doi.org/10.15252/msb.20199111

Naesens M, Kuypers DRJ, Sarwal M (2009a) Calcineurin Inhibitor Nephrotoxicity. Clinical Journal of the American Society of Nephrology 4(2):481–508. https://doi.org/10.2215/CJN.04800908

Naesens M, Lerut E, Sarwal M, Van Damme B, Vanrenterghem Y, Kuypers DRJ (2009b) Balancing Efficacy and Toxicity of Kidney Transplant Immunosuppression. Transplantation Proceedings 41(8):3393–3395. https://doi.org/10.1016/j.transproceed.2009.09.017

Nagao RJ, Marcu R, Shin YJ, Lih D, Xue J, Arang N, Wei L, Akilesh S, Kaushansky A, Himmelfarb J, Zheng Y (2022) Cyclosporine Induces Fenestra-Associated Injury in Human Renal Microvessels *In Vitro*. ACS Biomater Sci Eng 8(1):196–207. https://doi.org/10.1021/acsbiomaterials.1c00986

Nakayama T, Sato W, Kosugi T, Zhang L, Campbell-Thompson M, Yoshimura A, Croker BP, Johnson RJ, Nakagawa T (2009) Endothelial injury due to eNOS deficiency accelerates the progression of chronic renal disease in the mouse. American Journal of Physiology-Renal Physiology 296(2):F317–F327. https://doi.org/10.1152/ajprenal.90450.2008

Nankivell BJ, P'Ng CH, O'Connell PJ, Chapman JR (2016) Calcineurin Inhibitor Nephrotoxicity Through the Lens of Longitudinal Histology: Comparison of Cyclosporine and Tacrolimus Eras. Transplantation 100(8):1723–1731. https://doi.org/10.1097/TP.0000000000001243

Nishiyama A, Kobori H, Fukui T, Zhang G-X, Yao L, Rahman M, Hitomi H, Kiyomoto H, Shokoji T, Kimura S, Kohno M, Abe Y (2003) Role of Angiotensin II and Reactive Oxygen Species in Cyclosporine A–Dependent Hypertension. Hypertension 42(4):754–760. https://doi.org/10.1161/01.HYP.0000085195.38870.44

Otsuka S, Melis N, Gaida MM, Dutta D, Weigert R, Ashwell JD (2021) Calcineurin inhibitors suppress acute graft-versus-host disease via NFAT-independent inhibition of T cell receptor signaling. Journal of Clinical Investigation 131(11):e147683. https://doi.org/10.1172/JCI147683

Pallet N, Bouvier N, Bendjallabah A, Rabant M, Flinois JP, Hertig A, Legendre C, Beaune P, Thervet E, Anglicheau D (2008a) Cyclosporine-Induced Endoplasmic Reticulum Stress Triggers Tubular Phenotypic Changes and Death. American Journal of Transplantation 8(11):2283–2296. https://doi.org/10.1111/j.1600-6143.2008.02396.x

Pallet N, Bouvier N, Legendre C, Gilleron J, Codogno P, Beaune P, Thervet E, Anglicheau D (2008b) Autophagy protects renal tubular cells against cyclosporine toxicity. Autophagy 4(6):783–791. https://doi.org/10.4161/auto.6477

Pallet N, Djamali A, Legendre C (2011) Challenges in diagnosing acute calcineurin-inhibitor induced nephrotoxicity: From toxicogenomics to emerging biomarkers. Pharmacological Research 64(1):25–30. https://doi.org/10.1016/j.phrs.2011.03.013

Pallet N, Rabant M, Xu-Dubois Y-C, LeCorre D, Mucchielli M-H, Imbeaud S, Agier N, Hertig A, Thervet E, Legendre C (2008c) Response of human renal tubular cells to cyclosporine and sirolimus: A

toxicogenomic study. Toxicology and Applied Pharmacology 229(2):184–196. https://doi.org/10.1016/j.taap.2008.01.019

Pallone TL, Edwards A, Mattson DL (2012) Renal medullary circulation. Compr Physiol 2(1):97–140. https://doi.org/10.1002/cphy.c100036

Paquette M, El-Houjeiri L, C. Zirden L, Puustinen P, Blanchette P, Jeong H, Dejgaard K, Siegel PM, Pause A (2021) AMPK-dependent phosphorylation is required for transcriptional activation of TFEB and TFE3. Autophagy 17(12):3957–3975. https://doi.org/10.1080/15548627.2021.1898748

Park S, DiMaio TA, Scheef EA, Sorenson CM, Sheibani N (2010) PECAM-1 regulates proangiogenic properties of endothelial cells through modulation of cell-cell and cell-matrix interactions. American Journal of Physiology-Cell Physiology 299(6):C1468–C1484. https://doi.org/10.1152/ajpcell.00246.2010

Patel SR, Dressler GR (2013) The genetics and epigenetics of kidney development. Semin Nephrol 33(4):314–326. https://doi.org/10.1016/j.semnephrol.2013.05.004

Pavenstädt H, Kriz W, Kretzler M (2003) Cell Biology of the Glomerular Podocyte. Physiological Reviews 83(1):253–307. https://doi.org/10.1152/physrev.00020.2002

Pearce D, Soundararajan R, Trimpert C, Kashlan OB, Deen PMT, Kohan DE (2015) Collecting Duct Principal Cell Transport Processes and Their Regulation. Clinical Journal of the American Society of Nephrology 10(1):135–146. https://doi.org/10.2215/CJN.05760513

Perera RM, Zoncu R (2016) The Lysosome as a Regulatory Hub. Annu Rev Cell Dev Biol 32(1):223–253. https://doi.org/10.1146/annurev-cellbio-111315-125125

Perico N, Detcheva A, Khalil EI, Remuzzi G (1996) Cyclosporine induces glomerulosclerosis: Three-dimensional definition of the lesions in a rat model of renal transplant. Kidney International 49(5):1283–1288. https://doi.org/10.1038/ki.1996.183

Perico N, Remuzzi A, Imberti O, Cavallotti D, Bertani T, Remuzzi G (1991) Morphometrical Analysis of Glomerular Changes Induced by Cyclosporine in the Rat. American Journal of Kidney Diseases 17(5):537–543. https://doi.org/10.1016/S0272-6386(12)80495-1

Quaggin SE, Kreidberg JA (2008) Development of the renal glomerulus: good neighbors and good fences. Development 135(4):609–620. https://doi.org/10.1242/dev.001081

Rabelink TJ, de Zeeuw D (2015) The glycocalyx—linking albuminuria with renal and cardiovascular disease. Nat Rev Nephrol 11(11):667–676. https://doi.org/10.1038/nrneph.2015.162

Rao R, Bhalla V, Pastor-Soler NM (2019) Intercalated Cells of the Kidney Collecting Duct in Kidney Physiology. Semin Nephrol 39(4):353–367. https://doi.org/10.1016/j.semnephrol.2019.04.005

Rashid H-O, Yadav RK, Kim H-R, Chae H-J (2015) ER stress: Autophagy induction, inhibition and selection. Autophagy 11(11):1956–1977. https://doi.org/10.1080/15548627.2015.1091141

Rask-Madsen C, King GL (2008) Differential Regulation of VEGF Signaling by PKC-α and PKC-ε in Endothelial Cells. ATVB 28(5):919–924. https://doi.org/10.1161/ATVBAHA.108.162842

Reidy KJ, Villegas G, Teichman J, Veron D, Shen W, Jimenez J, Thomas D, Tufro A (2009) Semaphorin3a regulates endothelial cell number and podocyte differentiation during glomerular development. Development 136(23):3979–3989. https://doi.org/10.1242/dev.037267

Ren H, Zhai W, Lu X, Wang G (2021) The Cross-Links of Endoplasmic Reticulum Stress, Autophagy, and Neurodegeneration in Parkinson's Disease. Front Aging Neurosci 13:691881. https://doi.org/10.3389/fnagi.2021.691881

Robert B, Zhao X, Abrahamson DR (2000) Coexpression of neuropilin-1, Flk1, and VEGF $_{164}$ in developing and mature mouse kidney glomeruli. American Journal of Physiology-Renal Physiology 279(2):F275–F282. https://doi.org/10.1152/ajprenal.2000.279.2.F275

Roberts WG, Palade GE (1995) Increased microvascular permeability and endothelial fenestration induced by vascular endothelial growth factor. Journal of Cell Science 108(6):2369–2379. https://doi.org/10.1242/jcs.108.6.2369

Rodrigues-Diez R, González-Guerrero C, Ocaña-Salceda C, Rodrigues-Diez RR, Egido J, Ortiz A, Ruiz-Ortega M, Ramos AM (2016) Calcineurin inhibitors cyclosporine A and tacrolimus induce vascular inflammation and endothelial activation through TLR4 signaling. Sci Rep 6(1):27915. https://doi.org/10.1038/srep27915

Rusnak F, Mertz P (2000) Calcineurin: Form and Function. Physiological Reviews 80(4):1483–1521. https://doi.org/10.1152/physrev.2000.80.4.1483

Salmon AH, Satchell SC (2012) Endothelial glycocalyx dysfunction in disease: albuminuria and increased microvascular permeability: Glycocalyx and microvascular permeability. J Pathol 226(4):562–574. https://doi.org/10.1002/path.3964

Sardiello M, Palmieri M, di Ronza A, Medina DL, Valenza M, Gennarino VA, Di Malta C, Donaudy F, Embrione V, Polishchuk RS, Banfi S, Parenti G, Cattaneo E, Ballabio A (2009) A Gene Network Regulating Lysosomal Biogenesis and Function. Science 325(5939):473–477. https://doi.org/10.1126/science.1174447

Sarró E, Jacobs-Cachá C, Itarte E, Meseguer A (2012) A pharmacologically-based array to identify targets of cyclosporine A-induced toxicity in cultured renal proximal tubule cells. Toxicology and Applied Pharmacology 258(2):275–287. https://doi.org/10.1016/j.taap.2011.11.007

Satchell SC, Braet F (2009) Glomerular endothelial cell fenestrations: an integral component of the glomerular filtration barrier. American Journal of Physiology-Renal Physiology 296(5):F947–F956. https://doi.org/10.1152/ajprenal.90601.2008

Satchell SC, Tasman CH, Singh A, Ni L, Geelen J, von Ruhland CJ, O'Hare MJ, Saleem MA, van den Heuvel LP, Mathieson PW (2006a) Conditionally immortalized human glomerular endothelial cells expressing fenestrations in response to VEGF. Kidney International 69(9):1633–1640. https://doi.org/10.1038/sj.ki.5000277

Satchell SC, Tasman CH, Singh A, Ni L, Geelen J, von Ruhland CJ, O'Hare MJ, Saleem MA, van den Heuvel LP, Mathieson PW (2006b) Conditionally immortalized human glomerular endothelial cells expressing fenestrations in response to VEGF. Kidney International 69(9):1633–1640. https://doi.org/10.1038/sj.ki.5000277

Schlöndorff D, Wyatt CM, Campbell KN (2017) Revisiting the determinants of the glomerular filtration barrier: what goes round must come round. Kidney International 92(3):533–536. https://doi.org/10.1016/j.kint.2017.06.003

Scott RP, Quaggin SE (2015) The cell biology of renal filtration. Journal of Cell Biology 209(2):199–210. https://doi.org/10.1083/jcb.201410017

Settembre C, Di Malta C, Polito VA, Arencibia MG, Vetrini F, Erdin S, Erdin SU, Huynh T, Medina D, Colella P, Sardiello M, Rubinsztein DC, Ballabio A (2011) TFEB Links Autophagy to Lysosomal Biogenesis. Science 332(6036):1429–1433. https://doi.org/10.1126/science.1204592

Shihab FS, Yi H, Bennett WM, Andoh TF (2000) Effect of nitric oxide modulation on TGF-β1 and matrix proteins in chronic cyclosporine nephrotoxicity. Kidney International 58(3):1174–1185. https://doi.org/10.1046/j.1523-1755.2000.00273.x

Sibal L, C Agarwal S, D Home P, H Boger R (2010) The Role of Asymmetric Dimethylarginine (ADMA) in Endothelial Dysfunction and Cardiovascular Disease. CCR 6(2):82–90. https://doi.org/10.2174/157340310791162659

Siegerist F, Ribback S, Dombrowski F, Amann K, Zimmermann U, Endlich K, Endlich N (2017) Structured illumination microscopy and automatized image processing as a rapid diagnostic tool for podocyte effacement. Sci Rep 7(1):11473. https://doi.org/10.1038/s41598-017-11553-x

Skorecki K, Chertow GM, Marsden PA, Taal MW, Yu ASL (eds) (2016) Brenner & Rector's the kidney, 10th edition. Elsevier, Philadelphia, PA

Sluiter TJ, van Buul JD, Huveneers S, Quax PHA, de Vries MR (2021) Endothelial Barrier Function and Leukocyte Transmigration in Atherosclerosis. Biomedicines 9(4):328. https://doi.org/10.3390/biomedicines9040328

Sol M, Kamps JAAM, van den Born J, van den Heuvel MC, van der Vlag J, Krenning G, Hillebrands J-L (2020) Glomerular Endothelial Cells as Instigators of Glomerular Sclerotic Diseases. Front Pharmacol 11:573557. https://doi.org/10.3389/fphar.2020.573557

Sonveaux P, Martinive P, DeWever J, Batova Z, Daneau G, Pelat M, Ghisdal P, Grégoire V, Dessy C, Balligand J-L, Feron O (2004) Caveolin-1 Expression Is Critical for Vascular Endothelial Growth Factor–Induced Ischemic Hindlimb Collateralization and Nitric Oxide–Mediated Angiogenesis. Circulation Research 95(2):154–161. https://doi.org/10.1161/01.RES.0000136344.27825.72

Stillman IE, Andoh TF, Burdmann EA, Bennett WM, Rosen S (1995) FK506 nephrotoxicity: morphologic and physiologic characterization of a rat model. Lab Invest 73(6):794–803

Subramanya AR, Ellison DH (2014) Distal convoluted tubule. Clin J Am Soc Nephrol 9(12):2147–2163. https://doi.org/10.2215/CJN.05920613

Suleiman HY, Roth R, Jain S, Heuser JE, Shaw AS, Miner JH (2017) Injury-induced actin cytoskeleton reorganization in podocytes revealed by super-resolution microscopy. JCI Insight 2(16):e94137. https://doi.org/10.1172/jci.insight.94137

Suthanthiran M, Strom TB (1994) Renal Transplantation. N Engl J Med 331(6):365–376. https://doi.org/10.1056/NEJM199408113310606

Tahir SA, Park S, Thompson TC (2009) Caveolin-1 regulates VEGF-stimulated angiogenic activities in prostate cancer and endothelial cells. Cancer Biology & Therapy 8(23):2284–2294. https://doi.org/10.4161/cbt.8.23.10138

Tamayo-Gutierrez A, Ibrahim HN (2022) The Kidney in Heart Failure: The Role of Venous Congestion. Methodist Debakey Cardiovasc J 18(4):4–10. https://doi.org/10.14797/mdcvj.1121

Taylor AL, Watson CJE, Bradley JA (2005) Immunosuppressive agents in solid organ transplantation: Mechanisms of action and therapeutic efficacy. Critical Reviews in Oncology/Hematology 56(1):23–46. https://doi.org/10.1016/j.critrevonc.2005.03.012

Tonelli M, Wiebe N, Knoll G, Bello A, Browne S, Jadhav D, Klarenbach S, Gill J (2011) Systematic Review: Kidney Transplantation Compared With Dialysis in Clinically Relevant Outcomes. American Journal of Transplantation 11(10):2093–2109. https://doi.org/10.1111/j.1600-6143.2011.03686.x

Tossidou I, Teng B, Worthmann K, Müller-Deile J, Jobst-Schwan T, Kardinal C, Schroder P, Bolanos-Palmieri P, Haller H, Willerding J, Drost DM, de Jonge L, Reubold T, Eschenburg S, Johnson RI, Schiffer M (2019) Tyrosine Phosphorylation of CD2AP Affects Stability of the Slit Diaphragm Complex. JASN 30(7):1220–1237. https://doi.org/10.1681/ASN.2018080860

Treuting PM, Dintzis SM, Montine KS (eds) (2018) Comparative anatomy and histology: a mouse, rat, and human atlas, Second edition. Academic Press, London San Diego Cambridge, MA Kidlington

Uciechowska-Kaczmarzyk U, Babik S, Zsila F, Bojarski KK, Beke-Somfai T, Samsonov SA (2018) Molecular dynamics-based model of VEGF-A and its heparin interactions. Journal of Molecular Graphics and Modelling 82:157–166. https://doi.org/10.1016/j.jmgm.2018.04.015

Ume AC, Wenegieme T-Y, Williams CR (2021) Calcineurin inhibitors: a double-edged sword. American Journal of Physiology-Renal Physiology 320(3):F336–F341. https://doi.org/10.1152/ajprenal.00262.2020

Unnersjö-Jess D, Ramdedovic A, Höhne M, Butt L, Koehler FC, Müller R-U, Hoyer PF, Blom H, Schermer B, Benzing T (2022) Three-Dimensional Super-Resolved Imaging of Paraffin-Embedded Kidney Samples. Kidney360 3(3):446–454. https://doi.org/10.34067/KID.0005882021

Vallance P, Leiper J (2005) Asymmetric Dimethylarginine and Kidney Disease—Marker or Mediator? Journal of the American Society of Nephrology 16(8):2254–2256. https://doi.org/10.1681/ASN.2005050539

Vallance P, Leone A, Calver A, Collier J, Moncada S (1992) Accumulation of an endogenous inhibitor of nitric oxide synthesis in chronic renal failure. Lancet 339(8793):572–575. https://doi.org/10.1016/0140-6736(92)90865-z

Vallés PG, Manucha W, Carrizo L, Vega Perugorria J, Seltzer A, Ruete C (2007) Renal caveolin-1 expression in children with unilateral ureteropelvic junction obstruction. Pediatr Nephrol 22(2):237–248. https://doi.org/10.1007/s00467-006-0290-4

Vallon V, Komers R (2011) Pathophysiology of the diabetic kidney. Compr Physiol 1(3):1175–1232. https://doi.org/10.1002/cphy.c100049

Vassiliadis J, Bracken C, Matthews D, O'Brien S, Schiavi S, Wawersik S (2011) Calcium Mediates Glomerular Filtration through Calcineurin and mTORC2/Akt Signaling. Journal of the American Society of Nephrology 22(8):1453–1461. https://doi.org/10.1681/ASN.2010080878

Veron D, Bertuccio CA, Marlier A, Reidy K, Garcia AM, Jimenez J, Velazquez H, Kashgarian M, Moeckel GW, Tufro A (2011) Podocyte vascular endothelial growth factor (Vegf$_{164}$) overexpression causes severe nodular glomerulosclerosis in a mouse model of type 1 diabetes. Diabetologia 54(5):1227–1241. https://doi.org/10.1007/s00125-010-2034-z

Wagner N, Wagner K-D, Xing Y, Scholz H, Schedl A (2004) The Major Podocyte Protein Nephrin Is Transcriptionally Activated by the Wilms' Tumor Suppressor WT1. Journal of the American Society of Nephrology 15(12):3044–3051. https://doi.org/10.1097/01.ASN.0000146687.99058.25

Wang H, Riha GM, Yan S, Li M, Chai H, Yang H, Yao Q, Chen C (2005) Shear Stress Induces Endothelial Differentiation From a Murine Embryonic Mesenchymal Progenitor Cell Line. ATVB 25(9):1817–1823. https://doi.org/10.1161/01.ATV.0000175840.90510.a8

Wang X, Jiang S, Fei L, Dong F, Xie L, Qiu X, Lei Y, Guo J, Zhong M, Ren X, Yang Y, Zhao L, Zhang G, Wang H, Tang C, Yu L, Liu R, Patzak A, Persson PB, Hultström M, Wei Q, Lai EY, Zheng Z (2022) Tacrolimus Causes Hypertension by Increasing Vascular Contractility via RhoA (Ras Homolog Family Member A)/ROCK (Rho-Associated Protein Kinase) Pathway in Mice. Hypertension 79(10):2228–2238. https://doi.org/10.1161/HYPERTENSIONAHA.122.19189

Wang Y, Hoeppner LH, Angom RS, Wang E, Dutta S, Doeppler HR, Wang F, Shen T, Scarisbrick IA, Guha S, Storz P, Bhattacharya R, Mukhopadhyay D (2019) Protein kinase D up-regulates transcription of VEGF receptor-2 in endothelial cells by suppressing nuclear localization of the transcription factor AP2β. Journal of Biological Chemistry 294(43):15759–15767. https://doi.org/10.1074/jbc.RA119.010152

Williams D, Haragsim L (2006) Calcineurin Nephrotoxicity. Advances in Chronic Kidney Disease 13(1):47–55. https://doi.org/10.1053/j.ackd.2005.11.001

Wu P-H, Onodera Y, Giaccia AJ, Le Q-T, Shimizu S, Shirato H, Nam J-M (2020) Lysosomal trafficking mediated by Arl8b and BORC promotes invasion of cancer cells that survive radiation. Commun Biol 3(1):620. https://doi.org/10.1038/s42003-020-01339-9

Xu C, Chang A, Hack BK, Eadon MT, Alper SL, Cunningham PN (2014) TNF-mediated damage to glomerular endothelium is an important determinant of acute kidney injury in sepsis. Kidney International 85(1):72–81. https://doi.org/10.1038/ki.2013.286

Xu H, Ren D (2015) Lysosomal Physiology. Annu Rev Physiol 77(1):57–80. https://doi.org/10.1146/annurev-physiol-021014-071649

Yilmaz DE, Kirschner K, Demirci H, Himmerkus N, Bachmann S, Mutig K (2022a) Immunosuppressive calcineurin inhibitor cyclosporine A induces proapoptotic endoplasmic reticulum stress in renal tubular cells. Journal of Biological Chemistry 298(3):101589. https://doi.org/10.1016/j.jbc.2022.101589

Yilmaz DE, Kirschner K, Demirci H, Himmerkus N, Bachmann S, Mutig K (2022b) Immunosuppressive calcineurin inhibitor cyclosporine A induces proapoptotic endoplasmic reticulum stress in renal tubular cells. Journal of Biological Chemistry 298(3):101589. https://doi.org/10.1016/j.jbc.2022.101589

Young BA, Burdmann EA, Johnson RJ, Andoh T, Bennett WM, Couser WG, Alpers CE (1995) Cyclosporine A induced arteriolopathy in a rat model of chronic cyclosporine nephropathy. Kidney International 48(2):431–438. https://doi.org/10.1038/ki.1995.311

Yuan L-Q, Wang C, Lu D-F, Zhao X-D, Tan L-H, Chen X (2020) Induction of apoptosis and ferroptosis by a tumor suppressing magnetic field through ROS-mediated DNA damage. Aging 12(4):3662–3681. https://doi.org/10.18632/aging.102836

Zhang W, Li X, Wang S, Chen Y, Liu H (2020) Regulation of TFEB activity and its potential as a therapeutic target against kidney diseases. Cell Death Discov 6(1):32. https://doi.org/10.1038/s41420-020-0265-4

Zheng S, Epstein PN (2021) CD45 Immunohistochemistry in Mouse Kidney. Bio Protoc 11(22):e4230. https://doi.org/10.21769/BioProtoc.4230

Zmijewska AA, Zmijewski JW, Becker Jr. EJ, Benavides GA, Darley-Usmar V, Mannon RB (2021) Bioenergetic maladaptation and release of HMGB1 in calcineurin inhibitor-mediated nephrotoxicity. American Journal of Transplantation 21(9):2964–2977. https://doi.org/10.1111/ajt.16561

Zoccali C, Bode-Böger SM, Mallamaci F, Benedetto FA, Tripepi G, Malatino LS, Cataliotti A, Bellanuova I, Fermo I, Frölich JC, Böger RH (2001) Plasma concentration of asymmetrical dimethylarginine and mortality in patients with end-stage renal disease: a prospective study. The Lancet 358(9299):2113–2117. https://doi.org/10.1016/S0140-6736(01)07217-8

Statutory declaration

"I, Hasan Demirci, by personally signing this document in lieu of an oath, hereby affirm that I prepared the submitted dissertation on the topic 'Analysis of nephrotoxic changes induced by calcineurin inhibitors in a rat model / Analyse nephrotoxischer Nebenwirkungen von Calcineurininhibitoren im Rattenmodell', independently and without the support of third parties, and that I used no other sources and aids than those stated.

All parts which are based on the publications or presentations of other authors, either in letter or in spirit, are specified as such in accordance with the citing guidelines. The sections on methodology (in particular regarding practical work, laboratory regulations, statistical processing) and results (in particular regarding figures, charts and tables) are exclusively my responsibility.

Furthermore, I declare that I have correctly marked all of the data, the analyses, and the conclusions generated from data obtained in collaboration with other persons, and that I have correctly marked my own contribution and the contributions of other persons (cf. declaration of contribution). I have correctly marked all texts or parts of texts that were generated in collaboration with other persons.

My contributions to any publications to this dissertation correspond to those stated in the below joint declaration made together with the supervisor. All publications created within the scope of the dissertation comply with the guidelines of the ICMJE (International Committee of Medical Journal Editors; www.icmje.org) on authorship. In

addition, I declare that I shall comply with the regulations of Charité –
Universitätsmedizin Berlin on ensuring good scientific practice.

I declare that I have not yet submitted this dissertation in identical or similar form to
another Faculty.

The significance of this statutory declaration and the consequences of a false statutory
declaration under criminal law (Sections 156, 161 of the German Criminal Code) are
known to me."

_____   _____

Date   Signature

Declaration of contribution

Hasan Demirci has contributed to this publication published at preprint server:

Demirci H., Popovic S., Dittmayer C., Yilmaz D. E., El-Shimy I. A., Mülleder, M., Hinze C. Persson B. P., Mutig K., Bachmann, S. (2023). Immunosuppression with Cyclosporine versus Tacrolimus shows distinctive nephrotoxicity profiles within renal compartments. bioRxiv, 2023-05. doi: https://doi.org/10.1101/2023.04.05.535688.

He is the sole first author. He conceived and designed research with the help of Prof. Dr. Sebastian Bachmann and Dr. Kerim Mutig. Hasan Demirci performed animal experiments, tissue processing; collected all blood and urine samples with the help of Suncica Popovic and Prof. Dr. Sebastian Bachmann. Hasan Demirci performed and analysed histological, physiological, and biochemical experiments; analyzed all data, and interpreted the results of the experiments. Hasan Demirci designed and analyzed multiomic data with the help of Dr. Ismail El-Shimy, Dr. Michael Mülleder and Dr. med. Dipl.-Math. Christian Hinze. Hasan Demirci further prepared all Figures and Tables. Prof. Dr. Sebastian Bachmann and Dr. Carsten Dittmayer performed SEM and TEM. Hasan Demirci and Prof. Dr. Sebastian Bachmann drafted the manuscript; Prof. Dr. Sebastian Bachmann, Hasan Demirci, Dr. med. Dipl.-Math. Christian Hinze, and Prof. Dr. Pontus B. Persson approved the final version of the manuscript.

_____

Signature, date and stamp of first supervising university professor / lecturer

Curriculum Vitae

My curriculum vitae does not appear in the electronic version of my paper for reasons of data protection.

Complete list of publications

Demirci H., Popovic S., Dittmayer C., Yilmaz D. E., El-Shimy I. A., Mülleder, M., Hinze C. Persson B. P., Mutig K., Bachmann, S. (2023). Immunosuppression with Cyclosporine versus Tacrolimus shows distinctive nephrotoxicity profiles within renal compartments. bioRxiv, 2023-04. doi: https://doi.org/10.1101/2023.04.05.535688 (preprint server).

Kriuchkova N., Breiderhoff T., Müller D., Yilmaz D. E., **Demirci H.**, Drewell H., Günzel D., Himmerkus N., Bleich M., Persson P. B., Mutig K. (2022) Furosemide rescues hypercalciuria in Familial Hypomagnesaemia with Hypercalciuria and Nephrocalcinosis model. Acta Physiologica, https://doi.org/10.1111/apha.13927 (IF: 7.523).

Oner L., Yilmaz D. E., **Demirci H.**, Ozbek T., Celik S. (2022) Detection of aflatoxins in tomato and pepper pastes in Istanbul, Turkey. European Journal of Science and Technology (35), 221-226, https://doi.org/10.31590/ejosat.1074060 (IF not avaliable).

Yilmaz D. E., Kirschner K., **Demirci H.**, Himmerkus N., Bachmann S., Mutig K. (2022) Immunosuppressive calcineurin inhibitor cyclosporine A induces pro-apoptotic endoplasmic reticulum stress in renal tubular cells. Journal of Biological Chemistry, Volume 298, Issue 3, 2022, 101589, ISSN 0021-9258, https://doi.org/10.1016/j.jbc.2022.101589 (IF: 5.486).

Demirci, H., Kurt-Gur, G., Ordu, E. Microbiota profiling and screening of the lipase active halotolerant yeasts of the olive brine. World J Microbiol Biotechnol 37, 23 (2021). https://doi.org/10.1007/s11274-020-02976-2 (IF: 3.24).

Demirci, H., Ordu, E. (2020). Metagenomic analysis of the microbial community in Çal Cave soil to elucidate biotechnological potential. Turkish Journal of Forestry, 21(3), 254-259. https://doi.org/10.18182/tjf.658468 (IF not avaliable).

Kurt-Gür, G., **Demirci, H.**, Sunulu, A., Ordu, E. Stress response of NAD+-dependent formate dehydrogenase in Gossypium hirsutum L. grown under copper toxicity.

Environmental Science and Pollution Research 25, 31679–31690 (2018). https://doi.org/10.1007/s11356-018-3145-1 (IF: 3.24).

Acknowledgments

Certificate of an accredited statistician

CHARITÉ

ChariteCentrum für Human- und Gesundheitswissenschaften

Charité | Campus Charité Mitte | 10117 Berlin

Institut für Biometrie und klinische Epidemiologie (IBIkE)

Direktor: Prof. Dr. Frank Konietschke

Postanschrift:
Charitéplatz 1 | 10117 Berlin
Besucheranschrift:
Reinhardtstr. 58 | 10117 Berlin

Tel. +49 (0)30 450 562171
frank.konietschke@charite.de
https://biometrie.charite.de/

Name, Vorname: Demirci, Hasan

Emailadresse: hasan.demirci@charite.de

Matrikelnummer: 227502

PromotionsbetreuerIn: Prof. Dr. Sebastian Bachmann

Promotionsinstitution / Klinik: Institut für Funktionelle Anatomie

Bescheinigung

Hiermit bescheinige ich, dass Herr Hasan Demirci innerhalb der Service Unit Biometrie des Instituts für Biometrie und klinische Epidemiologie (iBikE) bei mir eine statistische Beratung zu einem Promotionsvorhaben wahrgenommen hat. Folgende Beratungstermine wurden wahrgenommen:

- 30.11.2023

Folgende wesentliche Ratschläge hinsichtlich einer sinnvollen Auswertung und Interpretation der Daten wurden während der Beratung erteilt:

- t-Test und ANOVA: Adjustierung für multiples Testen
- Parametrische Testannahmen

Diese Bescheinigung garantiert nicht die richtige Umsetzung der in der Beratung gemachten Vorschläge, die korrekte Durchführung der empfohlenen statistischen Verfahren und die richtige Darstellung und Interpretation der Ergebnisse. Die Verantwortung hierfür obliegt allein dem Promovierenden. Das Institut für Biometrie und klinische Epidemiologie übernimmt hierfür keine Haftung.

Datum:

30.11.2023

Name des Beraters\ der Beraterin:

Camilo J. Hernandez-Toro

Camilo Jose Hernandez Toro

Digital unterschrieben von
Camilo Jose Hernandez Toro
Datum: 2023.11.30 09:42:24
+01'00'

CHARITÉ
UNIVERSITÄTSMEDIZIN BERLIN
Institut für Biometrie und
Klinische Epidemiologie
Campus Charité Mitte
Charitéplatz 1 | D-10117 Berlin
Sitz: Reinhardtstr. 58

Unterschrift BeraterIn, Institutsstempel